A. ALIKHANYAN NATIONAL SCIENCE LABORATORY

Armen Gyurjinyan

Studying atomic nuclei based on symmetry and clusters models

A THESIS

for acquiring the degree of candidate of physical-mathematical sciences in division 01.04.16 “nuclear, elementary particles and cosmic ray physics”

Scientific Supervisor: Prof. Robert Avagyan

Yerevan – 2016

Table of Contents

Acknowledgement

I would like to thank National Science Foundation for supporting this work under contract number NSF PHY-1419765 and everyone how helped me to do experiments and analyse the data especially Ani Aprahamian and Wanpeng Tan.

Abbreviations

ADC	Analogue to Digital Converter
ASIC	Application Specific Integration Circuit
CFD	Constant Fraction Discriminator
DAQ	Data Acquisition
DSA	Deuterated Scintillator Array
DSSD	Double-sided Silicon Strip Detector
FWHM	Full Width at Half Maximum
HIS	Helium Ion Source
HPGe	High-Purity Germanium
IBFM	Interacting Boson Fermion Model
IBM	Interacting Boson Model
ICC	Internal Conversion Coe_cient
ICEBall	Internal Conversion Electron Ball
MADC-32	Multiple Analogue Digital Converter
MQDC-32	Multiple charge integrated Analogue Digital Converter
PA	PreAmplifier
Si(Li)	Silicon-Lithium
MC-SNICS	Multi-Cathode Source of Negative Ions by Cesium Sputtering
SUSY	Super Symmetry
TDC	Time Digital Convertor

Notifications

$\hbar$=1.054*10^{-34} J*s reduced plank constant

π=3.14 mathematical constant

ln Natural base logarithm

H Hamiltonian

Ψ wave function

E energy

ε efficiency

J total angular momentum

I momentum of inertia

Chapter 1

1. Introduction

This chapter will present the motivation and explanation for both experiments. Below will be discussed different models and how they can be used, the advantages and disadvantages of each model.

1.1 Introduction

Since the beginning of ancient times, human kind always tried to explain the nature and the universe. In the end of 19th century, when the radioactivity was discovered by Becquerel new era in science began. That was the first step in the nuclear physics. Scientists begun to use models and symmetries to explain structure of nuclei and use reactions to explain the way the nuclei were produced. Huge amount of work was done so far, but there is still more to do.

Nuclear physics play big role in the explanation of the “Big Bang” theory and stellar evolution. Accelerator made possible to produce the reactions that are going on the stars and produce matter.

In my work I will show the results from two experiments which are necessary in understanding nuclear structure and models.

1.2 Shell Model

The only way to describe why for some number of nucleons the nucleus has higher stability than for other was to implement shell structure of nucleus. The model that describes the shell structure is the shell model. In the shell model the Pauli exclusive principle is taken into account. The observations showed that the Magic numbers are 2, 8, 20, 28, 50, 82 and 126. When the nucleus has the proton or neutron numbers equal to the Magic number than

the nucleus will have comparably higher binding energy than nearby nuclei. It is possible that both proton and neutron number will be equal to Magic numbers. That kind of nuclei called double-magic nuclei (^{4}He, ^{16}O, ^{40}Ca and etc.).

The shell model of the nuclei is very similar to the atomic shell structure. In the 1S(n=0, j=1/2) shell possible nucleon number is 2. The 1P(n=1, j=1/2,3/2) shell has two parts when j=1/2 then 2 nucleons, when the j=3/2 4 nucleons. There are total 6 nucleons in the 1P shell. 1st shell and 2nd shell numbers together will be 8 which is the magic number. With this way will be possible to get all magic numbers. Fig. 1.1 shows the structure of all shells and magic numbers in the shell.

Having the appropriate potential for the model is very important. It will allow to solve the Schrödinger equation and find the eigenvalues of energy. In the shell model a lot of simplifications lead to the central potential. So the potential depends only from radial distance and does not have angular dependence. The potential in the shell model is attractive and U(r)→0 as r→0. Schrödinger equation for such case is shown in the Eq. 1.1.

$$H\psi = \left[\frac{p^2}{2M} + U(r)\right]\psi_{nlm} \tag{1.1}$$

The equation is separable to the radial and angular parts therefore the solution can be written:

$$\psi_{nlm}(r) = \psi_{nlm}(r,\theta,\phi) = \frac{1}{r}R_{nl}(r)\psi_{nl}(\theta,\phi) \tag{1.2}$$

The radial part of the Eq. 1.1 can be written to Eq. 1.3

$$\frac{\hbar^2}{2M}\frac{dR_{nl(r)}}{dr^2} + \left[E_{nl} - U(r) - \frac{\hbar^2}{2M}\frac{l(l+1)}{r^2}\right]R_{nl}(r) = 0 \tag{1.3}$$

This model allows to explain magic numbers and the structure of the nuclei, but the model has some problems.

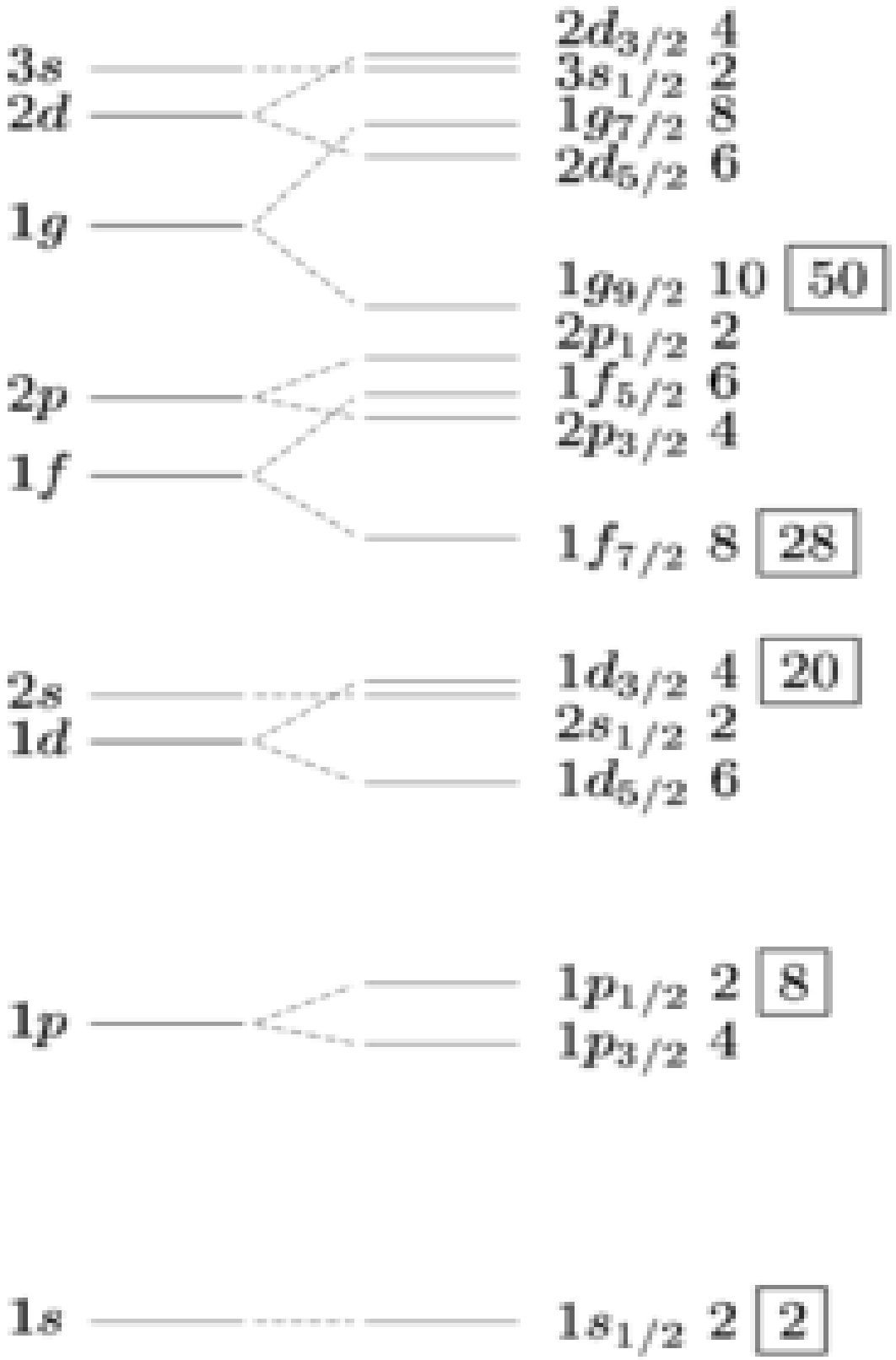

Figure 1.1 Nuclei shells and number of nucleon in each shell

Main issue is that there is no difference between proton and neutron. It does not take into account the charge of the proton which means absence of Coulomb force. That can lead that the stability should correspond the Z=N=A/2. However, the Coulomb interactions makes it difficult to add additional proton rather than a neutron. Due to there is a neutron excess when in the stable heavy nuclei.

1.3 Internal Conversion Electrons

The de-excitation of the nuclei can happen with multiple ways. One of the way is that the nuclei will emit γ-ray or multiple and reach ground states. Other way is that the nuclei will pass the energy to the electron in the K, L … shell and they will come out from the atom. Those electrons called the conversion electrons. Fig. 1.2 shows the diagram for emitting the conversion electrons.

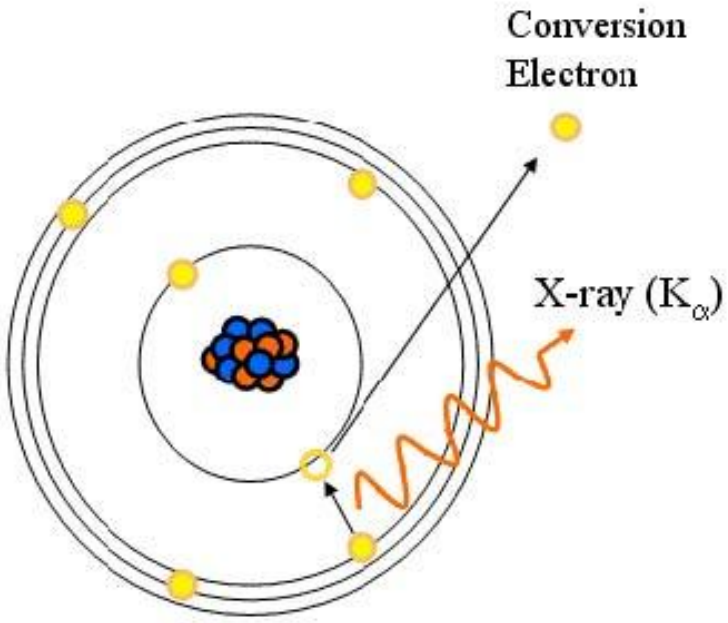

Figure 1.2 The diagram of emitting internal conversion electron.

After emitting the electron another electron from higher energy level will take that place and emit X-ray.

Same excited level can emit both electron and γ-ray, if it is not an E0 transition. Measuring the Yields of the electron and γ-rays will be possible to measure Internal Conversion Coefficient (ICC) and do some predictions for spin and multi polarity of the excited level.

1.4 “Nuclear” Super Symmetry (SUSY) in the medium-heavy nuclei range (A–190)

Studying the nucleus in the physics means have a model that will describe structure, deformation, excitation energy levels and etc. of the nucleus.

The shell model can describe nuclei with low mass up to 50 nucleons. Then more nucleon in the nuclei, more shells should be taken into account and the number of nucleons configuration becomes so big that shell model will be intractable.

The idea that the symmetries are key part of the nature lead to the developing of the new dynamical models [1]. The model that was developed initially was Interacting Boson Model (IBM) [2]. The model describes the even-even nuclei and allows to do predictions for excitation energies. Later model was developed to include even-odd or odd-even nuclei, and excitation energies was possible to predict. The model was the Interacting Boson-Fermion Model (IBFM) [2, 3]. Finally, during 80's the final model was developed that describes the odd-odd nuclei excited levels as well [4, 5, 6]. The model is “Nuclear” Super Symmetry (SUSY).

The “Nuclear” SUSY should not be confused with the SUSY that is describing the unified fundamental forces and studying with Large Hadron Collider. The nuclear SUSY is not a fundamental as the particle SUSY, it is a composite symmetry of bosons and fermions in an approach that can be used to predict the structure of odd-odd nuclei. Model that can predict the odd-odd nuclei structure remains the problem even today.

IBM is the framework with the dynamical symmetries via Lie Algebras to describing collective properties of even-even nuclei of various geometrical shapes and the transition regions between them in a unified network.

The IBM and its inherent symmetries proved valuable benchmarks in nuclear structure by providing equation to calculate energy levels, selection rules for de-exciting transitions, and transfer strengths that could be directly compared with experimental findings near the symmetries and in the transitions between them by a unified Hamiltonian that could reflect the observed evolution of structure.

The model describes the nuclei as an inert core combined with bosons which represents pair of identical nucleons. In this model neutron and proton behave as same particle. The even-even member of this super group is known to exhibit the O(6) symmetry [7].

This IBM concept was later expanded to include odd-even and even-odd nuclei via symmetries of the Interacting Boson Fermion Model (IBFM). In this model neutron and proton behave as a different particles due to was possible to extend the model.

IBFM describes nucleus as a core, which is inert even-even nucleus, and fermion which interacts with the core.

There is possibility of two kind of interaction between the fermion and even-even nucleus. The subsections will describe Lia algebra and then each of possible interactions.

1.4.1 Lie Algebra

The Lie Algebra is the mathematical method of describing the abstract group. Lets assume a group *G* with the group members ($\hat{G}_1, \hat{G}_2, \ldots, \hat{G}_n$). The group should satisfy following conditions:

1. Closure:

If the $\hat{G}_i$ and $\hat{G}_j$ are the members of the group then their product $\hat{G}_i\hat{G}_j$ is also a member.

2. Associativity:

The $\hat{G}_i(\hat{G}_j\hat{G}_k) = (\hat{G}_i\hat{G}_j)\hat{G}_k$ property is always valid.

3. Identity:

There exist an $\hat{E}$ element of *G* group that $\hat{E}\hat{G}_i = \hat{G}_i\hat{E} = \hat{G}_i$.

4. Inverse:

For every $\hat{G}_i$ there is an element $\hat{G}_i^{-1}$ such that $\hat{G}_i\hat{G}_i^{-1} = \hat{G}_i^{-1}\hat{G}_i = \hat{E}$.

The elements of the group can be obtain by the set of the elements $\hat{g}_i$, i=1,2,...,s called generators. Simplest example of the group that satisfy Lie algebra is SO(2) group of rotations. The group members can be written as:

$$\hat{G}(\alpha) = e^{-i\alpha\hat{l}_z} \tag{1.4}$$

Where α is rotation angle and

$$\hat{l}_z = -i(x\frac{\partial}{\partial y} - y\frac{\partial}{\partial x}) \tag{1.5}$$

is the generator of transformation in the x-y plane. Transformations in the z-x and y-z planes will be

$$\hat{l}_y = -i(z\frac{\partial}{\partial x} - x\frac{\partial}{\partial z}),\ \hat{l}_x = -i(y\frac{\partial}{\partial z} - z\frac{\partial}{\partial y}) \tag{1.6}$$

Finite rotation in the three-dimensions can be parametrized by three Euler angles.

Now let's apply this to physical systems. Invariance of the Hamiltonian under the algebra leads to the

$$[\hat{H}\hat{g_i}] = 0 \tag{1.7}$$

and g plays the role of symmetry algebra for the system.

If there is a chain of algebra will lead to introducing the dynamical symmetries. That will lead to the following Hamiltonian:

$$\hat{H}' = \alpha C_{l_1}(g_1) + \beta C_{l_2}(g_2) \tag{1.8}$$

where $C_{l_i}(g_i)$ is the Casimir invariant of g_i .

1.4.2 U(6/4) Super Symmetry

First case is the $SO^B(6)$ boson group and $SU^F(4)$ fermion group. The subgroup is called U(6/4) dynamical supersymmetery. This group describes the fermion-core interaction, when fermion can occupy only single level.

The Hamiltonian for this case can be written as

$$H = AC_{2SO^B(6)} + BC_{2Spin(5)} + DC_{2Spin(3)} \tag{1.9}$$

which leads to an analytic form for the energy as a function of the quantum numbers

$$E = A\Sigma(\Sigma+4) + \mathrm{B}[\sigma_1(\sigma_1+4) + \sigma_2(\sigma_2+2) + \sigma_3^2] +$$

$$+C[\tau_1(\tau_1+3) + \tau_2(\tau_2+1)] + DJ(J+1) \tag{1.10}$$

The coefficients A, B, C and D are determined in a simultaneous fir of the excitation energies of even-even and odd-even nuclei that belongs to the same supermultiplet. Both equations deviations can be found in the Ref. [8].

1.4.3 U(6/12) Super Symmetry

Second case is the $SO^B(6)$ boson group and $SU^F(12)$ fermion group. The subgroup is called U(6/12) dynamical supersymmetry. This group describes the fermion-core interaction, when fermion can occupy multiple level.

The Hamiltonian for this case can be written as

$$H = \alpha C_{2U^B{}_{F(6)}} + \beta C_{2SO^{BF}{}_{(6)}} + \gamma C_{2SO^{BF}{}_{(5)}} + \delta C_{2SO^{BF}{}_{(3)}} + \epsilon C_{2Spin(3)} \quad (1.11)$$

which leads to an analytic form for the energy as a function of the quantum numbers

$$E = \alpha[N_1(N_1+5) + N_2(N_2+3)] + \beta[\sigma_1(\sigma_1+4) + \sigma_2(\sigma_2+2) + \sigma_3^2] +$$

$$+\gamma[\tau_1(\tau_1+3) + \tau_2(\tau_2+1)] + \delta L(L+1) + \epsilon J(J+1) \quad (1.12)$$

Again the equations where taken from the Ref. [8].

1.4.4 Super Symmetry (SUSY)

Final stage of the extension of the model is “Nuclear” Super Symmetry (SUSY). In the “Nuclear” SUSY the bosonic and fermionic degrees of freedom are combined in one common set of multiplets that could predict the structure of the odd-odd nucleus [4, 5, 6].

This theoretical formalism leads to a quartet of nuclei with equal numbers of bosons and fermions that could be linked by SUSY. The supersymmetry that describes the super group is U(6/12)⊗(6/4).

As super group members was used ^{194,195}Pt and ^{195,196}Au. The number of bosons and fermions are related to the number of valence nucleons the number of protons and neutrons outside the close shells. For example, ^{194}Pt has 78 protons and 116 neutrons. The quantum numbers can be calculated $N_\pi = (82-78)/2 = 2$ and $N_\nu = (126-116)/2 = 5$. On the other hand, ^{195}Au has 79 protons and 116 neutrons, so it has 3 valence protons and 10 valence neutrons. It means that $N_\pi = 1$, $M_\pi = 1$ and $N_\nu = 5$, M_ν=0. Table 1.1 shows the quantum numbers for all members.

Table 1.1. Number of proton and neutron bosons ($\boldsymbol{N_{\pi,\nu}}$) and fermions ($\boldsymbol{M_{\pi,\nu}}$) for ^{194,195}Pt and ^{195,196}Au members of the quartet.

Nucleus	N_π	M_π	N_ν	M_ν
$^{194}_{78}Pt^{116}$	2	0	5	0
$^{195}_{78}Pt^{116}$	2	0	4	1
$^{195}_{79}Au^{116}$	1	1	5	0
$^{196}_{79}Au^{116}$	1	1	4	1

The invariant for the SUSY is “N+M”, compare to IBM in which “N” is invariant. The odd neutron of this group can occupy $3p_{\frac{1}{2}}$, $3p_{\frac{3}{2}}$ and $3f_{\frac{5}{2}}$, orbits

and the odd proton can occupy only $2d_{\frac{3}{2}}$ orbit. So for this super group the U(6/12)⊗(6/4) SUSY should be used.

The Hamiltonian for the U(6/12)⊗U(6/4) is shown in the Eq. 1.13 from Ref. [8].

$$H = AC_{2U^{B}F_{V}(6)} + BC_{2SO_{V}^{BF}(6)} + B'C_{2Spin(6)} + CC_{2Spin(5)} +$$

$$+DC_{2Spin(2)} + EC_{2SU(2)} \quad (1.13)$$

Solution of the eigenvalues problems is shown in the Eq. 1.14. A, B, B′, C, D, E are the fitting parameters. With the following equation will be possible to predict the ^{196}Au energy levels.

$$E = A[N_1(N_1+5) + N_2(N_2+3)] + \mathrm{B}[\Sigma_1(\Sigma_1+4) + \Sigma_2(\Sigma_2+2)] +$$

$$+ B'[\sigma_1(\sigma_1+4) + \sigma_2(\sigma_2+2) + \sigma_3^2] + C[\tau_1(\tau_1+3) + \tau_2(\tau_2+1)] +$$

$$+DL(L+1) + EJ(J+1) \quad (1.14)$$

The predictions for the level structure of ^{196}Au involve only six parameters and can be compared with experiment. Extensive experimental efforts have been made before [9, 10, 11] to study the structure of ^{196}Au utilizing transfer reactions with protons as well as deuterons, by in-beam γ-ray and internal conversion spectroscopy to provide robust evidence for the existence of "Nuclear" SUSY. With excellent agreement between prediction and experiment up to approximately 250 keV and fairly good agreement up to 500 keV in excitation energy. Gröger et al. [9] were careful to point to the dependence of the predictions for ^{196}Au on the detailed spectroscopy of the odd-even and even-odd members of the multiplet.

1.5 Clusters in the α-conjugate nuclei

After the Big Bang only light nuclei (H, He and Li) were created. These nuclei become a building block for synthesis of higher mass elements. The α-nucleus as a cluster component has been identified in α-conjugate nuclei that are nuclei with equal and even number of proton and neutrons. The special stability of the α-nucleus or clusters of α-particles continue to persist in heavier nuclei such as ^{12}C, ^{16}O, ^{20}Ne, ^{24}Mg and others [21]. Besides that ^{4}He is noble gas and interacts very weakly, first excited state of this nucleus is around 20 MeV. The binding energy of this nucleus is also very high compare to nearby nuclei. Addition to this α-α strong and repulsive interaction coming from Pauli Exclusion Principle [22, 23], made α-cluster model [24].

1.5.1 α-particle Model

The liquid-droplet model of the nucleus that was discovered by Bohr, gives good description of many nuclear processes and information on nuclear binding energy. But better understanding of the excited levels of the nuclei only with other models based on more specific assumptions. The difference between the liquid-droplet model and the α-particle model [24] is that the first model discuss neutrons and the protons as independent particles, however, the second model first discuss two protons and two neutrons interactions (α-particle) and then such subgroups interactions between each other.

The interaction-potential for α-particles is shown in the Fig. 1.3 from Ref. [24]. The r_0 is the radius of the nuclei. There is attractive force only when the α-particles in the nuclei are within some range near the radius. After some radius there is a repulsive force so α-particle will be ejected. With this model is possible to describe α-decay in heavy nuclei.

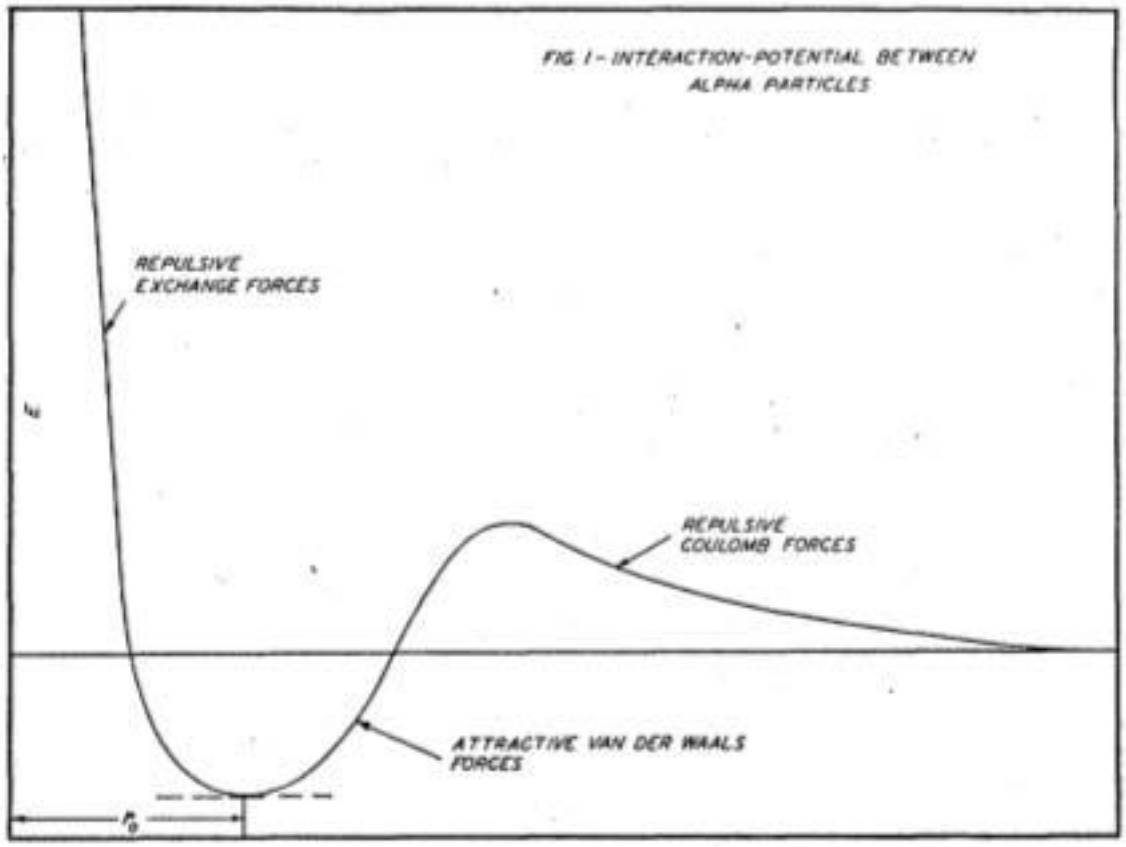

Figure 1.3 The interaction potential between the α–particles Ref. [24].

During 1960s multiply studies were done to revival the model [25, 26] and eventually in 1968 Ikeda suggested the structure of α-clusters in the α–conjugate nuclei excited states [27].

Ikeda showed that since some threshold in the α-conjugate nuclei begin to form the α-particles. Eventually at some point nuclei will be completely clustered. That energy is called α break-up energy. For example, ^{16}O breakup energy is the 14.44 MeV. So any excited level above the 14.44 MeV will break-up into 4 α-particles.

Another important quality of this model is ability to measure the momentum of inertia of the nucleus in the excited level. That can be done with the Eq. 1.15, where "E_x" is the excitation energy of the nucleus coming from the rotation, "I" is the momentum of inertia and the "J" is the spin of the state.

$$E_x^* = \frac{\hbar^2}{2I} J(J+1) \quad (1.15)$$

As the α-particles is Bose particle and the ψ wave functions are asymmetric than only the J = 0, 2, 4 … spins will be allowed.

1.5.2 ^{16}O cluster

The one of the important parameters in the α-conjugate is the α-bonds in the nuclei. The α-bonds shows how many α-α interactions are in the nuclei. For example, ^{8}Be has only one α-α bond, ^{12}C has 3 α-α bonds and etc. The binding energy of the nuclei depends from number of the bonds linearly (Ref. [28]) as shown in the Fig. 1.4.

One of the best example that forms α-cluster is ^{16}O. Numerous experiments with different methods were done [21, 29, 30, 31] to study α-cluster components in the structure of ^{16}O. The structure of the ^{16}O is very interesting as the number of protons and neutrons is magic number and the shell is closed.

The other aspect of the ^{16}O structure is relevant for α-burning reactions thought to play a significant role in stellar evolution. ^{12}C/^{16}O rate is very important for stars age measurements.

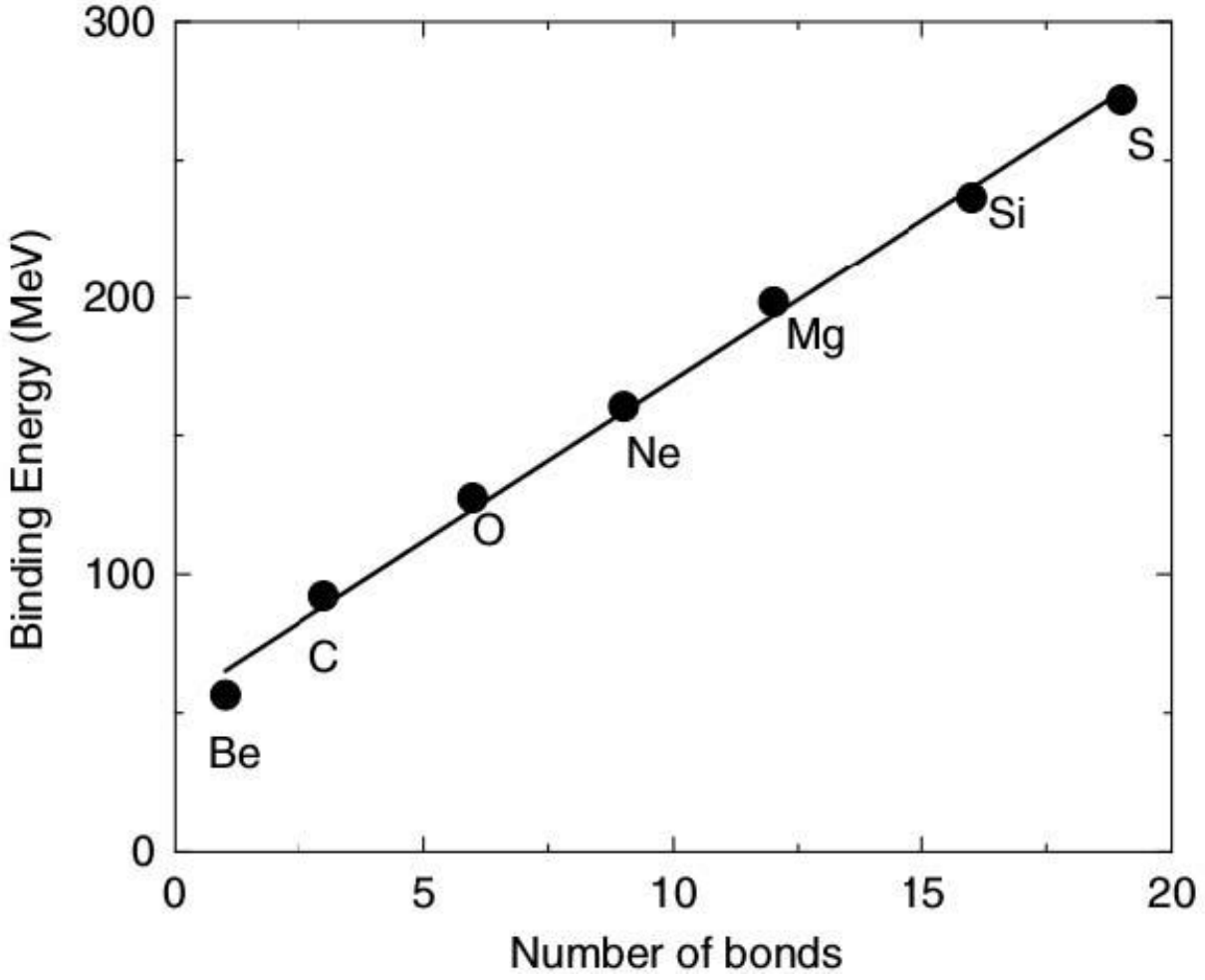

Figure 1.4 The binding energy versus to number of bond in the binding energy versus to number of bond in the α-conjugate nuclei from Ref. [28].

The experiment that was done and results are shown in the dissertation is related to only ^{16}O structure. The Chevallier et al Ref. [29] measured the momentum of inertia of the ^{16}O excited levels above the 4α break-up level and showed that there is a possible linear α-chain in some excited levels of ^{16}O.

The measurements in the Ref. [29] shows that the bands have four time larger momentum of inertia compared to relatively low-lying energy levels. That is very big number for momentum of inertia. That kind of momentum of inertia can be reached only if all α-particles will lie together on the same line making the linear chain.

Chapter 2

2. Facility and Used Packages

Both experiments were carried out at the University of Notre Dame, IN, USA. This chapter will presents the facilities that was used for experiments and the main packages that were used for simulation and data analyzing. The layout of the facility is shown in the Fig. 2.1. The FN Tandem is accelerator, Helium Ion Source (HIS) and Multi-Cathode Source of Negative Ions by Cesium Sputtering (MC-SNICS) are the ion sources. The detail explanation of all that will be presented below. All the information about the facility can be found in the Ref. [34, 35, 36, 37].

The packages that were used are Geant4 and ROOT. Those are OOP packages mainly developed for high energy physics, but later modified to be used for nuclear physics simulation (Geant4) and any kind of data analyzing (ROOT).

2.1 FN Tandem

The facility that was used for experiments is mostly concentrated on low energy nuclear physics. In the following section I will present the facility that was used to do experiments. The charging and acceleration systems will be discussed more detailed.

The main part of the FN Tandem is the terminal. It is the part where all positive charge is concentrated. So for example the Tandem that was used is 11 MV so in principle it should be possible to put so much charge into the terminal to create 11 MV potential.

The terminal will be charged with two “Pelletron chains” low and high energy part. That is why this type of accelerators called “Pelletron accelerators”.

Figure 2.1 The layout of the Nuclear Science Laboratory at the University of Notre Dame.

The pellets are metal and connected together with nylon inter-connectors. All pellets are isolated from each other. The chains rotate all the time and keep the terminal positive voltage constant.

After putting voltage to the terminal with the chains it is necessary to use the field for acceleration. As it is electrical field than the Coulomb force is relative to $1/r^2$. So the Fig. 2.2 first figure is presenting the electrical field dependence from distance. This way of the acceleration is very bad as the ion will et most of its energy when it will be close to the terminal.

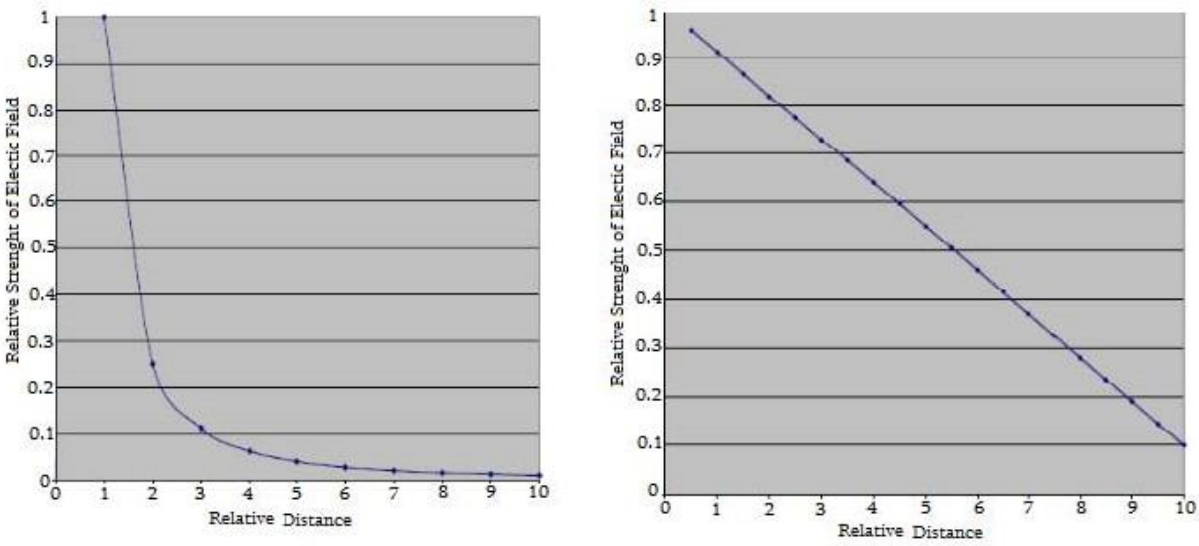

Figure 2.2 Electric field dependence from distance with and without resistances.

That is why method was used to make acceleration better. All the LE and HE tubes the metallic plates are put and connected each other with 300 MOhm resisters. All that are connected to the terminal and the charge of the terminal is spreader between the plates. The Fig. 2.2 second figure shows the electric field strength dependence from distance for this case. Now the ion will accelerated linearly. Fig. 2.3 shows the detailed structure of the FN Tandem.

Next step is to accelerate ions. Ions entered to the FN Tandem with the -1 negative charge so the electrical field will attract them and accelerate. Than in the terminal when there is no electrical field with the stripper foil the ion's charge will be changed to positive and with the repulsive forces the ion again will be accelerated.

There is possible that ion has multiple electrons whichever charge is preferable can be chosen later with magnetic fields. Different charges mean different energies. So same beam energy can be increased or decreased if the magnetic field's configuration will be changed.

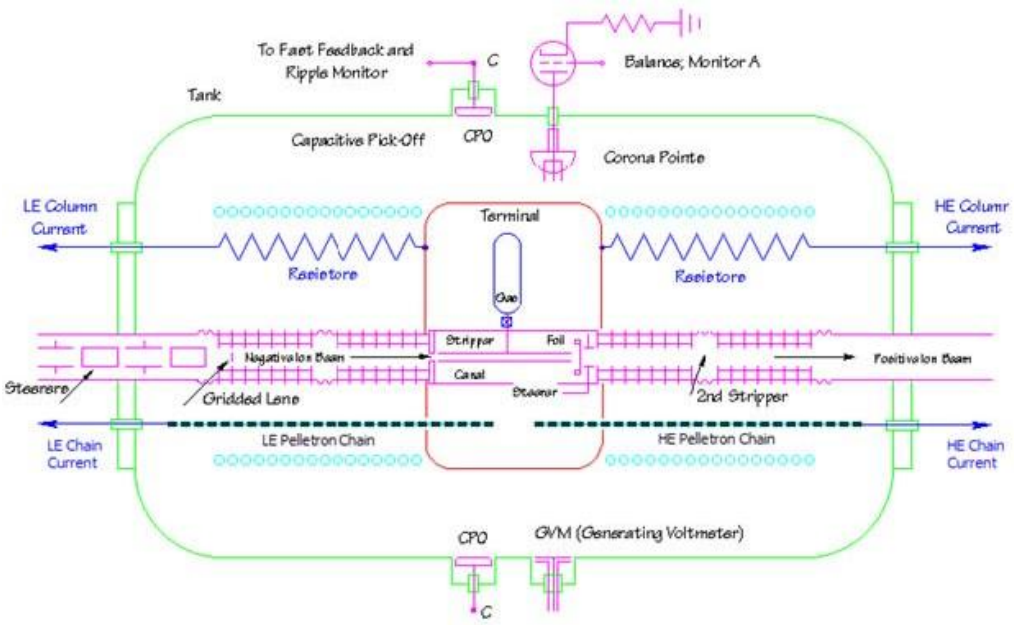

Figure 2.3 Charging system diagram of the FN Tandem accelerator.

The way to calculate the beam energy is very simple: If the ion has the -1 negative parity at low energy column and Q positive parity at the high energy column than total beam energy will be (1+Q)V where V is the voltage on terminal.

For example if the ion is the ^{12}C and the terminal voltage is 3 V than after passing high energy column as the ^{12}C has 6 electrons than 6 different ^{12}C will exist. If the charge is +1 then the energy will be 6 MeV, and for +6 the energy will be 21 MeV. But usually it is very difficult to strip all the electrons from the ion so the ^{12}C beam usually has either +2 or +3 charges. The way to increase the amount of the +6 charged ions was putted second stripper foil in the middle of the high energy column. So after the stripper more ions will have +6 charge and the beam intensity with high energy will increase.

2.2 Ion Sources

Except from the FN Tandem the other important facilities are the ion sources. The detailed explanation of how each ion source is working will be presented in the subsections below.

2.2.1 Multi-Cathode Source of Negative Ions by Cesium Sputtering (MC-SNICS)

The Multi-Cathode Source of Negative Ions by Cesium Sputtering (MCSNICS) is the sputter ion source. This ion source can produce all kind of stable ion beams except the Helium. It has advantage that is possible to load the wheels of cathodes 20 or 40 at any time and do different beam runs if it is necessary.

The production of ion is very simple. It has the reservoir of cesium which is heated and creating the cesium vapour. The cesium vapour rise into close space under high vacuum between the cathodes which is cooled and heated ionizer.

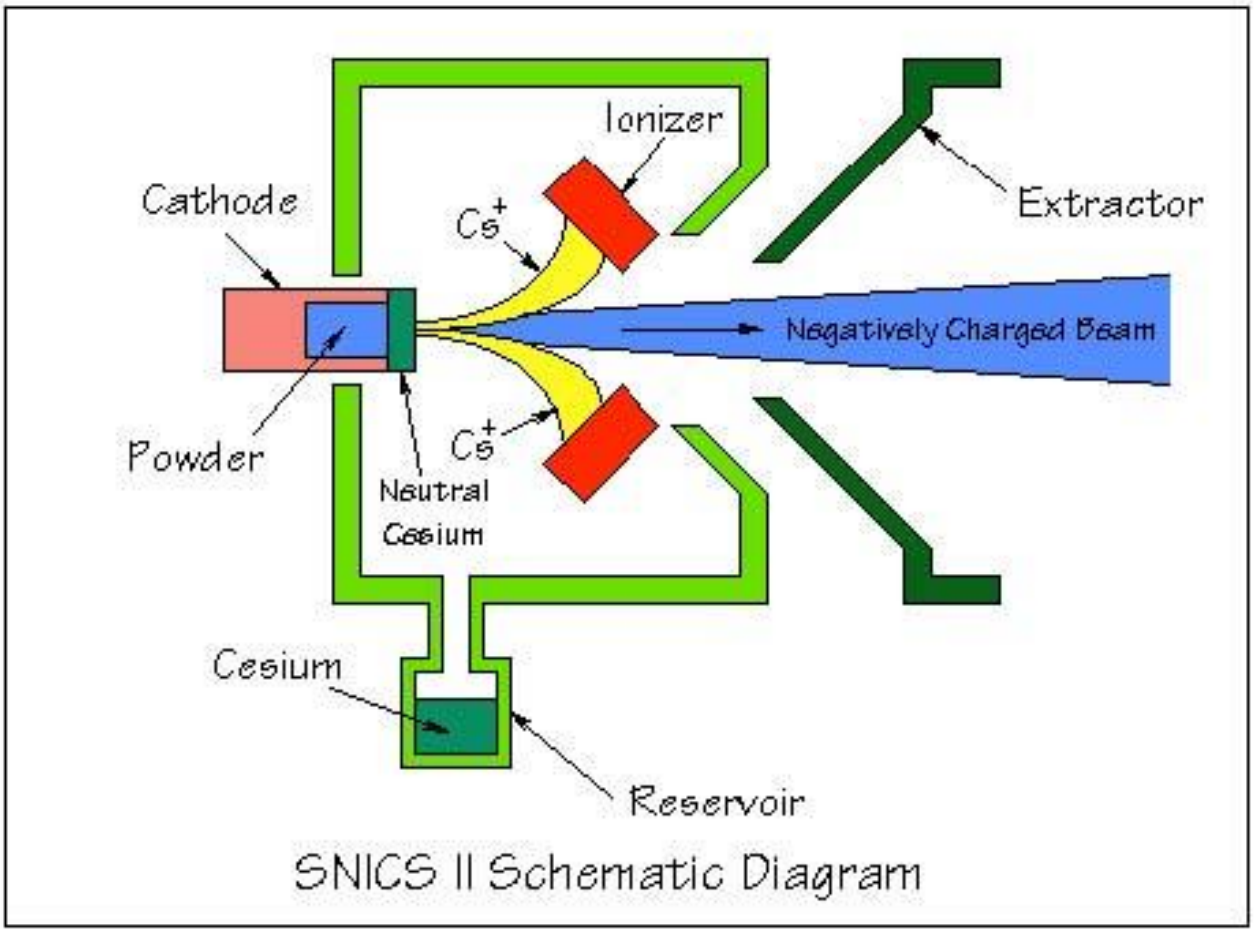

Figure 2.4 Charging system diagram of the FN Tandem accelerator.

Hitting the surface of ionizer the cesium gain positive charge and accelerates towards the cathode. In the cathode it interacts with the material and part of the atoms capture electron and become negative. Negative ions get out and produce beam. The Fig. 2.4 shows the diagram how everything is happening. After having the negative beam it will be accelerated through the tandem and change charge to positive.

2.2.2 Helium Ion Source (HIS)

The ^{3}He and ^{3}He cannot be ionized with the MC-SNICS. As the Helium is a noble gas it interacts with matter very rare. So simple way of adding a electron to the Helium atom will not work, but there is complicated way to do it.

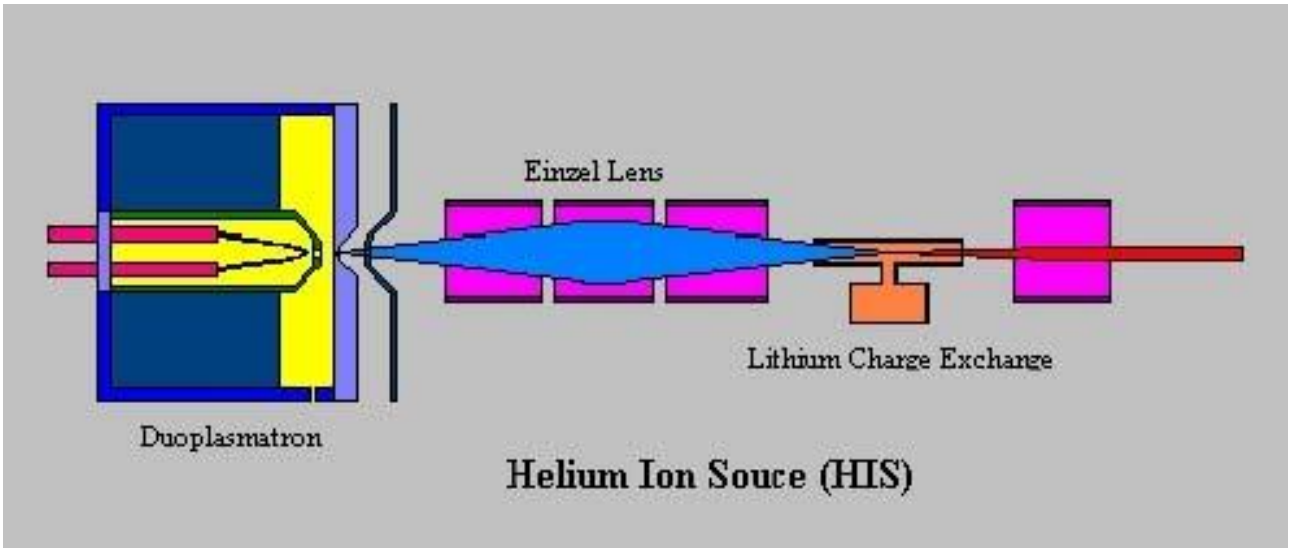

Figure 2.5 Charging system diagram of the FN Tandem accelerator.

The electron can be added to the Helium atom with duoplasmatron. It has the small tungsten wire in it called filament, which is heated by passing current through it. The filament will create electrons in the region and the gas will be ionized with that electrons.

The positive charged ions will pass through the small hole called “button”. The beam will focused and send to the region filled with lithium vapour. Ions interaction with the vapor will make ions to pick-up one or multiple electrons.

That way a negative charged Helium ions will be created. Afterwards, all that negative ions will be injected into the accelerator.

2.3 Internal Conversion Electron Ball (ICEBall)

Internal Conversion Electron Ball (ICEBall) is constructed mainly for electron detection. It has six Silicon-Lithium (Si(Li)) detectors. The detectors have 5 mm thickness and around 750 mm^2 surface. The allowed energy window for the electron detection is approximately from 50 keV to 2 MeV. The energy window is due to the mini-orange filter in front of the detector.

The mini-orange filter is magnetic field which allows to pick certain energy range in place of the total range. The Fig. 2.6 shows the structure of one mini-orange filter and single Si(Li) detector. The magnetic field is between the wings of the filter and it has certain distance from the detector. If the magnetic field will be picked certain way only electrons with the energy of interest will reach to the detector. As it shown in the Fig. 2.6 electrons for the fixed energy electrons will pass and reach to detector. Electrons that have low energy will hit the mini-orange filter which is Tungsten and the electrons will be completely stopped there. Electrons that have higher energy will be bended too much and will miss the detector.

In the current experiment the mini-orange filter was setup to allow detection the electrons with the energy range from 50 keV to 750 keV, as low-lying energy levels of the 195Au are important to study.

The binding energy of the electrons in the K-shell is around 80 keV and in the M and L shells is around 15 keV. So the γ-rays energies range will be from 65 keV to 830keV. Any γ-ray transition that will have other energy can be measured in the γ-ray detectors but cannot be used to calculate internal conversion coefficient.

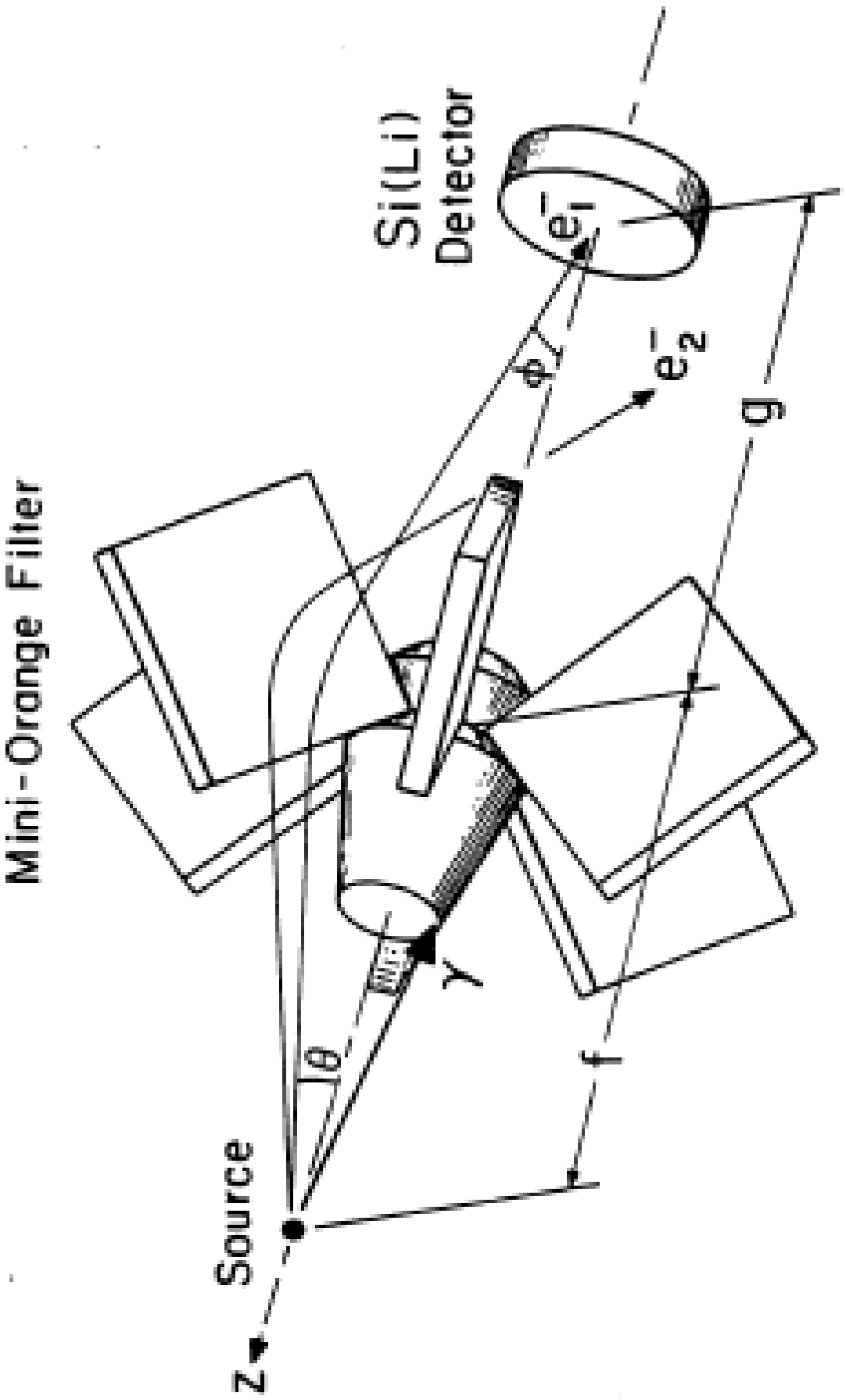

Figure 2.6 The mini-orange filter plus Si(Li) detector.

2.4 High-Purity Germanium Detector

High-Purity Germanium (HPGe) detectors are the best detectors for the γ-rays detection. They have very good resolutions and γ-rays can be separated from each other very well, but they have also disadvantage. Under neutron flux the crystal of the detector damages very fast as it is under high voltage. The neutron flux limits the beam intensity.

High voltage power supplies are required for this detectors as the voltage is around 3 kV – 5 kV. In the experiment that is presented in the current dissertation two this kind of detectors were used. The energy range of the detectors was until 2 MeV.

2.5 Packages

Except the technical problems to do the experiment, another problem is data analyzing. Multiple codes and packages were developed for that. I used the ROOT package to do all my data analyzing and Geant4 package for nuclear reactions simulations. Both packages were developed in CERN for high energy physics as they need to have good idea where to put the detectors and after reading out the huge amount of data make it fairly easy to analyze that. Both codes are Object Oriented and based on C++ coding style.

2.5.1 ROOT

ROOT is very powerful package for data analyzing. It allows to make trees with branches and fill them. So it is possible to have a lot of detectors, read out the data from all of them and fill into the tree. Later will be possible to do gates on one branch and look to the other detector results.

The electronics that was used does not write exactly everything into the root fills. There should be converter to do that. There is evt2root package written by Karl Smith which can be used to convert all data into the root files.

I did some modification in that package to be able to use it for this experiments data conversion.

The root has also another important advantage compare to other packages for data analysing. It has interface with multiple functions and ability to do design of the spectrum.

In the data analysis the scripts where written which will go over all entries and do the important measurements and fill or draw histograms. Additional the main root scripts other header files were written and used to make the process of running the code much faster and easier to read.

The advantage of the ROOT is also that it does not need a lot of space in the hard drive. Few Gigabytes of information can be stored in the few Megabytes ROOT file. This helps save the space in the hard drive as well.

During the experiment DAQ can be stopped for different reasons and new files will be created every time new run will be started. ROOT allows to chain all the files together and use all at once.

2.5.2 GEANT4

Geant4 is a simulation package developed in the CERN as well. The main purpose of the package was to help high energy physicist to choose best location for their detectors as the detectors are very big and difficult or even not possible to move. Later the code modified, models were developed to use for low and intermediate nuclear physics as well.

The Geant4 consist of 3 mandatory classes: “DetectorConstruction”, “PhysicsList” and “PrimaryGeneratorAction”. Then there are other action classes that can be used like “RunAction”, “SteppingAcion” and so on.

“DetectorConstruction” is the class that describes the experimental hall, detectors, target chamber and other thing that describe the experimental setup. In the “DetectorConstruction” basic used classes are for shape of the volume, material of the volume and the physical position of it. There can be daughter and mother volumes. It is possible to rotate the volumes and position as the author will prefer. If mother volume rotates all daughter volumes rotate automatically with it.

The next class is “PhysicsList” is the class that contains all physical process that should be taken into account. There are a lot of the already existing physics list which include both hadronic and electromagnetic interactions, but the author can easily write the “PhysicsList”. For example someone wants to study only pair production or Compton scattering than he can only use the header files for that physics.

Finally the “PrimaryGeneratorAction” controls the initial particle number, energy, direction and etc. In this class only some particles can be chosen like proton, electron, γ-ray, neutron α-particle and so on. Ion cannot be generated as initial particle since the Geant4.10 version. But still there is way to generate ions. Initial particle can be defined any particle in the “PrimaryGeneratorAction” (there is a special particle called geantino that can be used as well) and then after running the code in the command line can be typed the following commands:

\gun\ particle ion

\gun\ ion Z A E_x

where Z is the number of protons, A is the mass number and E_x is excitation energy of the ion. For example ^{8}Be ion in the ground state can be generated with the following commands:

```
\gun\particle ion
\gun\ion 4 8 0
```

Chapter 3

3. ^{195,196}Pt(p,xn) ^{195}Au Experimental Data

The ^{195,196}Pt(p,xn)^{195}Au experiment was carried out at the University of Notre Dame Nuclear Science Laboratory with the 11 MV Tandem. The Internal Conversion Electron Ball (ICEBall) array of 6 Silicon-Lithium (Si(Li)) detectors with an energy resolution of 3-5 keV and 2 High-Purity Germanium (HPGe) detectors with 109% relative efficiency [39] was used during experiment. Relative efficiency is in comparison to NaI detector with 3 inch diameter and 3 inch width.

The ^{195}Pt and ^{196}Pt targets with thicknesses of 1.07 mg/cm^2 and 1.34 mg/cm^2, respectively were used. A beam of bunched protons was used with 7.75 MeV on ^{195}Pt and 12 MeV on ^{196}Pt to populate levels in ^{195}Au and ^{196}Au.

Hardware coincidences were used for the ^{195,196}Pt(p,xn) reactions studies. DAQ was set up to read out only when any two detectors triggered simultaneously. This reduced the background, making lower intensity peaks more pronounced.

Following chapter shows the experimental methods, results and discussions for the experiment.

3.1 Experimental Methods

In this experiment γ-ray and electron spectroscopies were done. It is important to have good ADC to get precise result for γ-s and electrons energies. In the following section will be discussed the test and comparison of two different ADCs, as well as, used software important information. First ADC is the NIM standard ORTEC ASPec-927 [40] ADC, which is one of the best

ADC for γ-ray spectroscopy. This ADC has a maximum resolution of 16K bit and yields an energy resolution 1.6 keV at 1 MeV, but this ADC is very expensive. Second one was Mesytec MADC-32 [41] with 32 input channels. Compare to the ORTEC ADC, Mesytec is much cheaper and faster. So it is important to show that the resolution and integral linearity is similar for both modules to use MADC-32.

The HPGe detector that was used during experiment was used to detect γ-s from ^{152}Eu calibration source during the test. Signals from HPGe detector were divided into two parts one for MADC-32 module and other for ORTEC module. RadWare [42] software was used to analyze both spectra and look at the resolutions of the ADCs as a function of energy, as well as, the linearity.

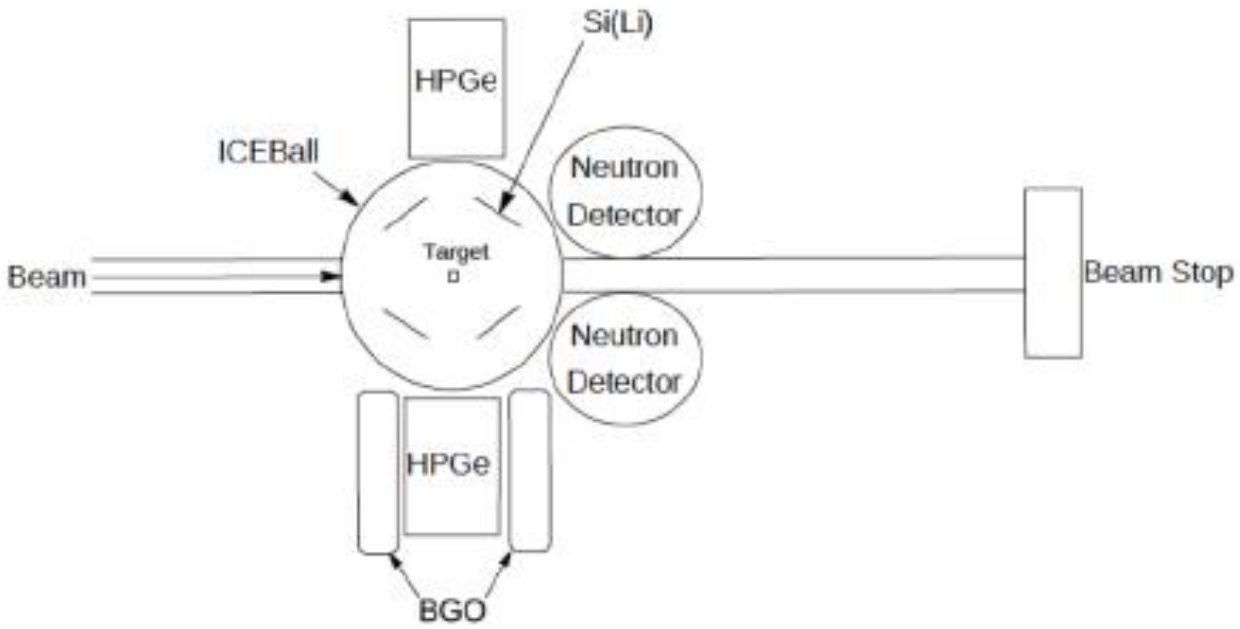

Figure 3.1 The experimental setup of this experiment using the ICEBALL array of Si(Li) detectors, 2 HPGe detectors, and 2 neutron scintillators. ICEBall is shown from a top down perspective showing 4 of the 6 Si(Li) detectors, the other two detectors are at the top and bottom centered over the target.

Two neutron scintillators were used to do only to put gates and make sure that the neutron was produced during the reaction. The gates on neutron detector improved the peak/background ratio a lot. BGOs are γ-ray detectors working as a veto on the HPGe detector. It helps to reduce Compton scattered γ-rays from the spectra, but unfortunately only one of the detectors had BGO shielding.

Figure 3.2 The carbon target ladder shown with a target frame, and collimator. The collimator is made out of tantalum and was used for beam tuning. All calibration sources were mounted on the same ladder to insure centering in the ICEBAll array.

The detailed information of the experimental setup were accepted to publish in the European journal of Physics (Ref. [33]).

Targets were mounted on the special target ladder which was mad carbon. Usually target ladders are from the aluminum, but it increase background and the excited levels of the aluminum are very low. On the other hand carbon excited levels is around 4 MeV which is too high and there will not be background from the target ladder. There are few positions in the target ladder as shown in the Fig. 3.2. One of them was used as target position another one as a small collimator to tune beam exactly to the center of the target.

3.1.1 RadWare

Radware is least-squares peak-fitting program designed to do γ-ray spectroscopy, but it can be used for electron spectroscopy as well. In the current program peak will be divided into three components. First one is Gaussian function, second is skewed Gaussian and third one is step function. Fig. 3.3 shows how each component make up main peak. There are two parameters “R” and “Step”. “R” describes part of the peak coming from skewed Gaussian and “Step” describes low-energy side background increase. There is also another important parameter that describes skewness of skewed Gaussian function. It is called β-decay constant.

During the γ-ray detection is possible that the γ-ray will have Compton scattering in the detector. Due to last two components in the peak shape description arise.

It is possible to put in the software both second and third function zero if they are not required. It is important to define background of whole spectrum after peak shape definition. Background can be defined with the Eq. 3.1:

$$Background = A + B * X + C * X^2 \quad (3.1)$$

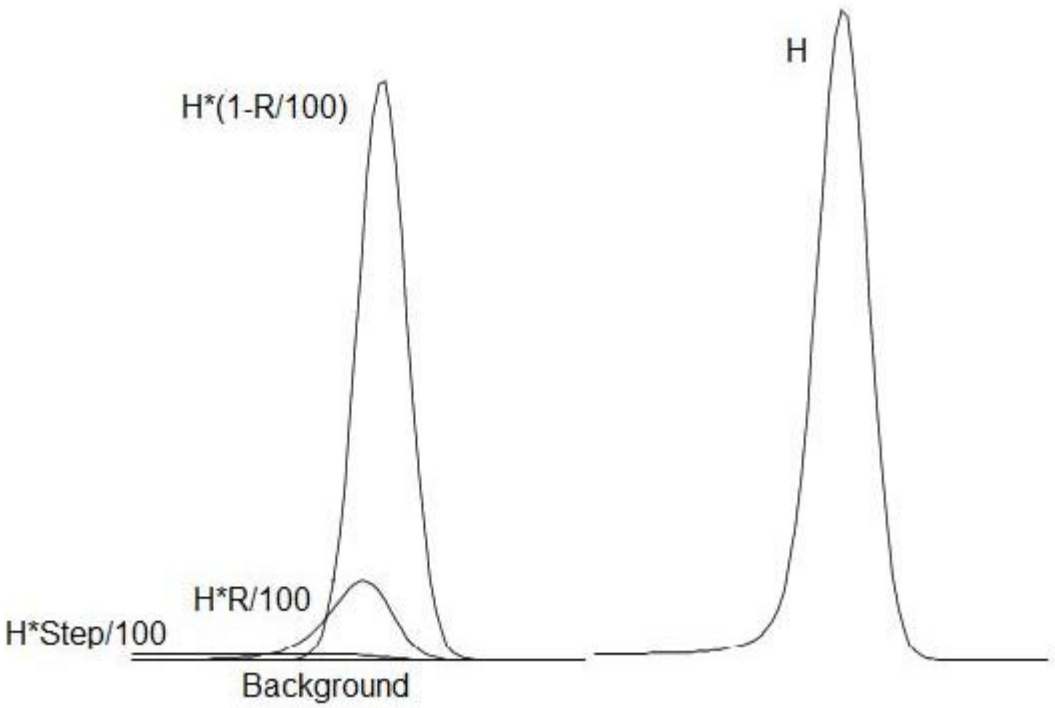

Figure 3.3 There components and how they make up total peak shape in the RadWare. Total height of the peak is "H". First component is Gaussian function with "H*(1-R/100)" part, second component is skewed Gaussian function with "H*R/100". Third component is "Step" function with part "H*Step/100".

In the background function A, B and C are parameters. Totally there are six parameters to describe background and peak shape to get best fitting results.

The variation of that parameters will give completely different results. I tried to find the optimal combination of the parameters for which the fitted result will have the least uncertainty. That was done during the ADCs test. Multiple cases were tried to find the solution.

It is possible not to fix the parameters, and let them free. I did that case as well, but I will not present that case, because it gave very bad results, compare to other cases.

3.1.2 Electronics

Electronics have a key role in the experimental nuclear physics. The faster electronics are required to handle data flow. Due to a lot of developments were done to find out the good electronics that will work properly with the detectors used in the experiment and can handle fast data flow.

The problem of the electronics is that they can implement additional uncertainty into the measured value that is why important to do good test and find out systematic uncertainty from electronics as well.

Due to test was done to compare too modules and find out can ORTEC module which is one of the best in the γ-ray spectroscopy be replaced with the new and fast MADC-32 module.

During the test both modules worked simultaneously. So the spectra of both modules were from the same ^{152}Eu source with the same period of time. Fig. 3.4 shows the spectrum from the MADC-32 module and Fig. 3.5 shows the spectrum from the ORTEC module. All labeled peaks have more than 1% intensity. The peaks energy intensity was taken from Ref. [38] and shown in the

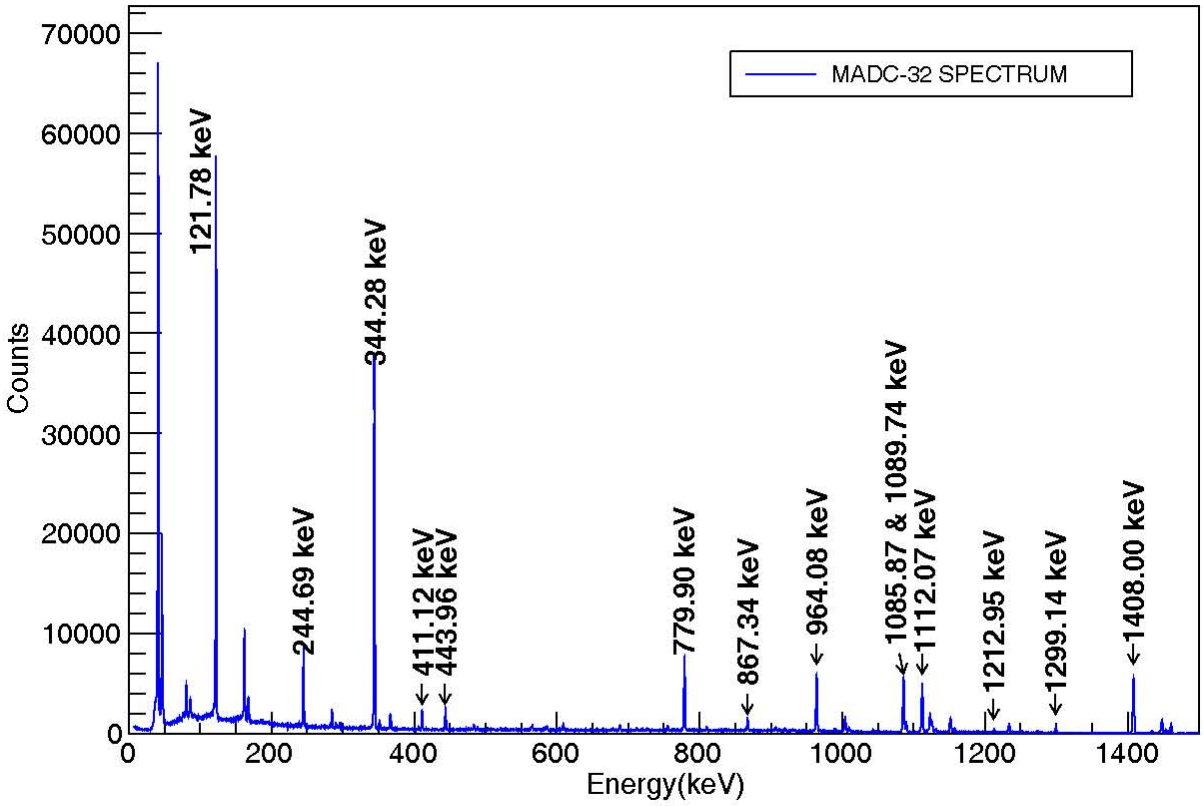

Figure 3.4 Spectrum of ^{152}Eu from Mesytec MADC-32 module.

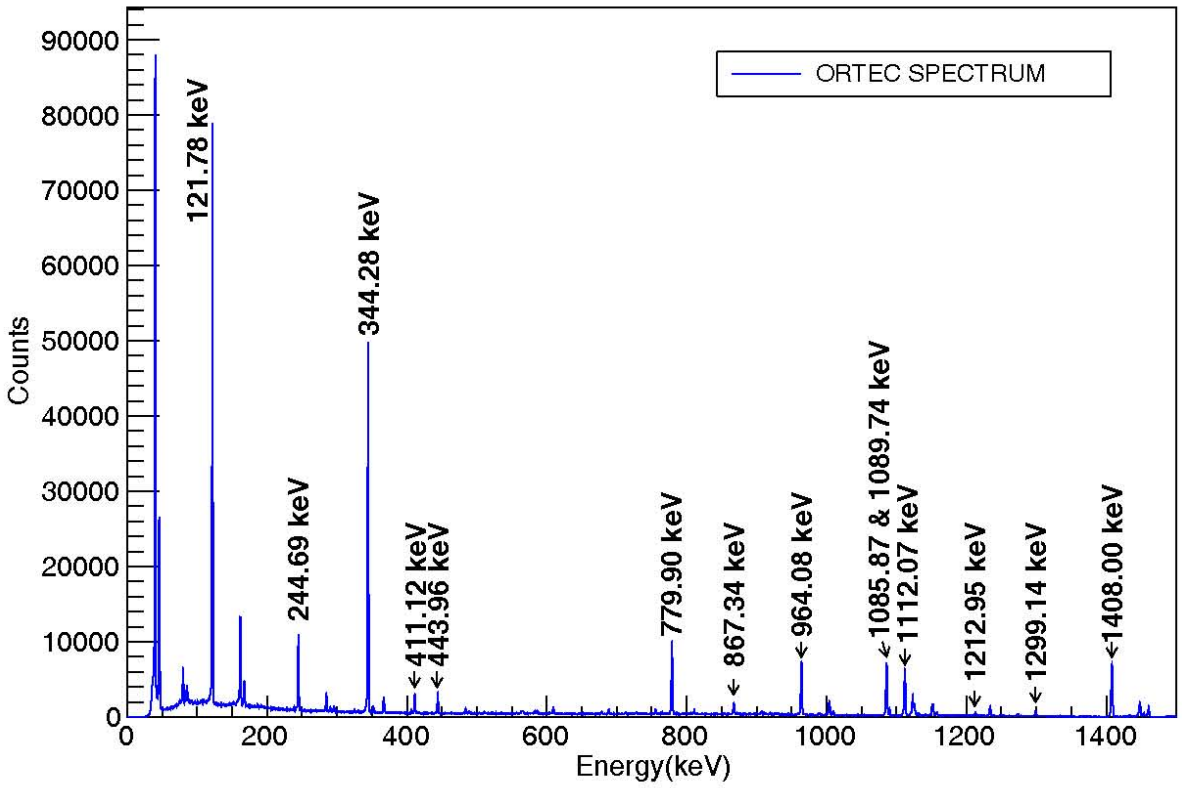

Figure 3.5 Spectrum of ^{152}Eu from ORTEC ASPec-927.

Table 3.1. The ^{152}Eu peaks cover the range from 100-1400 keV. This is working range for most low-energy nuclear physics experiments that need γ-ray spectroscopy. It is the working range for this experiments data analyzing as well.

Table 3.1 Energy and intensity of the peaks for the 152Eu that were used.

Energy (keV)	Intensity(%)	Energy (keV)	Intensity(%)	Energy (keV)	Intensity(%)
121.78	28.5	778.90	12.9	1089.74	1.7
244.69	7.6	867.38	4.2	1112.07	13.7
344.29	2.4	964.06	14.51	1299.14	1.6
411.12	2.2	1085.84	10.11	1408.01	20.9
443.96	2.8				

So if in this range the resolution and linearity of MADC-32 will be same as the ORTEC module, replacement can be done. The RadWare analyses for 4 different cases were done to get linearity and resolution measurements. The cases are: 1. C=R=β=Step=0, 2. B=C=R=β=0, 3. R=10, β=3, B=C=0, 4. R=10, β=3, B=Step=0. The best case that was found here later was used during experimental data analysis.

Fig. 3.6 shows the comparison of the Full Width at Half Maximum (FWHM) for MADC-32 module and Fig. 3.7 ORTEC ASPec-927 module for all RadWare cases. The FWHM shape for all cases is very similar for both modules. There is only small difference between two modules resolutions near the 1300 keV. It is due to the fact that the peak that was used has low intensity.

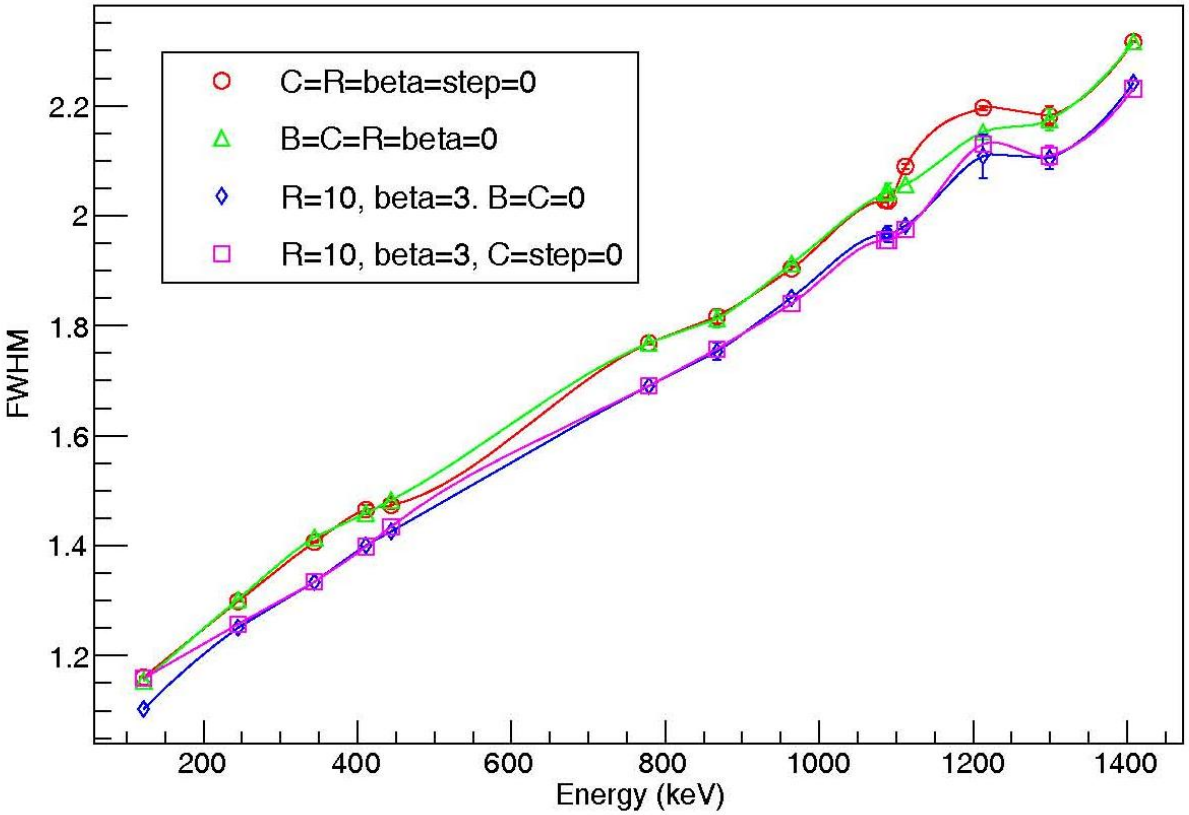

Figure 3.6 RadWare all cases resolution comparison for Mesytec MADC-32 module.

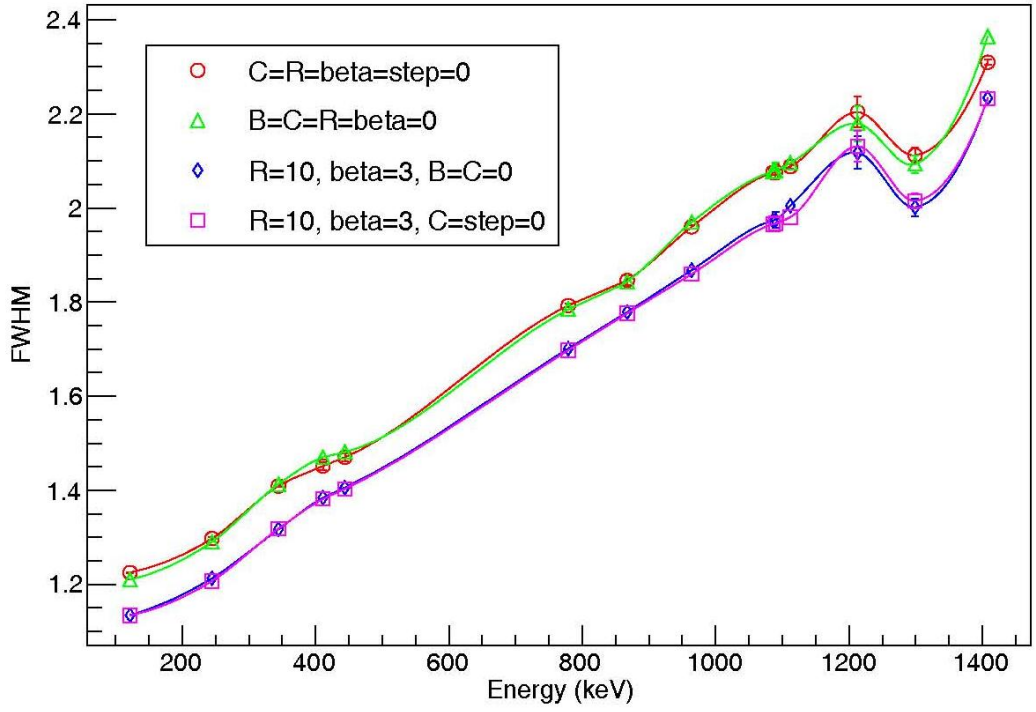

Figure 3.7 RadWare all cases resolution comparison for ORTEC ASPec-927.

Fig. 3.8 and Fig. 3.9 shows the linearity comparison for MADC-32 ORTEC modules respectively for all RadWare cases. The ORTEC APEC-927 linearity is very good. It is less than 0.1 keV in the whole range. On other hand, except of the B=C=R= β=0 case, all others have similar structure for MADC-32. In the low-energy tail the linearity for MADC-32 increase until 0.45 keV.

In the range 200-1400 keV both modules linearity is less than 0.1 keV. The best case from all this results is achieved, when for Radware case 3. That case parameters were used during experimental data analysis.

Both modules FWHM and linearity comparison for this case is shown in the Fig. 3.8 and Fig. 3.9 respectively. FWHM matched together perfectly except the point near 1300 keV which was discussed before.

In the low-energy range (100 keV - 200 keV) MADC-32 linearity is increasing too much, but in the rest part it can be used. During linearity measurements energy depends from channel number linearly in the following comparison. In this experimental data analysis this precision is enough, because there is only few peaks in that range.

It is possible to reach better results for linearity of MADC-32 module as well if in place of linear fit second order polynomial dependence will be used. I did that as well to show that the module is not usefully only on certain experiment, but it can be used for any other experiment as well.

The second order polynomial fit was done for the chosen case (R=10, β=3, B=C=0) and comparison with the linear dependence is shown the Fig. 3.10. In this case the linearity for the MADC-32 module is also less than 0.1 keV. So the linearity for MADC-32 can be reached to ORTEC ASPec-927 module linearity if second order polynomial will be used.

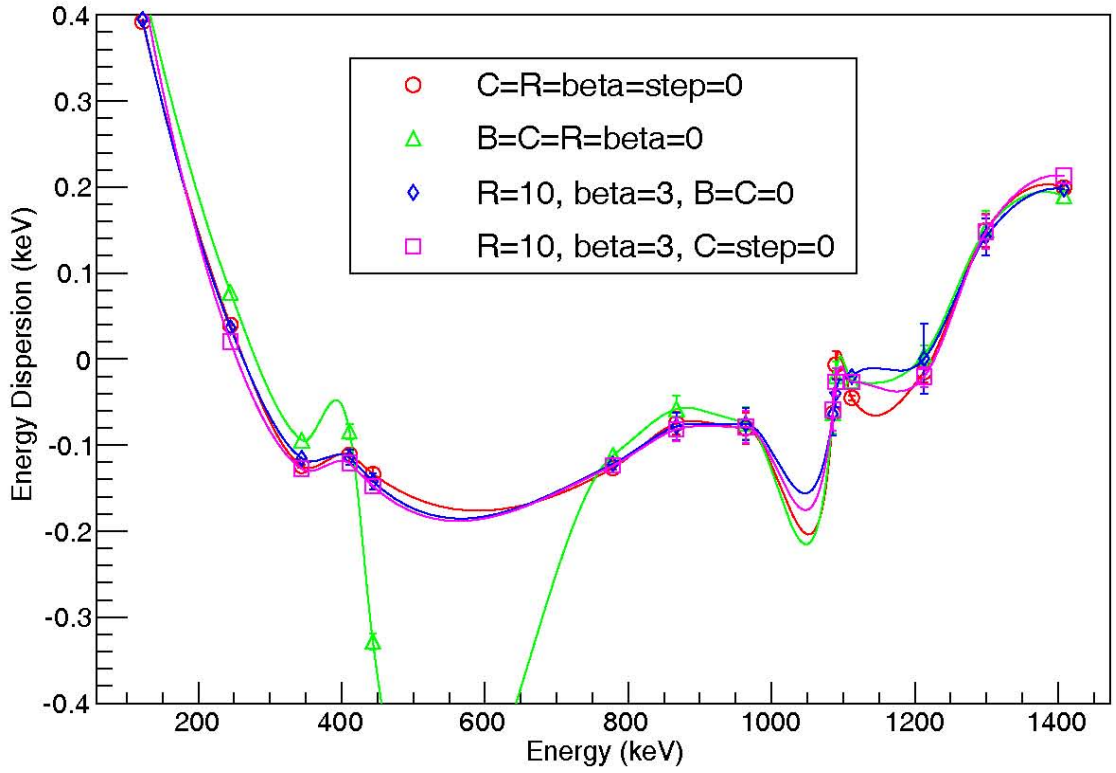

Figure 3.8 RadWare all cases linearity comparison for Mesytec MADC-32 module.

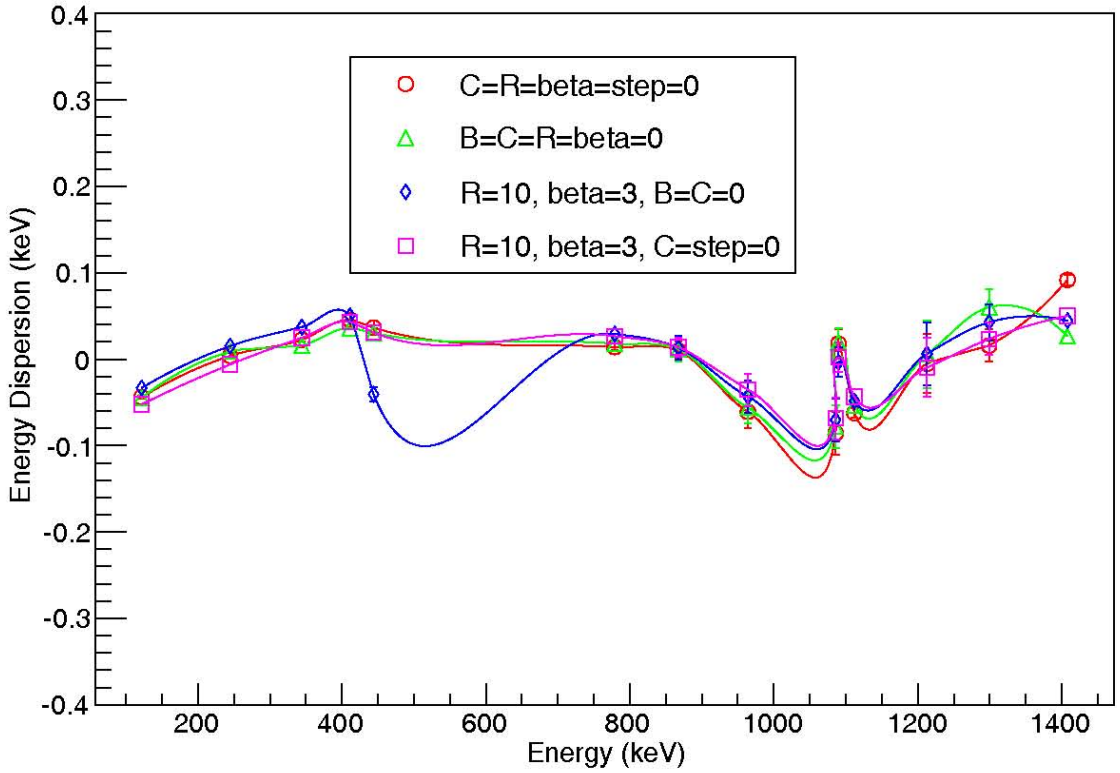

Figure 3.9 RadWare all cases linearity comparison for ORTEC ASPec-927.

After verifying that the module can be used during the experiment and method was described how it will be used. The code was written to convert data from basic system style file, which is very hard for analyzing data and has a lot of problems, into ROOT file and work in the ROOT space, which is much easier. The code takes into account the data structure of the module, compares with already know values and save values into root file.

All this corrections were detailed explained and published in the Armenian Journal of Physics and can be found in the Ref. [32].

This code is very important as it help to remove all events that have bad data event structure and can bring some random numbers into the real data.

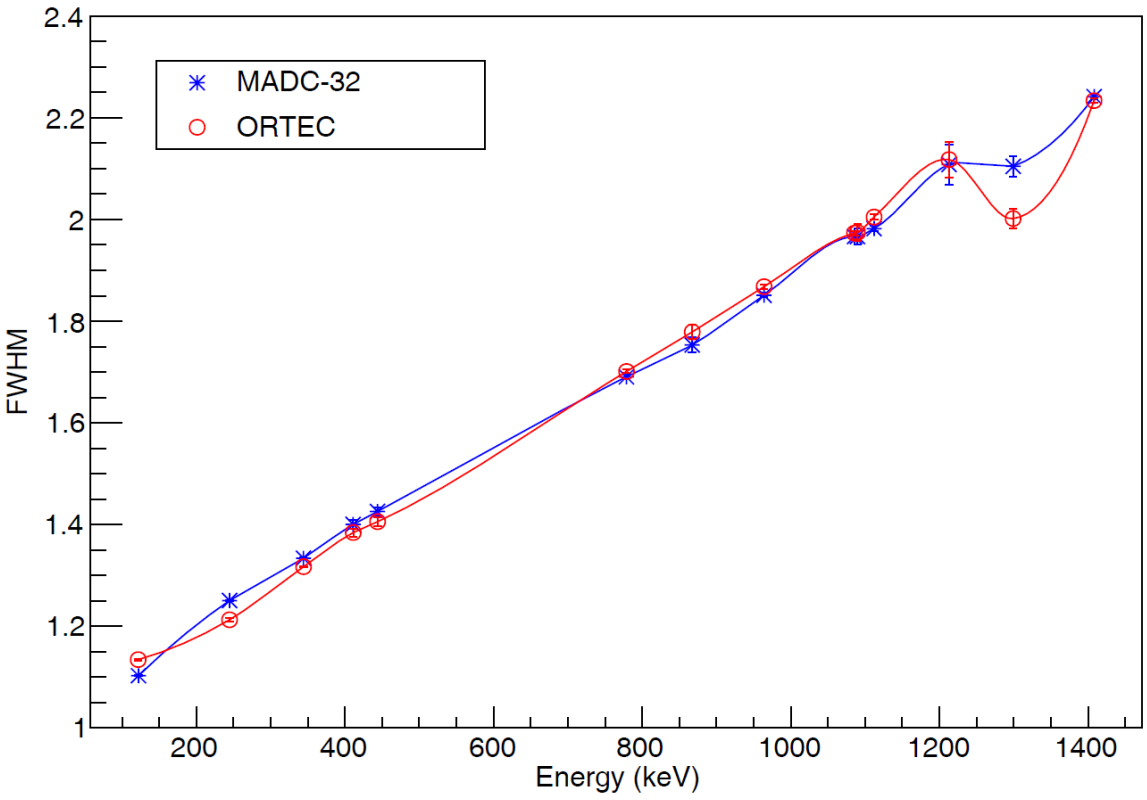

Figure 3.10 Resolution comparison of two modules.

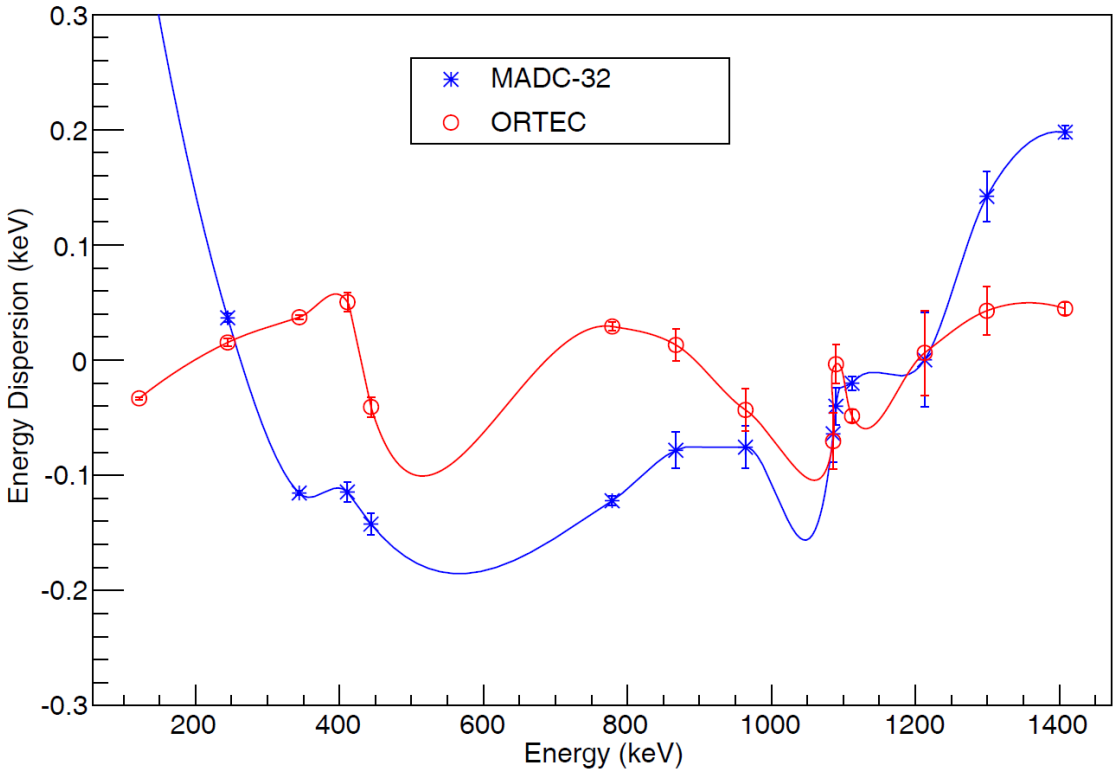

Figure 3.11 Linearity comparison of two modules.

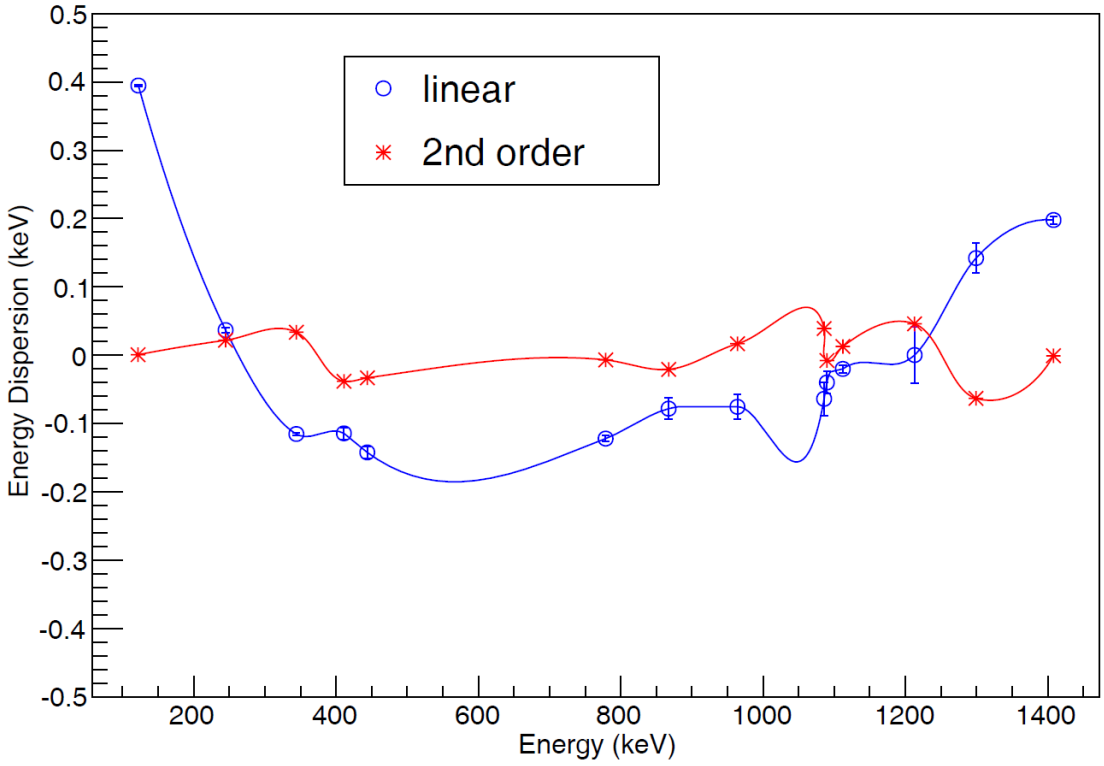

Figure 3.12 Comparison between linear and second order polynomial energy

I did some modifications on this code to make sure that it will check not just some know, but all known values and print out the percentage of bad events to get idea how much bad events the module will create.

That can be used later for other experiments as well to know approximately how much data is not reliable.

3.2 Efficiency Measurements

Efficiency measurements are important for the experiments in which Yield measurements are necessary. As Internal Conversion Coefficient (ICC) should be measured in the following experiment, multiple functions were used to find best solution for the efficiency curve. Both Si(Li) and HPGe efficiencies functions are required to define. The ^{152}Eu source was used for HPGe detectors efficiency measurements with the same peaks that was used for the test (Table 3.1). Two radioactive sources ^{133}Ba and ^{207}Bi were used for Si(Li) efficiency curve measurements. The energies and intensities of the peaks are shown in the Table 3.2 [38].

The range for the e_ciency curve for HPGe is from 120 keV to 1409 keV and for the Si(Li) is from 124 keV to 1047 keV. This range is enough for all peaks of interests that were measured for ^{195,196}Au.

Table 3.2 133Ba and 207Bi peaks energies and intensities used for Si(Li) efficiency measurements.

^{133}Ba		^{207}Bi	
Energy (keV)	Intensity (%)	Energy (keV)	Intensity (%)
124.62	0.15	481.69	1.54
240.41	0.33	553.84	0.44
266.87	0.68	975.65	7.08
320.03	1.31	1047.79	1.84

Efficiency curves are the Eq. 3.2 and Eq. 3.3 for the HPGe and the Si(Li) detectors respectively.

$$\ln(\epsilon) = p0 - \left(p1 + p2 * e^{-p3*\ln(E)}\right) * e^{-p4*\ln(E)} * \ln(\ln(E)) \quad (3.2)$$

$$\ln(\epsilon) = p0 + p1 * \ln(E) + p2 * E^2 \quad (3.3)$$

In the Eq. 3.2 p0, p1, p2, p3, p4 and in the Eq. 3.3 p0, p1, p2 are fitting parameters. Table 3.3 shows the parameters values for one of the detectors for each type.

Table 3.3 Parameters for one of the detectors for each type.

HPGe		Si(Li)	
Parameter	Value	Parameter	Value
p0	-39.7447	p0	-25.18
p1	-11.1026	p1	0.65
p2	-33.3276	p2	$2.05*10^{-7}$
p3	0.2295		
p4	0.0024		

The Yield (Y) will be equal peak counts (N) divided to efficiency at that Energy (ϵ) (Eq. 3.4).

$$Y = \frac{N}{\epsilon} \quad (3.4)$$

As there is possible that the conversion electron will be from different shells than for each of them the Yield should be measured. Than each of them can be divided onto the γ-ray Yield and the conversion coefficient will be

calculated for each shell. Later that conversion coefficients can be compared with the theory and do assignment of parity and spin.

As there is multiple detectors for each type total number of counts was divided to total efficiency at that energy.

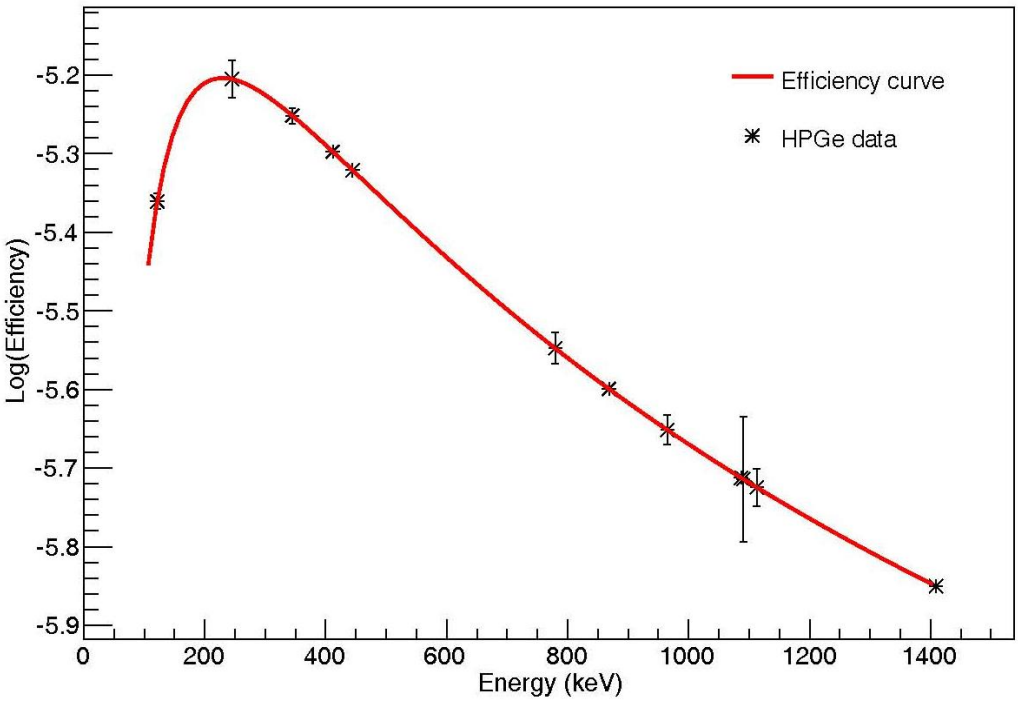

Figure 3.13 Comparison between linear and second order polynomial energy from channel dependence fitting for Mesytec MADC-32 module.

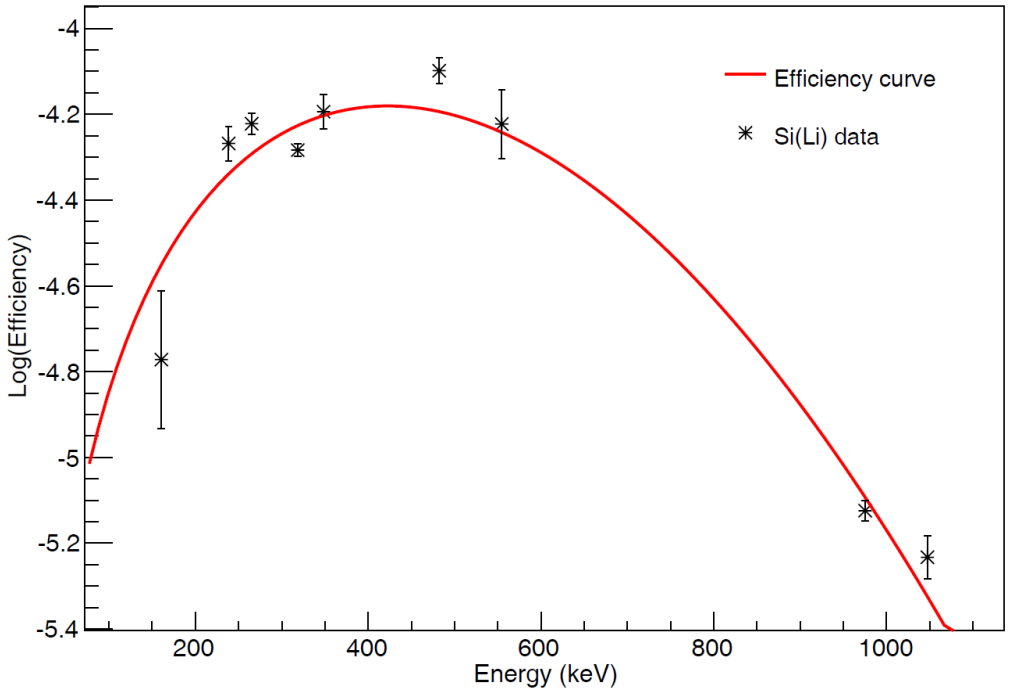

Figure 3.14 Comparison between linear and second order polynomial energy from channel dependence fitting for Mesytec MADC-32 module.

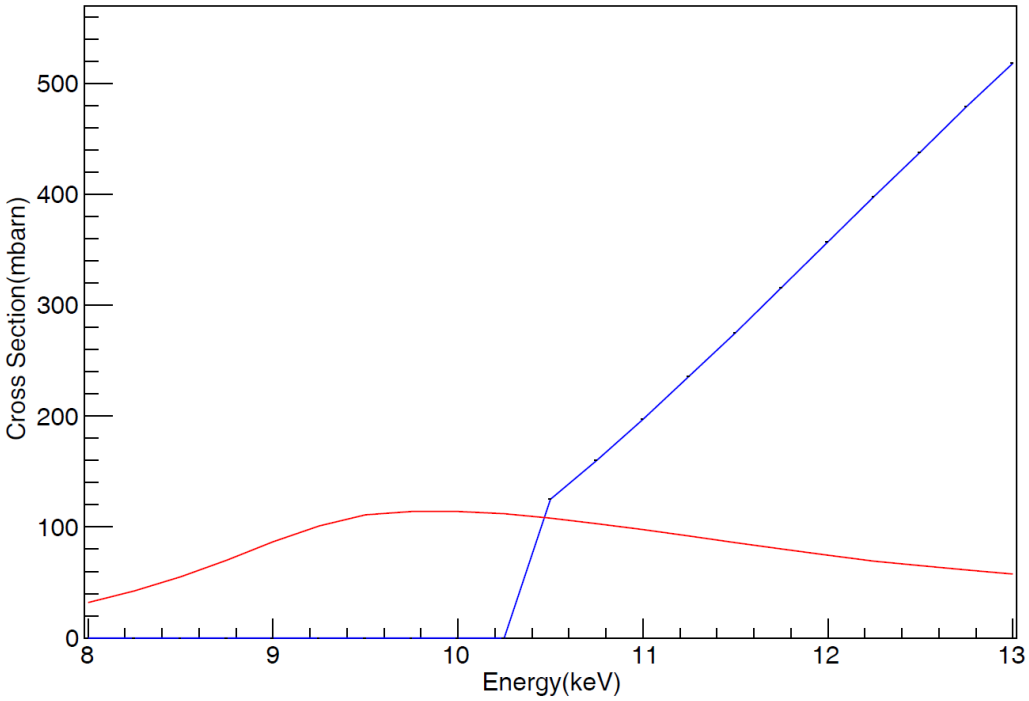

Figure 3.15 TALYS cross section calculation for both ^{196}Pt(p,n)^{196}Au (red) and ^{196}Pt(p,2n)^{195}Au (blue).

3.3 Experimental Measurements

Electrons can be from different shells so for each shell electron Yield should be calculated. Eq. 3.5 shows the ICC(α) calculation method.

$$\alpha = \frac{Yield_e}{Yield_\gamma} \tag{3.5}$$

As there are multiple detectors for each type. All of them were attached together to do γ-ray or electron spectroscopy to measure Yield for both electron and γ-ray. Attached HPGe and Si(Li) spectra are shown in the Fig. 3.18(a) and Fig. 3.18(b) respectively. Peaks in the spectra are shifted and the attachments are only possible if all detectors are calibrated.

The cross section for ^{196}Pt(p,n)^{196}Au reaction is comparably low for from ^{196}Pt(p,2n)^{195}Au. Due to only ^{195}Au gammas can be seen in the Fig. 3.18. The labelled peaks belong to ^{195}Au nucleus. The Fig. 3.15 is the TALYS calculation for the cross section for both reactions. The red line is the cross section for the (p,n) reaction and it is dominating until some point, but it does not vary too much. On the other hand, the blue line which corresponds to the (p,2n) reaction has starting point it is around 10.3 MeV until that energy the channel is not open as the energy is not enough to separate two neutrons. The beam energy was 12 MeV and at that point the cross section to produce ^{195}Au dominates around from times. Energy was chosen above that point to have both reactions open and with the hardware coincidence try to get the ^{196}Au peaks. The background was too high for the detectors was too high and the peaks did not appear.

Only having the raw spectrum is not enough to analyze all peaks and find new transition if they exist. Due to gates were used to study transitions. That gates also help to find the correlation between the peaks and make sure which peaks relate to the ^{195}Au.

Except γ-peak gates, it is possible to do timing gate as well, to find out the prompt peaks. As the buncher was used during the experiment it can be used to do time-of-flight gates. The buncher is sending start signal and then detector as a stop signal. Time-Digital Converter (TDC) reads the signals from buncher and detectors. Then delay between the buncher and detector can be constructed and can be drawn as a function. Fig. 3.16 and 3.17 shows the timing spectra for both single HPGe and single Si(Li) detectors respectively.

It can be seen a sharp peak for both detectors around 1300 ns. It is a called prompt peak and it is relative to all γ-rays and electrons that are coming from nuclei instant decay. Than for the HPGe detector there is a bump from 1500 ns to 2800 ns it is the signals from the long lived nuclei decay. There is no that kind of part for the Si(Li) detector as most of the electrons are from decay of nuclei which are very fast. Rest in both spectrum is background. Using gates on the prompt peaks will make spectra cleaner from background, and only short lived particles will be taken into account. This gates were applied in addition to all γ-ray gates to make peak/background ratio bigger.

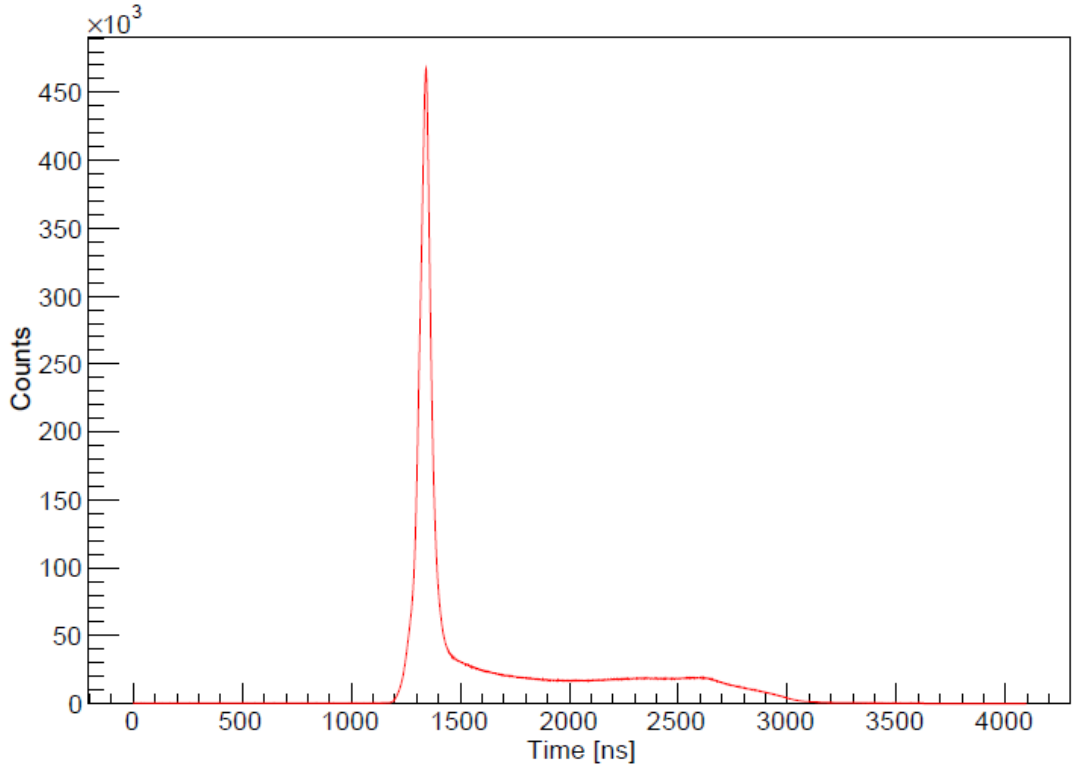

Figure 3.16 Delay function between buncher and one of the HPGe detector.

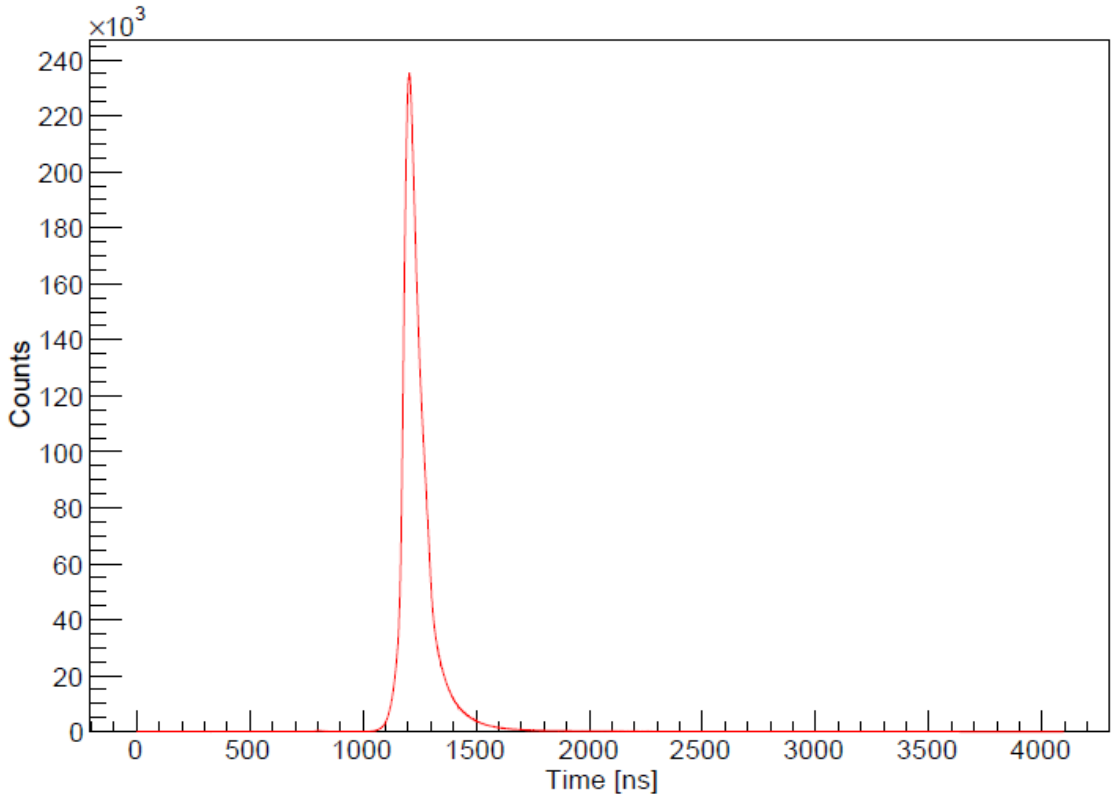

Figure 3.17 Delay function between buncher and one of the Si(Li) detector.

As there was two HPGe detectors during the experiment, so same γ-transition gate was done for both spectra and then total Yields were measured. With the following way the statistics can be increased twice. If in one of the HPGe detectors the signal appear that the Si(Li) spectrum should take into account that event.

Examples of gated spectra area shown in Fig. 3.19. Fig. 3.19(a) is the 261 keV γ-peak gate where the 285 keV, 441 keV and 693 keV γ-ray transitions are prominent in the spectrum. The 441 keV (Fig. 3.19 (b)) gate shows as expected the 261 keV and 285 keV transitions.

The γ-transitions from the levels at 1396 keV→954 keV→261 keV→0 emitting a 441 keV, 693 keV and 261 keV γ-rays, were previously known. Only way to explain additional 285 keV transition and that unobserved 693 keV transition in the 441 keV gate is to assume that there is another decay chain 988 keV→703 keV→261 keV→0 with 285 keV, 441 keV and 261 keV transitions. The 987 keV and 703 keV levels are new in this study. Conversion coefficient measurements showed that the new 441 keV transition is an M1 transition. The 285 keV line is probably an M1+(E2) transition. A partial level scheme with the new spin and multi polarities for those transitions is shown in the Fig. 3.21.

Fig. 3.19(c) shows the γ-ray spectrum for a 549 keV gate. Transitions 338 keV, 439 keV, 519 keV, 570 keV, and 629 keV are observed. The level scheme for ^{195}Au corresponding to this gate is shown in the Fig. 3.20.

In this case, there should be another transition with 549 keV energy that decays to the 439 keV energy level, otherwise the 439 keV transition would not be observed since it is not in coincidence with the 549 keV transition. That transition is therefore placed at a new level at 987 keV.

Most of the transitions are in the range from the 100 keV to 900 keV for HPGe. It is due to low statistics at higher energy range. Background is too high

and peaks cannot be seen. There is a huge background in a low energy part most of that background is just X-rays and not γ-rays.

In the Si(Li) detectors peaks are in the 150 keV to 450 keV. Again same problem is here in high energy part statistics is very low. In the low energy range, on the other hand, are huge background coming from atom. During the reaction proton scatters on electron and electron gets enough energy to come out from atom and be detected in the detectors. That is why there is a huge exponential background in the low energy part. Due to some low-lying peak cannot be seen. For example, 180 keV transitions L-shell electron peak can be seen as its energy will be around 165 keV, but K-shell electron cannot be seen as it is around 100 keV.

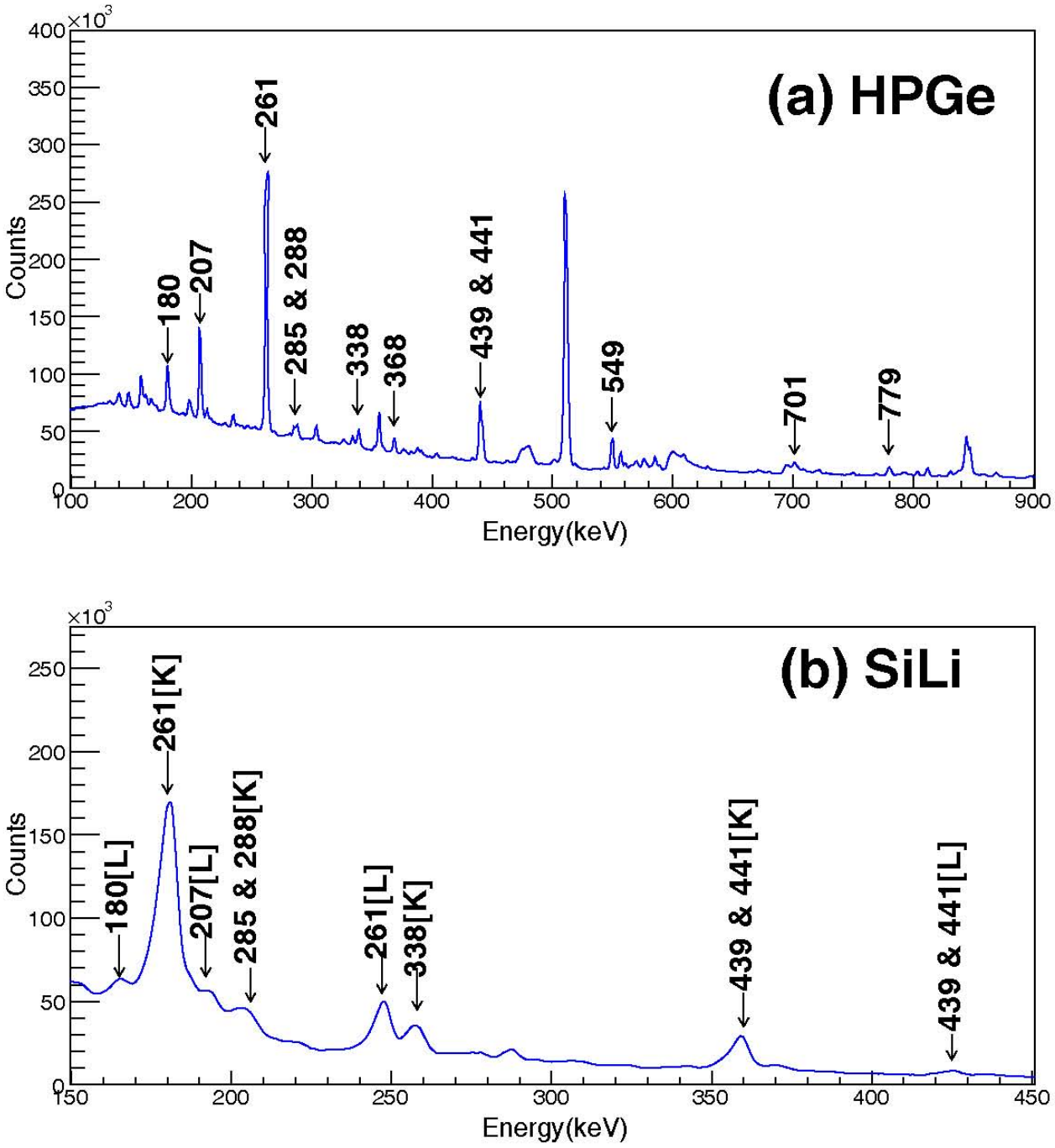

Figure 3.18 Sample spectra of the observed γ-rays and electrons. Section (a) corresponds to a γ-ray spectrum from one of the HPGe detectors. Section (b) is a part of the electron spectrum between 150-450 keV measured by the sum of all the Si(Li) detectors. All labelled peaks in both spectra belong to the ^{195}Au nucleus.

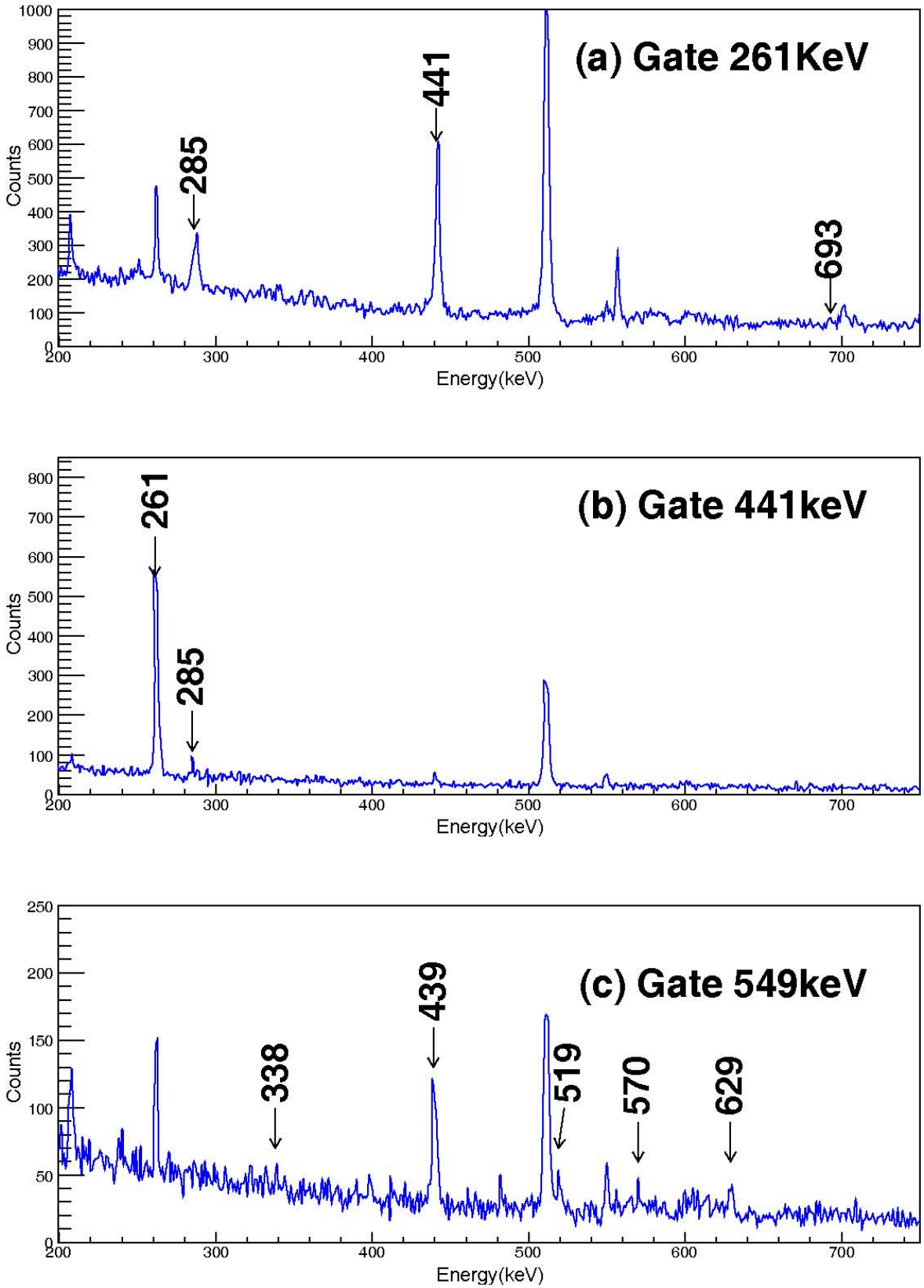

Figure 3.19 Comparison between linear and second order polynomial energy from channel dependence fitting for Mesytec MADC-32 module.

With the following two examples was shown the existence of new energy level 987 keV, which decay either to another new level 702 keV with the 285 keV γ-ray emission or already known 439 keV level with the 549 keV transition.

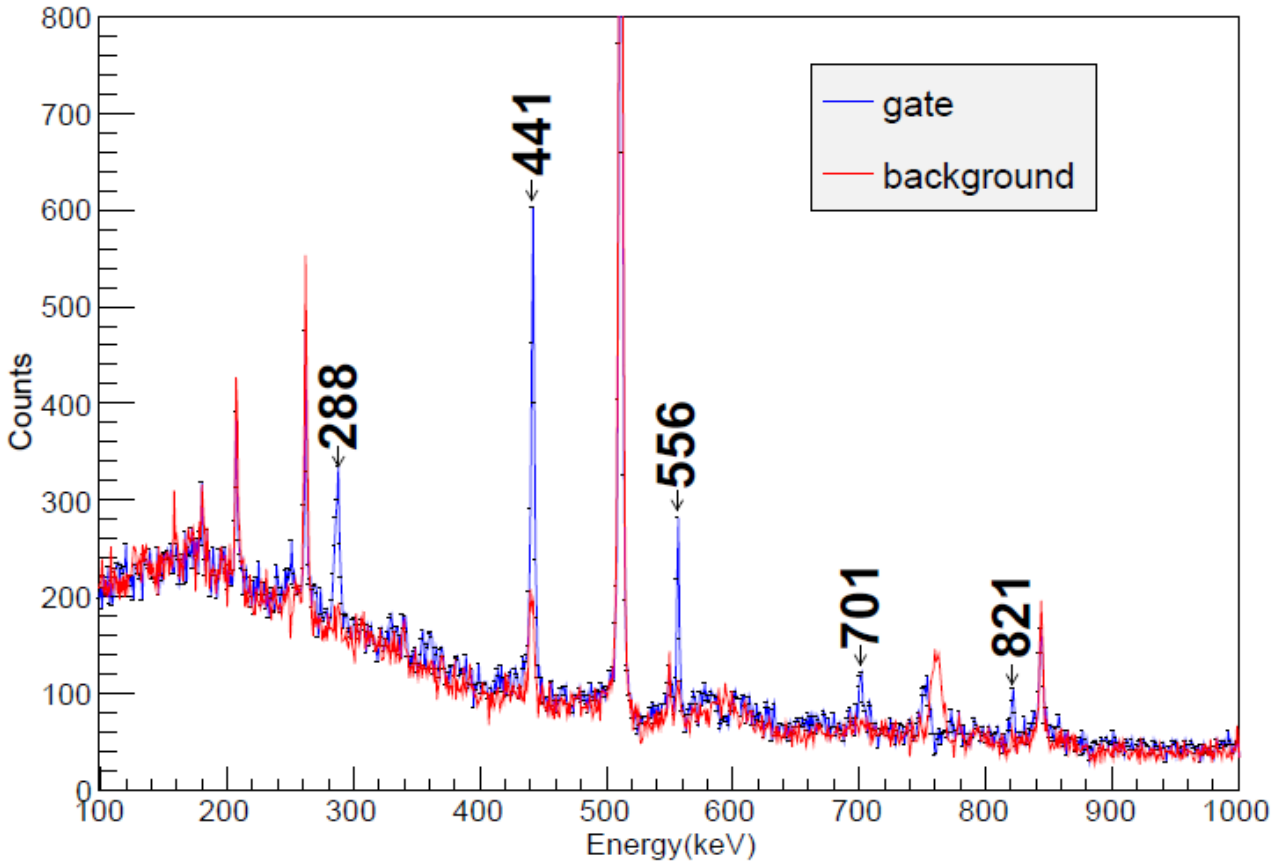

Figure 3.20 Gate on the 261 keV γ-peak and background gate.

In the Fig. 3.20 different gates have a lot of peaks that was not taken into account as gate related. It was proven that the gates doesn't relate to that peaks with the following way.

Gate on the peak was set and then with the similar statistics nearby was set another gate on background and two gates were compared together. As the statistics is not exactly same the gates statistics was normalizes.

For example if the peak of the interest has P_1 counts under the first gate with N_1 statistics, and P_2 counts under the second gate with the N_2 statistics. The P_1 was normalized with the following equation:

$$P_1 = \frac{N_1}{N_2} P_2 \tag{3.6}$$

With this normalization all spectra can be normalized and any peak that is in the γ-ray gate and is not on the background gate is peak related. The Fig. 3.20 shows an example. The γ-ray is 261 keV and related background. All labeled peaks are related to that peak and are from the 195Au excited levels.

The other possible thing is that the peaks can be shifted when the gate changes the position. The peak example is in the Fig. 3.20 around 770 keV. The peak on the background and the 261 keV related gates are very close. That is Compton scattering peak and does not have any relation with ^{195}Au. This is good way to find out all peak detailed information.

In the Fig. 3.21 and the Fig. 3.21 the black color is for new transitions and levels, the red color is gated γ-ray energy and the blue is new transitions and energy levels.

There is also another two new levels 1120 keV and the 1178 keV in the Fig. 3.19 which were observed during the data analysis.

After identifying all the transitions the ICCs were measured. Table 3.4 shows ICC for all transitions up to 1500 keV excitation energy for both ^{195}Pt(p,n) and ^{196}Pt(p,2n) reactions.

Most ICCs match together within error bars, but there are some cases that are too off. The ones that does not match and new state spin and multi polarity should be assigned will be discussed below.

Let's start from the unmatched ICCs. That are the mostly ICCs for the L shell. Transition are 440.86 keV from the level 702.95 keV, 285.3 keV from

the level 987.78 keV, 338.91 keV from the level 1407.85 keV. These transitions have very low statistics after gates the statistics is even less. The electron peak for the transitions sometimes is very difficult to identify due to huge background. That is why the following ICCs does not match.

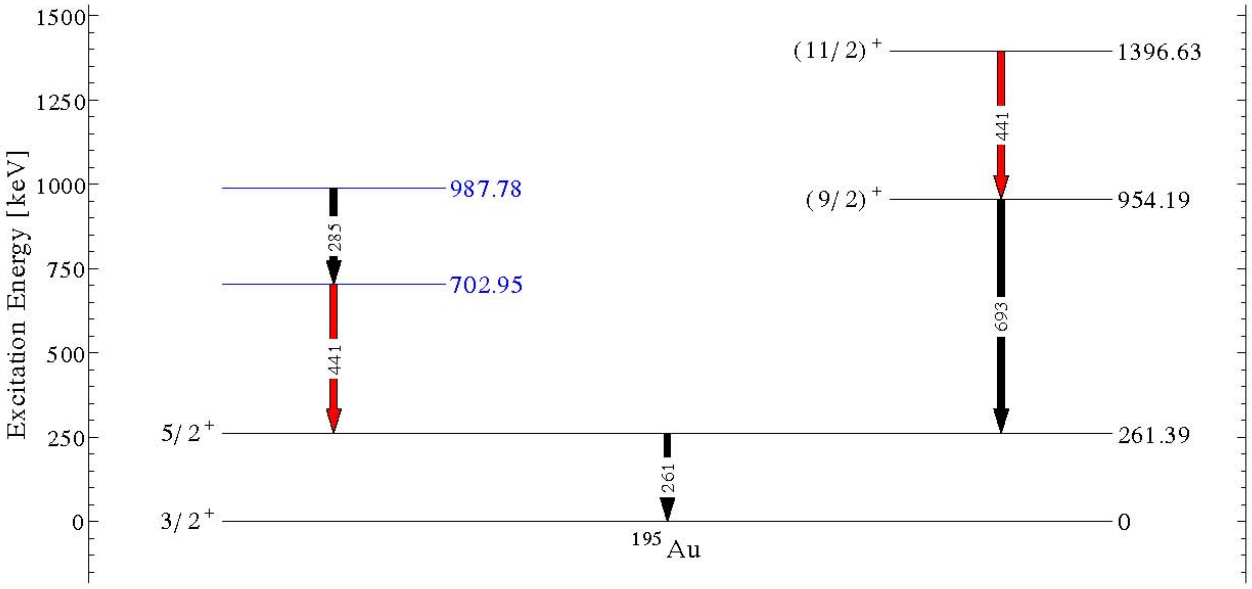

Figure 3.21 Partial level schemes constructed from the 261 keV and 441 keV gamma-ray gates. Blue levels indicate the new levels found in ^{195}Au. The red arrow indicate the gating transitions.

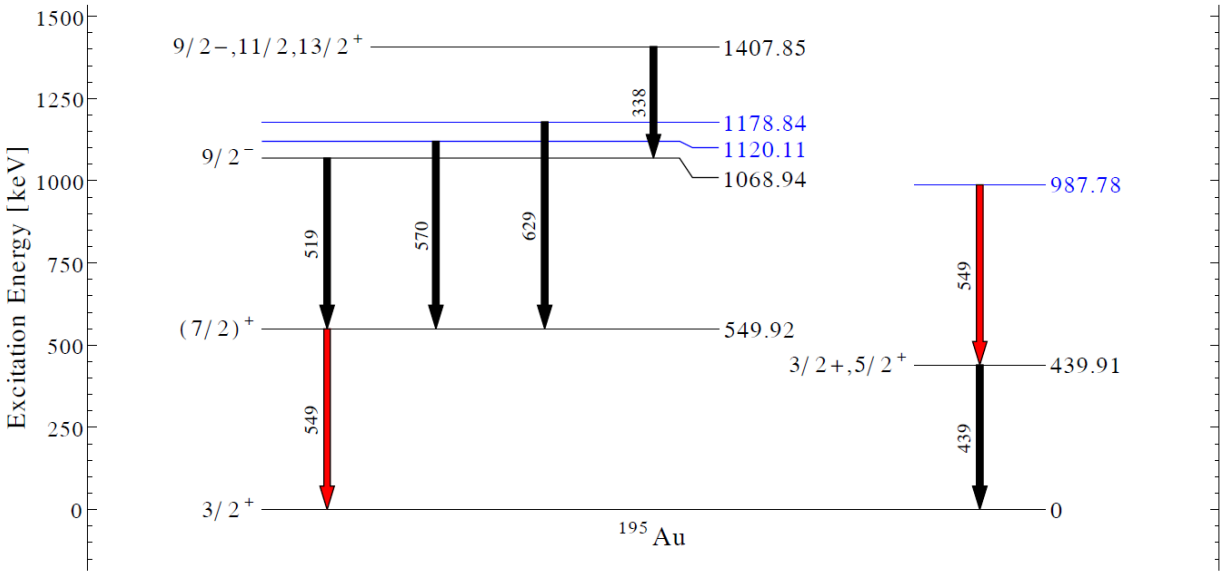

Figure 3.22 A partial level scheme constructed from the 549 keV gamma-ray gate. Blue levels indicate the new levels found in 195Au. The red arrows indicate the gating transitions.

Table 3.4 Internal Conversion Coe_cients from reactions ^{195}Pt(p,n) and ^{196}Pt(p,2n) with beam energy 7.75 MeV and 12 MeV respectively.

E_{level}[keV]	E_γ[keV]	E_e[keV]	Multipolarity	^{195}Pt(p,n) coefficient	^{196}Pt(p,2n) coefficient
241.06	180.17(2)	165.87[L]	M1	0.16(2)	0.23(3)
261.39	261.39(1)	180.69[K]	M1+E2	0.37(4)	0.42(4)
		247.06[L]		0.062(6)	0.059(6)
439.58	439.58(19)	358.88[K]	M1+E2	0.091(10)	0.14(3)
		425.28[L]		0.011(1)	0.013(7)
525.62	207.12(1)	126.42[K]	E2	0.11(3)	
		192.82[L]		0.23(3)	0.25(3)
549.92	288.15(19)	207.45[K]	M1	<0.46	<0.52
	549.92(23)	469.22[K]	M1+E2	0.020(8)	0.030(8)
702.95[1]	440.86(13)[1]	360.16[K]	M1	0.13(2)	0.11(1)

		426.56[L]		0.012(2)	0.024(3)
817.76	556.37(11)	475.67[K]	M1+E2	0.038(6)	0.062(8)
831.49[1]	391.5(4)[1]	310.80[K]	M2+E3	0.27(6)	0.54(14)
		377.20[L]		0.040(18)	0.045(21)
879.36	560.78(8)	480.08[K]	M1	0.050(6)	0.050(5)
894.41	368.87(1)	287.17[K]	M1	0.14(2)	0.16(2)
954.19	692.8(4)	612.10[K]	M1+(E2)	0.030(6)	
962.93[1]	701.54(21)[1]	620.84[K]	M1	0.029(14)	0.025(6)
987.78[1]	285.3(3)[1]	204.60[K]	M1+(E2)	0.60(15)	0.80(14)
		271.00[L]		0.30(7)	0.06(2)
	549.4(2)[1]	468.70[K]	M1+E2	0.024(8)	0.044(7)
1068.94	519.4(4)	438.70[K]	M2+E3	0.12(5)	0.024(9)
	542.9(4)	460.20[K]	M1+E2	0.030(15)	0.077(13)
1111.45	585.49(11)	504.79[K]	M1+E2	0.017(8)	0.022(4)
1120.11[1]	570.3(6)[1]	489.60[K]	M1+E2	0.047(62)	0.039(17)
	680.2(6)[1]	599.50[K]	M1	0.050(17)	0.075(18)
1178.84[1]	629.3(4)[1]	548.60[K]	M1	0.045(16)	0.069(16)
1281.21	386.8(3)	306.10[K]	M1+E2	0.10(3)	0.56(21)
		372.10[L]		0.15(3)	0.42(16)
1305.11[1]	779.49(23)[1]	698.79[K]	M1	0.032(9)	
1346.51	452.1(5)	371.40[K]	M1	0.082(3)	
1407.85	338.91(3)	258.21[K]	M2+E3	0.32(4)	0.51(6)
		324.21[L]			0.036(5)
1442.95	360.6(4)	279.90[K]	M1	0.19(6)	
		346.30[L]		0.36(23)	0.043(8)
1489.76	672.0(4)	591.30[K]	M1	0.041(18)	

[1]Transitions and energy levels that were measured in this work and Ref.[14].

There is another transition 519.4 keV from the level 1068.94 keV. This transition K-shell ICC is not matching. The problem is that the peak is very close to 511 keV annihilation peak and even after gates the annihilation peak is still exist. It is very difficult to separate for (p,n) reaction. On the other hand,

during (p,2n) reaction hardware coincidence was used and that helped to decrease the 511 keV annihilation peak dramatically. That is why the ICC from the (p,2n) reaction is more reliable.

Results of measured conversion coefficients were published in the Armenian Journal of Physics and can be found from the Ref. [35].

Another similar problem is with the 570.3 keV transition from the 1120.11 keV level. Again there is a strong background peak which decrease during hardware coincidence. So the (p,2n) reaction ICC is again more reliable.

Now about new levels spin and parity assignments.

Level 702.95 keV:

The following level has one de-excitation is 440.36 keV transition. ICC measurements showed that it is M1 transition. So there is no parity change and spin change will be $\Delta J = 0, \pm 1$. Final state has $5/2^+$ spin and parity so this level will have the $3/2^+$, $5/2^+$ or $7/2^+$ spin and parity.

Level 831.49 keV:

This level de-excites with the 391.5 keV transition. ICC measurements showed that it is M2+E3 transition. So there is parity change and spin change will be $\Delta J = 0, \pm 1, \pm 2$ for M2 and $\Delta J = 0, \pm 1, \pm 2, \pm 3$ for E3. Final level is 439.91 keV with 3/2+ or 5/2+ spin and parity. So the candidates for this level spin and parity are $1/2^-$, $3/2^-$, $5/2^-$, $7/2^-$, $9/2^-$ or $11/2^-$.

Level 962.93 keV:

Transition from this level is 701.54 keV which is M1 transition. Final level is 261.39 keV level with the $5/2^+$ spin and parity. So the level has possible $3/2^+$, $5/2^+$ or $7/2^+$ spin and parity candidates.

Level 987.78 keV:

This level has two transitions one of the transitions is 258.3 keV which is the M1+(E2) transition. Final level is the 702.95 keV level which is new so there is only possible candidates for spin and parity. Due there is big uncertainty for this transition. Second transition is 549.4 which is M1+E2. The final level for this transition is 439.91 keV level with $3/2^+$ or $5/2^+$ spin and parity. So the possible candidates of this level from this transition will be $1/2^+$, $3/2^+$,$5/2^+$,7/2+ or 9/2+.

Level 1120.11 keV:

This level again has two transitions. First one is the 570.3 keV which is M1+E2 and the final level has $7/2^+$ spin and parity. So the spin and parity candidates will be $3/2^+$, $5/2^+$, $7/2^+$, $9/2^+$ or $11/2^+$. Second transition is the 680.2 keV which is only M1 and the final state has $3/2^+$ or $5/2^+$ spin and parity. So the possible candidates are $1/2^+$, $3/2^+$, $5/2^+$ or $7/2^+$. So if only matched candidates will be taken than they are $3/2^+$, $5/2^+$ or $7/2^+$.

Level 1305.11 keV:

This is last new level for which ICC was measured. The transition is 779.49 keV and is M1 transition. Final level is the 525.62 keV level with the $7/2^-$ spin and parity. This level's spin and parity possible candidates will be $5/2^-$, $7/2^-$ or $9/2^-$.

It is only possible to do spin and parity predictions with ICCs. The best way to measure spin and polarity for this states is to measure angular distributions.

Final level scheme is shown in the Fig. 3.23 with all assignments. New levels do not have the spin and parity shown as there is too much candidates. In the figure red color is for new levels and transitions, black is for already known transitions and levels and dashed transitions are known, but were not observed in the following experiment.

Totally there is 10 new transitions and 8 new levels observed. Most of them were observed in the Ref. [14], but one of the transitions (549 keV from the 1068 keV energy level) was only observed during this experiment. The level 1475.22 keV was not discussed as the transition energy is too high for Si(Li) configuration that was used. That is why the ICC is not available for this transition.

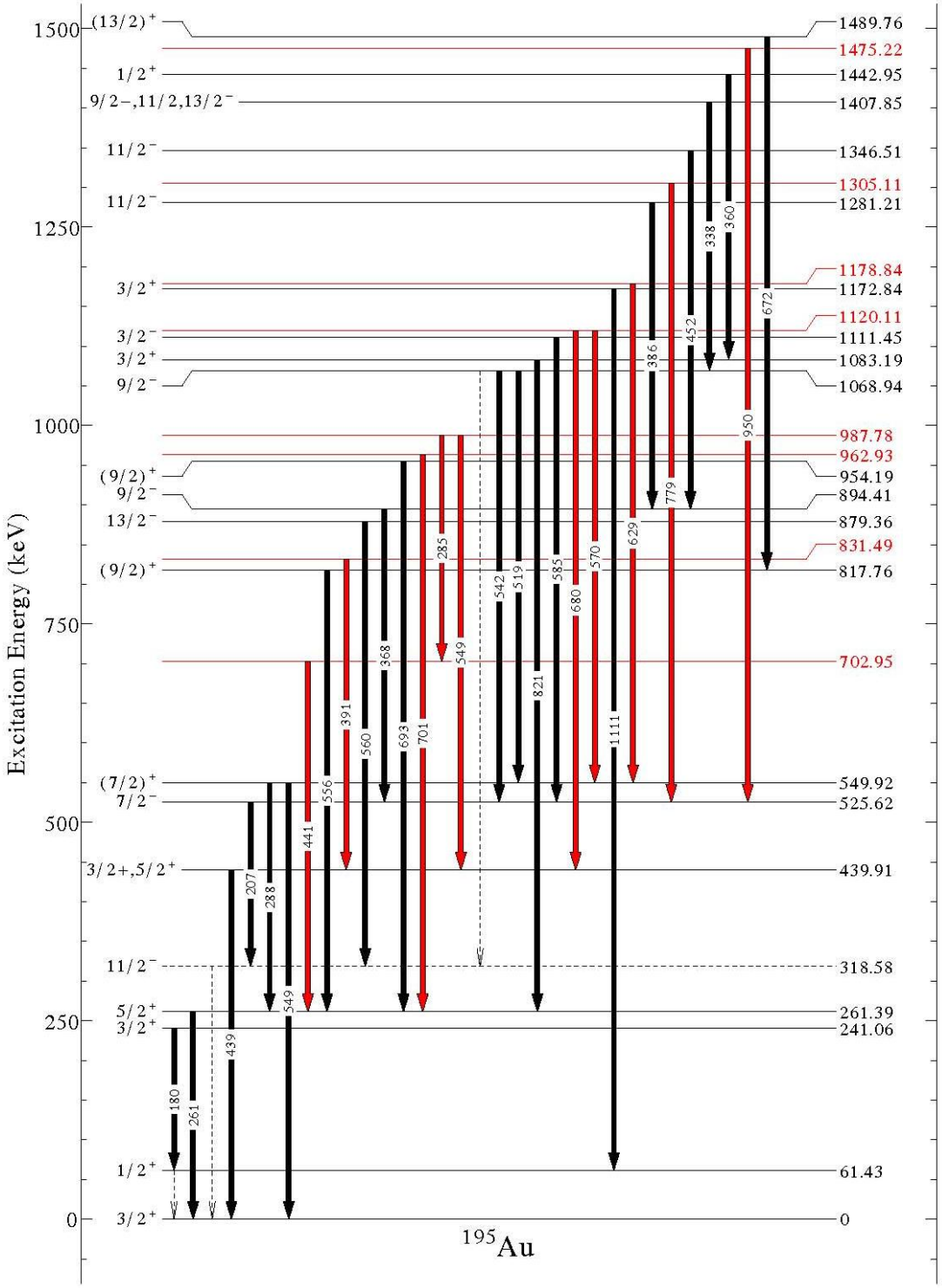

Figure 3.23 The constructed level scheme for ^{195}Au resulting from this work. The transitions and levels in solid black were previously seen by others and by the present study. The dashed lines represent transitions and levels seen in previous work, but we were not able to confirm in our work. Levels and transitions in red are new from this work.

3.4 Theoretical Predictions

As it was discussed in the introduction it is possible to predict the ^{196}Au energy levels only with other members' excitation energies using the Eq. 1.14. There are new energy levels that were measured for ^{195}Au until excitation energy 1.5 MeV. The levels that have positive multi polarity can be used to predict ^{196}Au low-lying levels with the negative polarity.

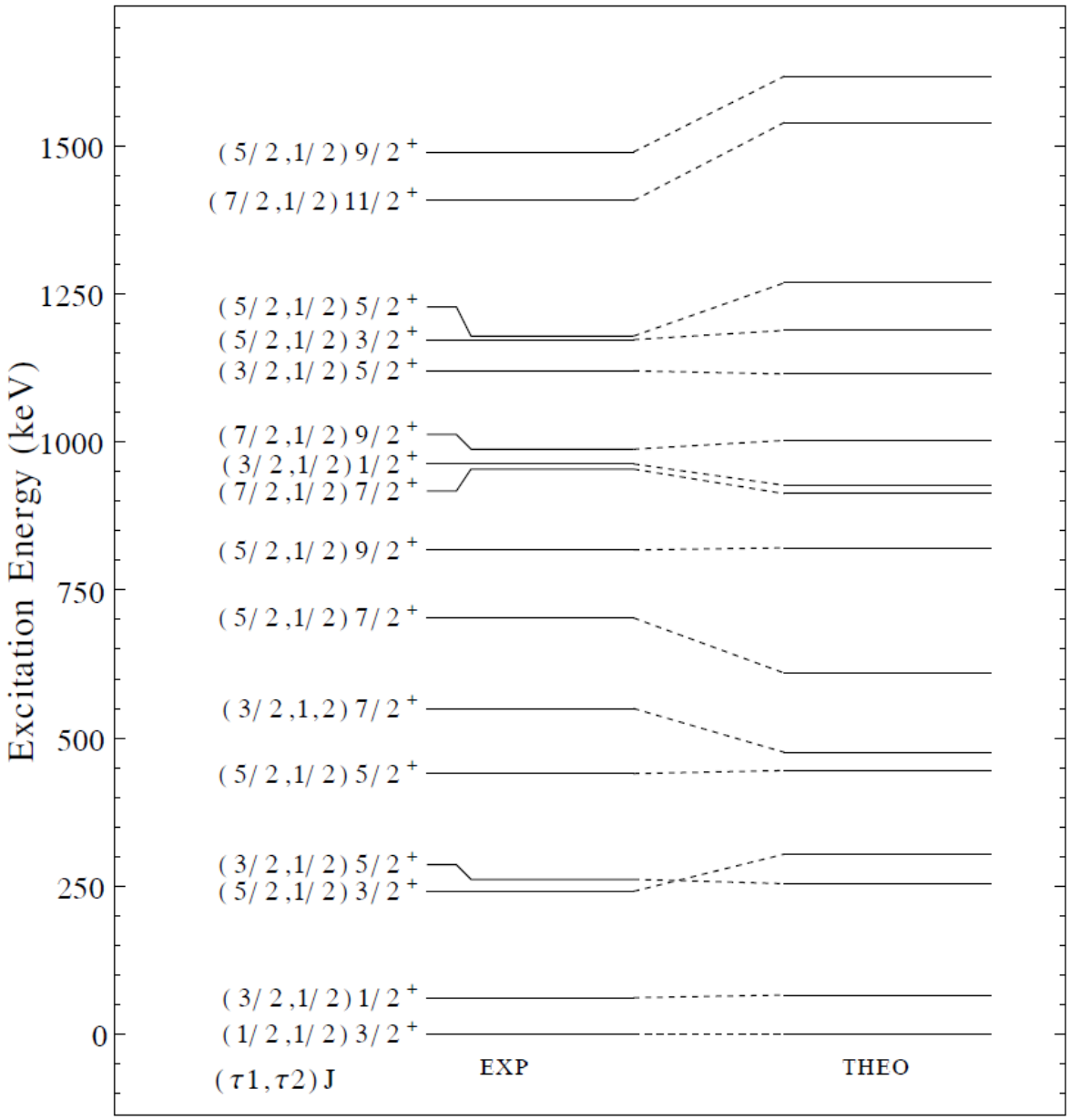

Figure 3.24 Measured and calculated excitation energy levels for ^{195}Au. N_1=6, N_2=0, Σ_1=6, Σ_2=0.

First of all, ^{195}Au levels should be fitted with the Eq. 1.14 to find the parameters. In the previous measurements [9, 10, 11] only 10 energy levels where used for ^{195}Au. There is 16 ^{196}Au excited levels in this calculations. The fitting code was written with C++ software which takes the quantum number and minimize the difference between the calculated and measured energy values. Hamiltonian solution gives eigenvalues of energies with some constant accuracy, the value that will be calculated for the ground state will be the constant. Other energy values will be corrected with that value. The Fig. 3.24 shows the comparison between the measured and calculated excitation energy levels for ^{195}Au. The difference between the calculated and measured values is less than 80 keV until 1250 keV excitation energy. So the theoretical values have very good agreement with the experimental.

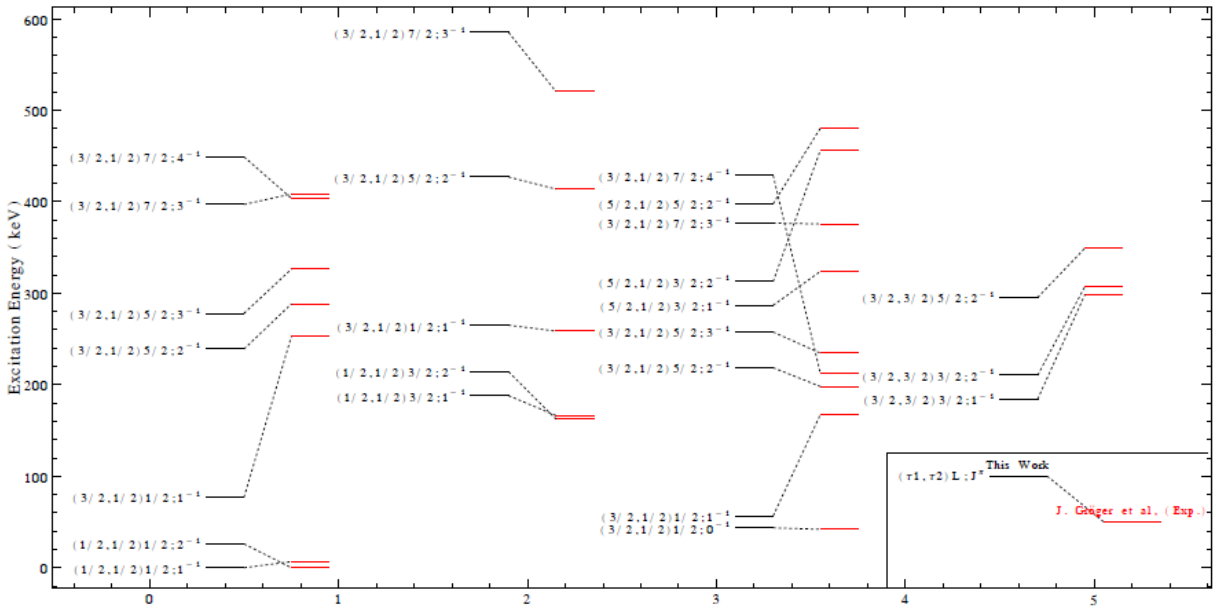

Figure 3.25 Predicted ^{196}Au levels comparison with experimental measurements from [9].

There can be used only one spin value for each excitation energy level. In the calculations all possible candidates were check and were picked up only the ones for which the theoretical calculations is closest to the experimental

measurements. Table 3.5 shows the parameters from this fitting in comparison with other experiments values.

Table 3.5 Formula 1 parameters values.

	A	B	B′	C	D	E
This work	53.5	-3.37	-43.88	27.31	16.11	8.28
Ref. [9]	52.5	8.7	-53.9	48.8	8.8	4.5
Ref. [10]	62.1	-2.6	-52.6	49.7	5.0	6.3
Ref. [11]	52.3	12.4	-58.0	50.1	6.9	4.4

The biggest impact of these new levels have the B′, C, D, E parameters. Then with the use of the following parameters can be predicted levels for ^{196}Au. The Fig. 3.25 shows the comparison of the predicted excitation energy levels and the experimentally measured values from the Ref. [9] until 600 keV energy level.

The maximum difference between the values is the 120 keV. but χ^2 for this measurement and the is less than Ref. [9] χ^2. The explanation of such difference is that during their predictions they use less excitation energies for the ^{195}Au and the spin assignment can be not accurate.

Fig. 3.26 shows the comparison between the all possible excitation energies for ^{195}Au until 1 MeV with the Ref. [9, 10, 11]. All 3 references have very similar excitation energies. In their predictions the band can be separated from each other. In this work prediction the band mix together. Only the mixing energies vary a lot, rest is within the 40 keV difference.

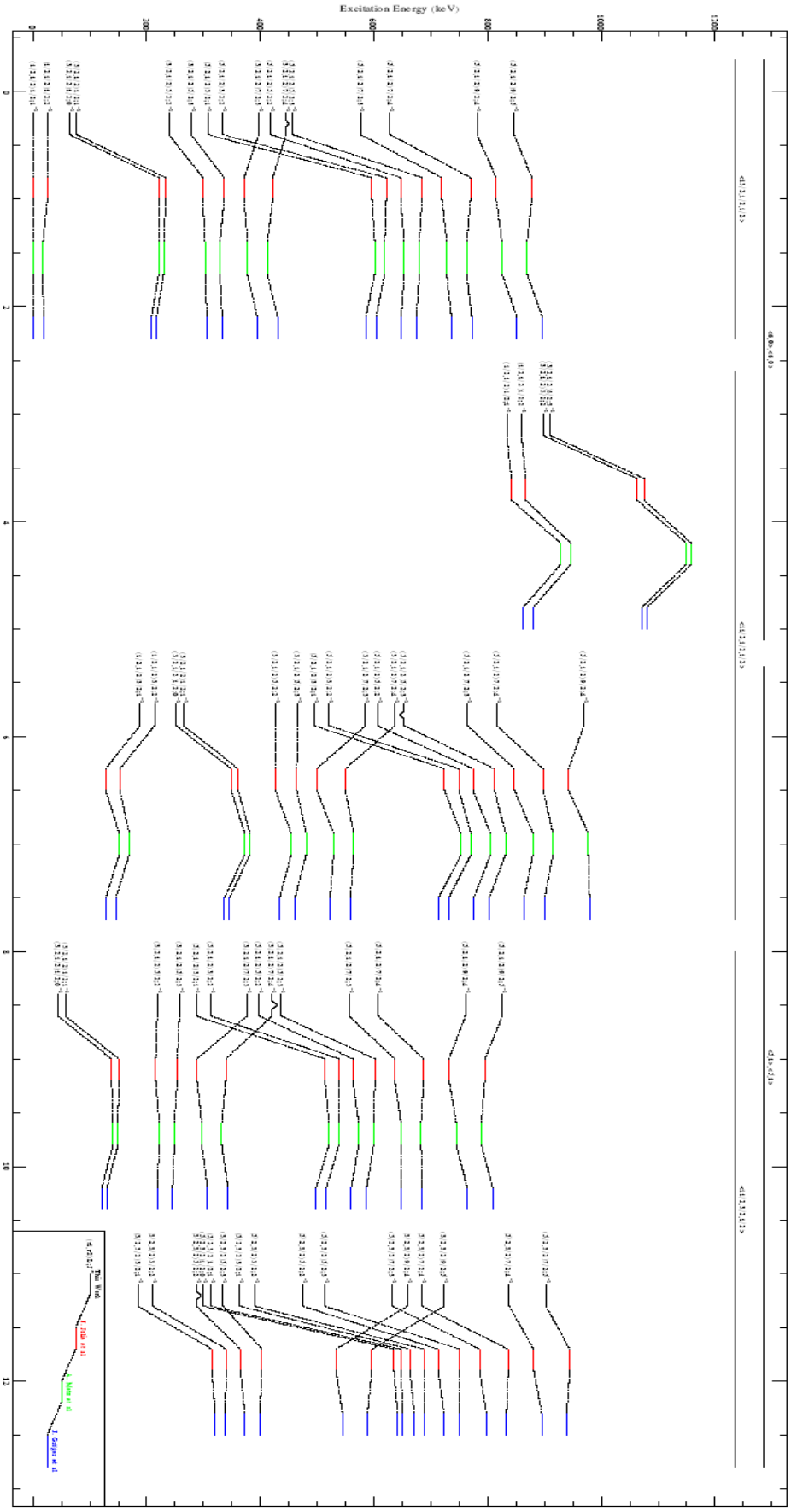

Figure 3.26 ^{196}Au theoretical prediction comparison for this experiments and the Ref. [9, 10, 11] until 1 MeV excitation energy.

Chapter 4

4. $^{13}C(\alpha,n)^{16}O$ Experiment Preparation

The $^{13}C(\alpha,n)^{16}O$ experiment was carried out at the University of Notre Dame Science Laboratory with the 11MV FN Tandem. Four 32 by 32 Double-sided Silicon Strip Detector (DSSD)s were used for charged particle energy and position detection and 12 Deuterated Scintillator Array (DSA) from University of Michigan for neutron detection.

DSSD were located symmetrically to beam direction. The detectors centres were 13 cm and 12 cm away from target with 23.83° and 57.3° angles relative to beam direction respectively.

DSA consisted of 12 detectors 7 of them were 4 inch x 6 inch and 5 of them 2 inch x 2 inch covering total 22°- 146° angular range.

If the beam energy will be enough high (around >29 MeV) than it will be possible to populate ^{16}O excited levels above 4α break-up level. After ^{16}O it can decay with the multiple ways: $^{16}O \rightarrow {}^{8}Be+{}^{8}Be$, $^{16}O \rightarrow {}^{12}C+{}^{4}He$ and $^{16}O \rightarrow 4{}^{4}Be$. This chapter will present detailed information how everything was tested, calibrated and prepared for this experiment.

4.1 Previous Measurements

A lot of studies were done to explain cluster structure of ^{16}O. One of the first studies was done P. Chevallier et al (Ref. [29]). During the experiment the detector was fixed at 90° center of mass angle and beam energy was varied from 11.85 MeV to 19.4 MeV. It means only certain excited level ^{16}O will get to the detector.

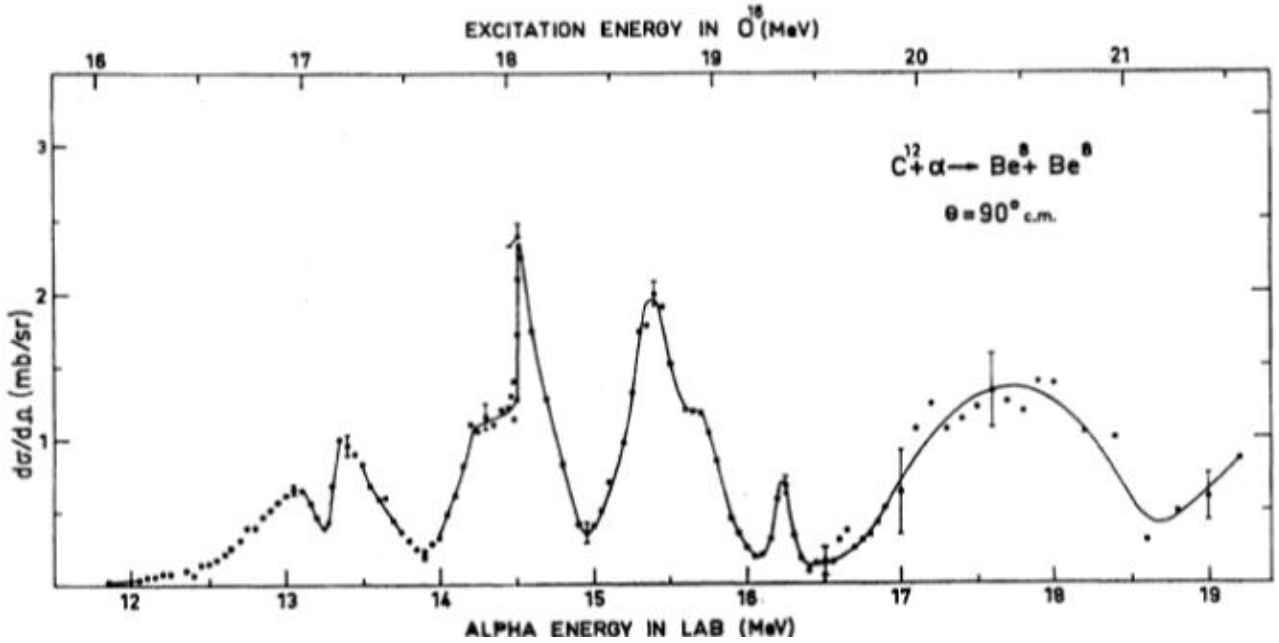

Figure 4.1 Cross section dependence from excitation energy in ^{16}O with the $^{12}C + \alpha = {}^{8}Be + {}^{8}Be$ reaction, when the detectors were at 90° center of mass angle.

Cross section was measured for ^{16}O excited levels. The constructed cross section dependence from ^{16}O excited level energy will show the excited states of ^{16}O.

Table 4.1 Identified excited levels of ^{16}O.

E^{α} (MeV)	$E^{*}(16O)$ (MeV)	J^{π}
13.05	16.95	2^{+}
13.35	17.15	2^{+}
14.1	17.7	$0^{+}.2^{+}$
14.2	17.8	4^{+}
14.52	18.05	4^{+}
15.2	18.6	$0^{+},2^{+}$
15.6	18.9	4^{+}
16.25	19.35	6^{+}

Measured excitation function shows that there are some excited levels until the excitation energy reaches 20 MeV. There is a big bump above 20 MeV, but probably there are some levels under that bump. The Fig. 4.1 presents the excitation function.

The difference between the prepared experiment and Ref. [29] experiment is different reactions to populate excited states of ^{16}O. In the previous experiment $^{12}C + \alpha = {}^{8}Be + {}^{8}Be$ reaction was used. It is the result of or $^{12}C + \alpha = {}^{16}O + \gamma$ reaction. In the current experiment ^{13}C will be used as a target so the reaction will be or $^{13}C + \alpha = {}^{16}O + n$. This reaction will have additional freedom and will easier to populate 160 excited levels.

On the other hand, there will additional neutron which can be used to do gates and make background lower.

The result was that they find out that the ^{16}O in some excited states has few times bigger momentum of inertia. That is the result of linear α-chain structure.

As it was mention in the introduction ^{16}O is not unique nucleus that has cluster states. Most of them are on the stability valley. Good explanation of the cluster states was done by Ikeda. Fig. 4.2 shows the structure of all α-conjugate nuclei which begin to form clusters at different energies. All energies in the figure are in MeV. So for example Silicon is one of that nuclei. It begin to form α-particle in the nuclei when the excited energy is 9.78 MeV. Than it begin to form more and more clusters and finally it become clustered completely when excited energy reaches 38.46 MeV.

This kind of nuclei have very interesting skill as well they can be clustered not as α-particle, but also other α-conjugate nuclei. For example Magnesium at excited level 13.93 MeV consist of two ^{12}C nuclei.

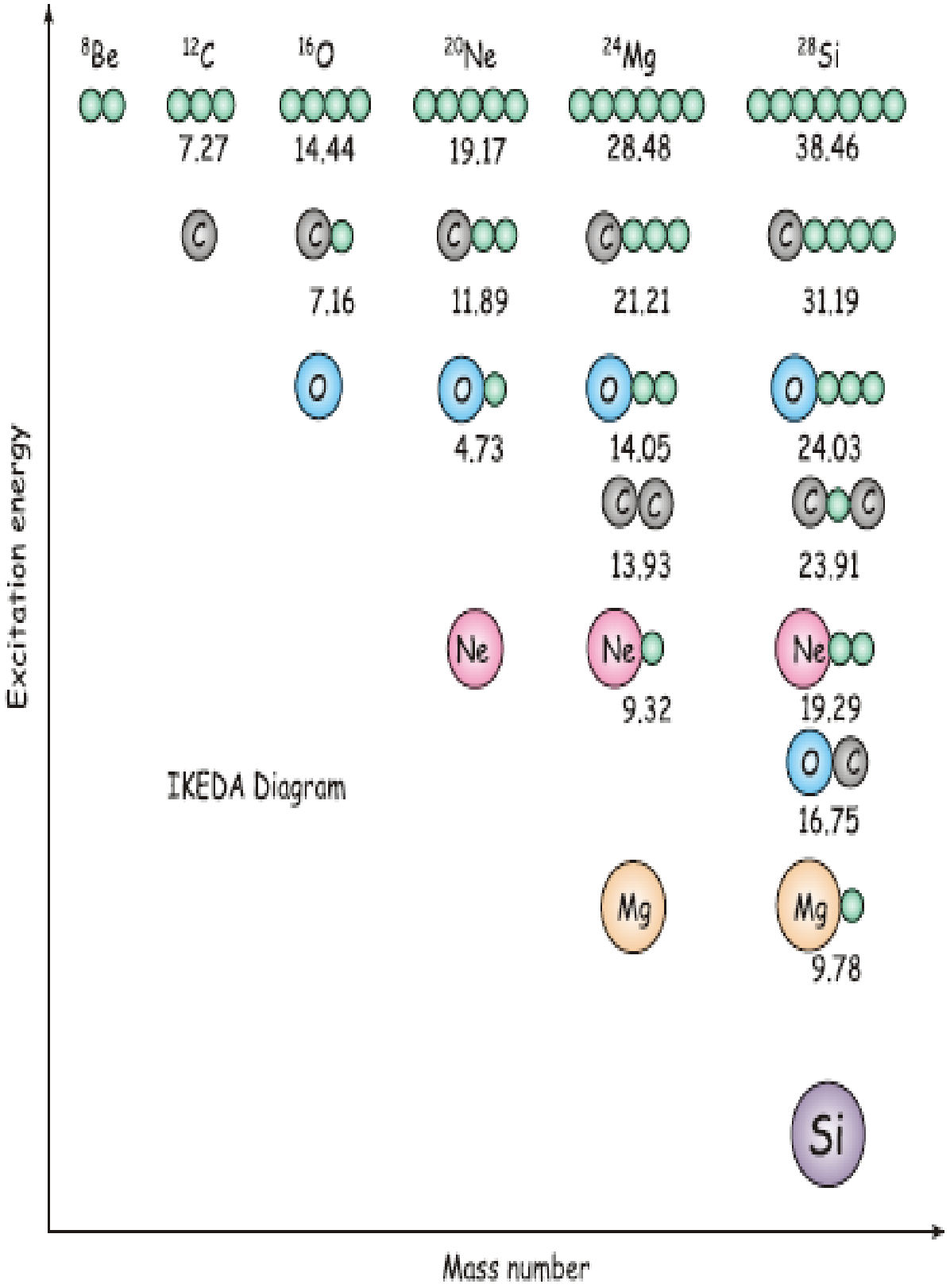

Figure 4.2 Shows the Ikeda diagram which describes structure of α-conjugated nuclei. All energies are in MeV.

4.2 Electronics

There was 256 channels from DSSD's during the experiment. Fast DAQ was required to control the data ow due to Application Specific Integration Circuit (ASIC) was used. ASIC is high-density signal processing in the low and intermediate-energy nuclear physics. It is mainly used for silicon detectors. It has 512 channels per box and 16 channels per chip.

Single DSSD is shown in the Fig. 4.3. It can be seen how strips are organized and connected with wires. The key thing is that the channel number and strip number does not much with each other. It is important as two kind of noise can be created during experimental runs.

One of them is cross talk. Which I will discuss later in this chapter and second one is the noise that can be created if the electric wires will be too close to each other.

Not matching strip numbers and channel numbers allow to differ them which will help in better understating of the structure of signal from the detectors and do proper corrections.

Each strip is 2 mm width and 500 micrometer thickness. It is enough to detect charged ions with the energy around 20 MeV. Which is more than enough for this experiment.

It has internal PreAmplifier (PA) which has 40 keV energy resolution at output, but it is possible to connect external PA as well and the energy resolution will be better (< 30 keV). It has 1 ns - 1.5 ns timing resolution for built in pseudo Constant Fraction Discriminator (CFD).

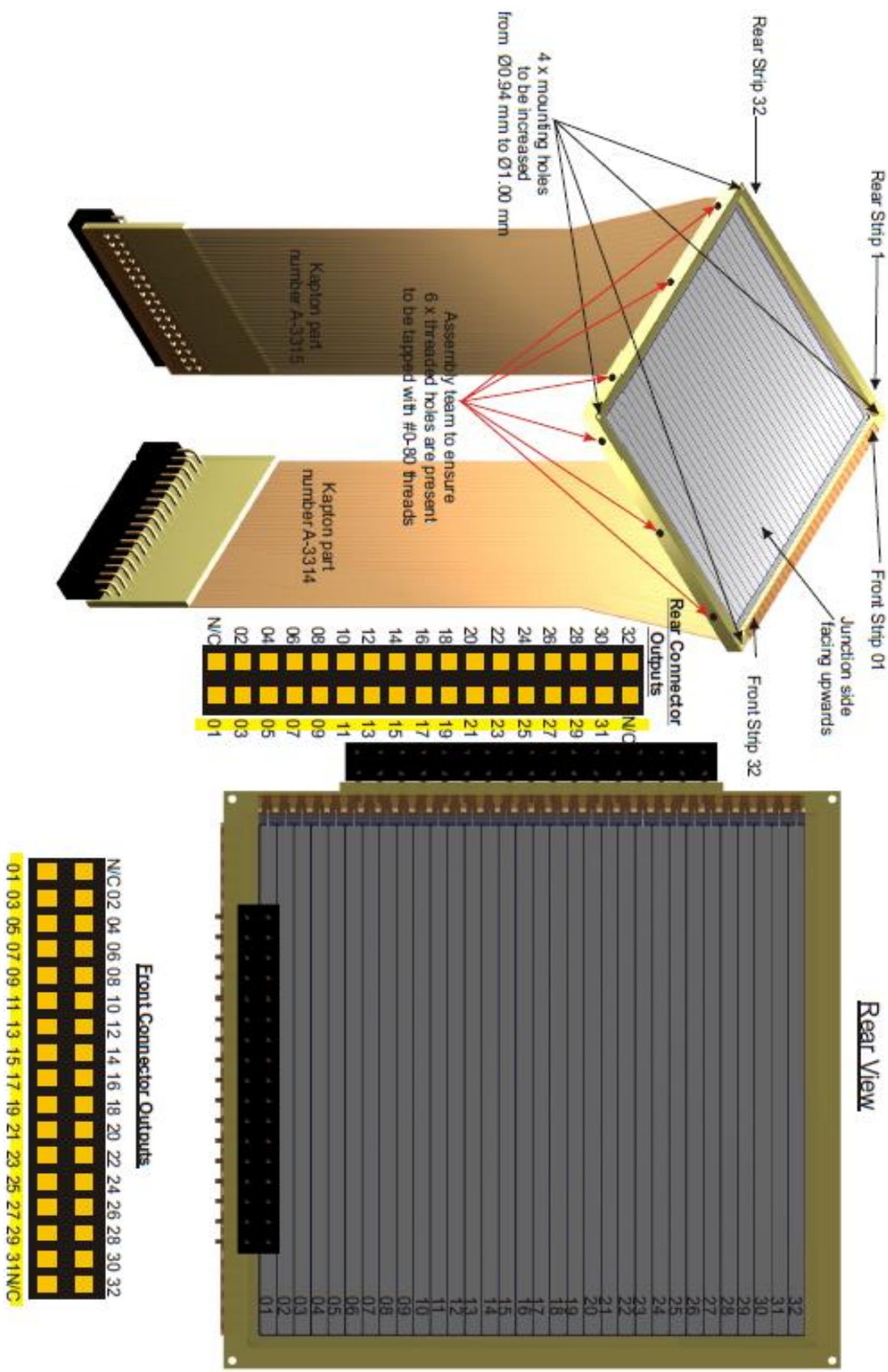

Figure 4.3 Presents the Double-sided strip silicon detector structure and how the strip are connected with the connectors.

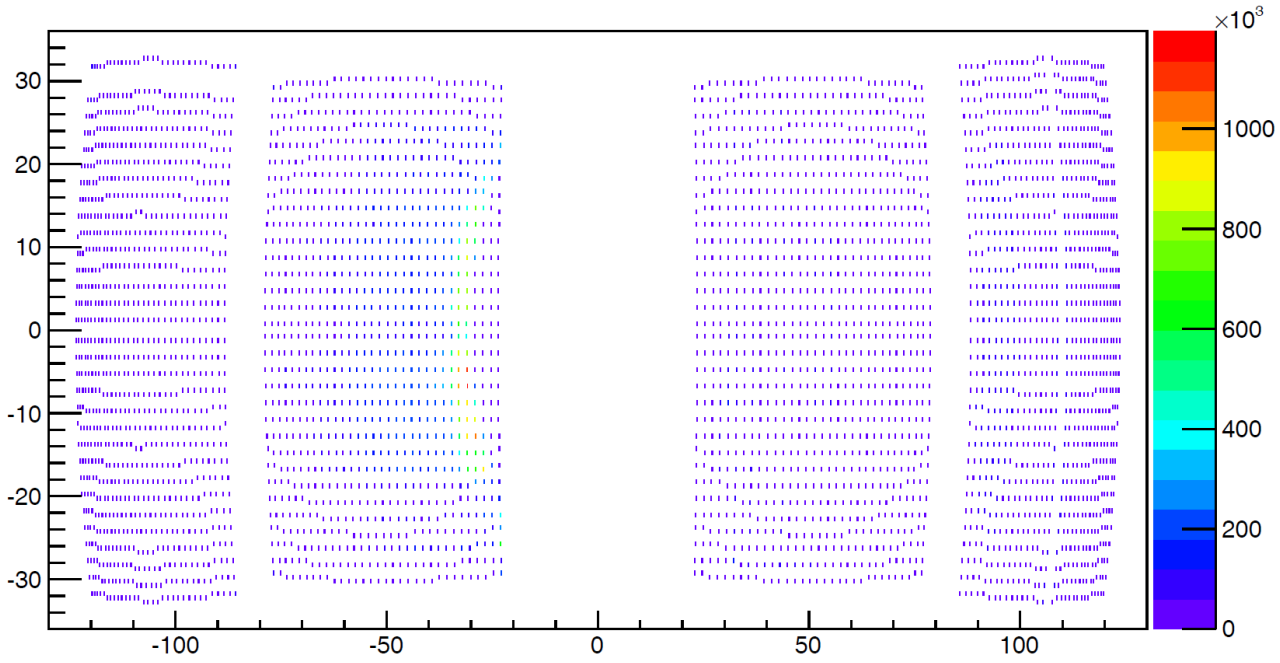

Figure 4.4 Shows the hit pattern in the Double-sided Silicon Strip Detector (DSSD)s from the target position.

The hit pattern of the DSSDs is shown in the Fig. 4.4. From the pattern is easy to see that the distribution is mostly isotropic.

MQDC-32 module was used to read out data from neutron detectors. Both ADCs work simultaneously so it is possible to do gates and reduce background.

As the neutron data was analyzed by other group. I can just bring the raw spectrum how it looks like. Fig. 4.5 shows the raw spectrum. There is two diagonal distributions one of them is neutrons with low intensity and second one is the γ-s with the high intensity.

It is possible to do gates to the measured excited levels and get neutron data. With that data will be possible to confirm the energies of the ^{16}O. This data will be analyzed in the University of Michigan by Michael Febbraro.

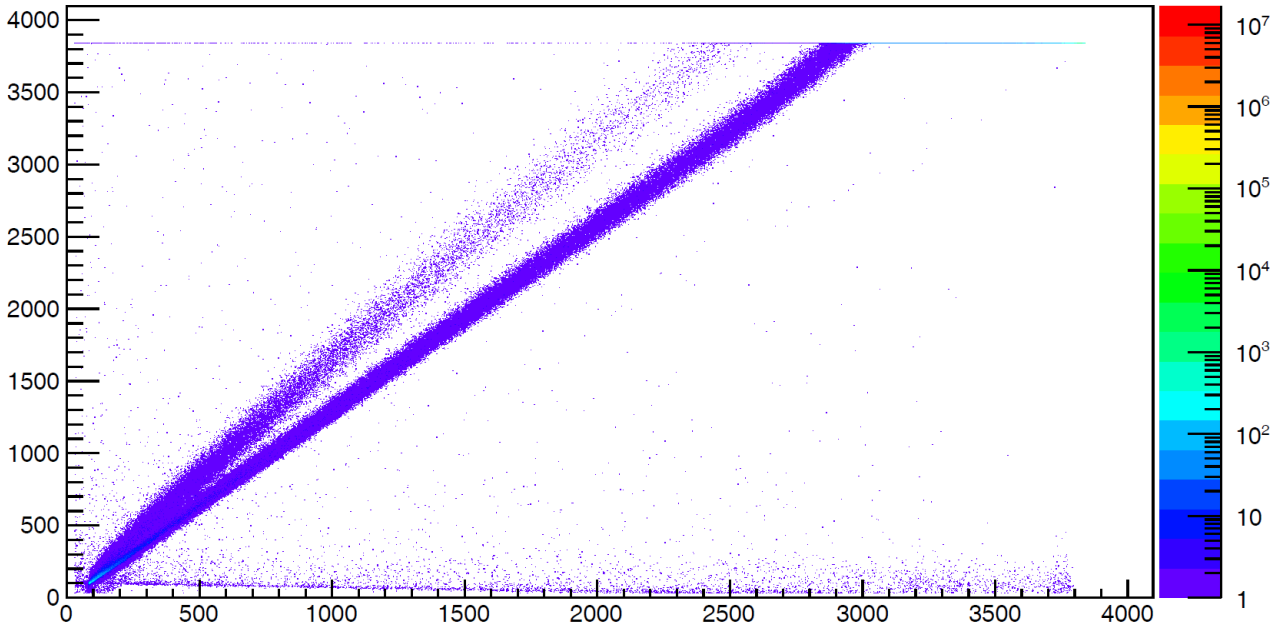

Figure 4.5 Raw spectrum from the neutron detector.

4.3 Calibration

Detector calibration is one of the most important parts of experimental data analysis. It will be possible to do energy and timing gates to measure energy of interest precisely with energy and timing calibration. Following section will describe energy and time calibration for Double-sided Silicon Strip Detector (DSSD), that were used for $^{13}C(\alpha,n)$ reaction study experiment. Also timing calibration for neutron detectors from Caen TDC. Both α-source and pulsar was used to do calibration.

4.3.1 Energy Calibration

Using both a pulsar and an α-source enabled finding the best calibration function over a larger energy range. Pulsar was used to apply different voltages to each channel. An α-source was used to convert voltage into energy. Applied voltages are listed in table 4.1.

Table 4.2 Voltages that were applied for calibration.

Voltage (V)						
0.02,	0.04,	0.06,	0.08,	0.1		
0.12,	0.2,	0.3,	0.5,	0.7,	1.0	
1.2,	1.3,	1.4,	1.5,	2.0,	2.5,	3.0

With following voltages approximately from 800 - 14500 channel range was covered or energy range from 250 keV - 20000 keV. There is also electronics threshold that was measured and got around 900 channels or 300 keV energy. That is why for most of the channels 0.02 V peak was not able to measure.

$$\text{Voltage} = \text{Slope} * \text{Centroid} + \text{Offset} \tag{4.1}$$

$$\text{Voltage} = A * \text{Centroid}^2 + B * \text{Centroid} + C \tag{4.2}$$

Few functions were tested to find best calibration function. First of all was tested linear fit (4.1) in all range, than second order polynomial fit (4.2) and third way was divide all range into two (low and high) ranges and do linear fit for each part. Comparison between three methods is shown in Figure 4.6. The lowest dispersion is when all range was divided into two parts as was mentioned in the third case.

Whole range where divided into two parts from middle point (1.5V). Middle point was included in both low and high energy calibration functions fitting to connect calibration functions in that point. Figure 4.7 shows dispersion for 16 channels. With this method the dispersion for most channels is below 0.001 V. In energy equivalent it will be 6-7 keV. After getting the well-defined shape of calibration functions it is important to convert voltage into

energy. To do that α-source was used. α-source emits two alphas with 3182.8keV and 5476.0 keV energies. With those energies centroids can be measured and find corresponding voltages. Assumption that energy has a linear dependence from voltage was done so calibration functions can be rescaled and get energy dependence from centroid.

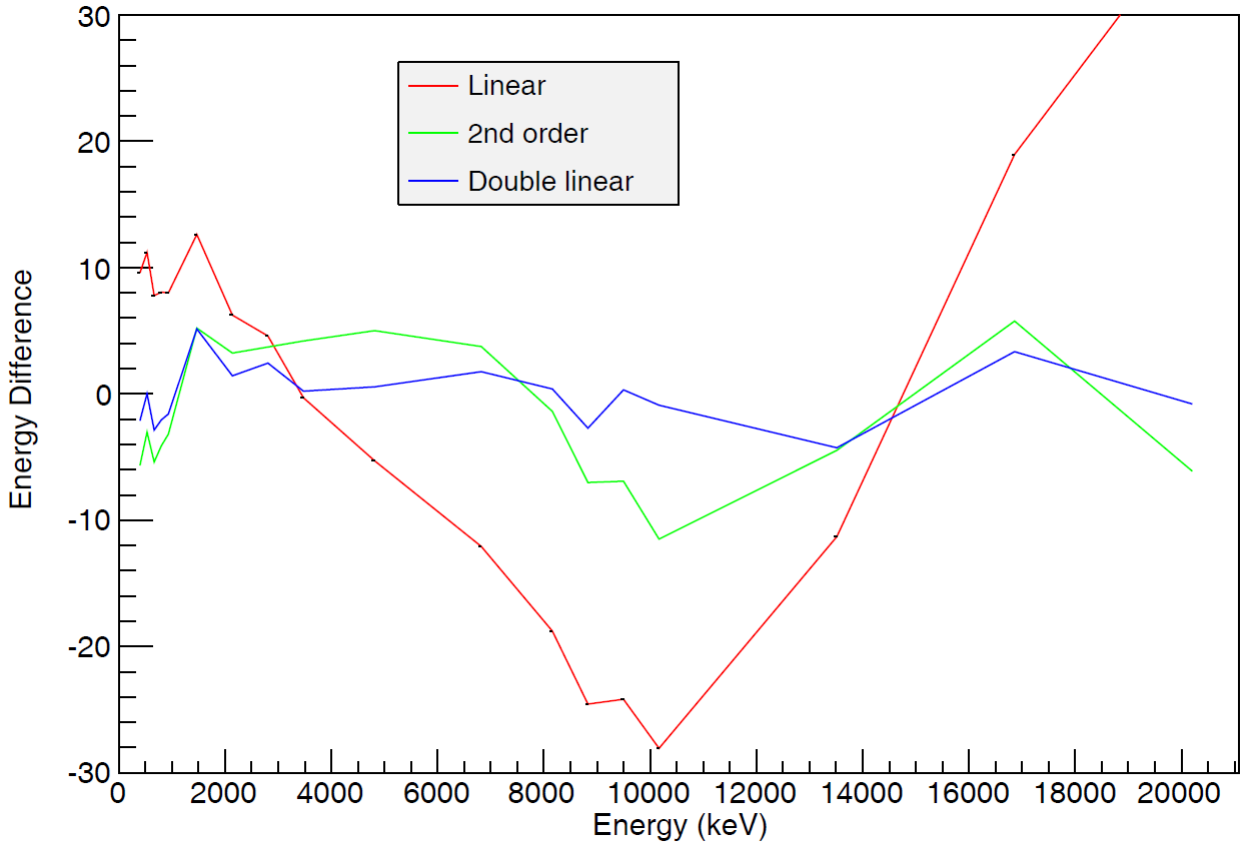

Figure 4.6 Voltage dispersion (applied voltage minus calculated voltage) dependence from applied voltage for three different cases in same channel.

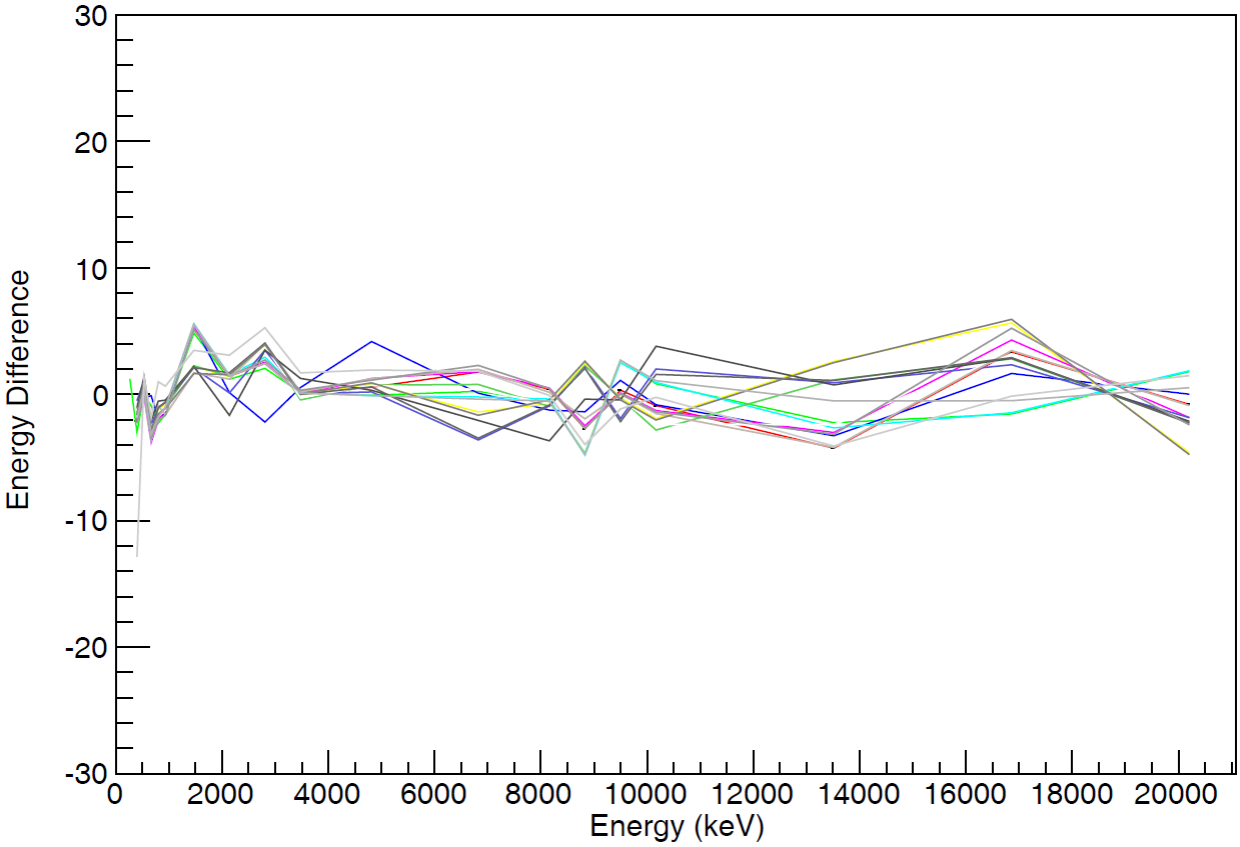

Figure 4.7 Voltage dispersion (applied voltage minus calculated voltage) dependence from applied voltage with double linear calibration method calculation for different channels.

4.3.2 Crosstalk Corrections and Hit Reconstruction

Beside energy calibration, it is also important to subtract noise that signal generates. When the signal has large voltage it can electromagnetically couple with nearby strips. It can cause that the nearby will generate signal simultaneously. This kind of noise called crosstalk. Crosstalk corrections will reduce all those kind of signals. In this case, it is also important to remember that strips at the edge of detectors will have smaller crosstalk, because they have only one neighbouring strip. Voltage was applied to each strip to check nearby strips and find the crosstalk. There will be linear dependence between applied and crosstalk energies as shown in Eq. 4.3.

$$Energy_{crosstalk} = Slope * Energy_{applied} + Offset \quad (4.3)$$

Figure 4.8 shows example of applied voltages in strip 11. There are three peaks which correspond to 2.0 V, 2.5 V, 3.0 V. Figure 4.9 shows nearby strips 10 and 12 spectra. Top figures are raw spectra with three crosstalk peaks in the channel range 1000-1500. It is very close to our threshold (approximately 900 channel number). Both applied voltages and crosstalk peaks have same statistics. After fitting crosstalk peaks and getting centroids with the energy calibration was it possible to convert them into energy. With both applied voltage energy and crosstalk energy linear fitting was done to get the line slope and offset. Figure 4.9 button spectra are gated spectra on strip 11 2.5 V peak. Gating can be used if three peaks overlap each other.

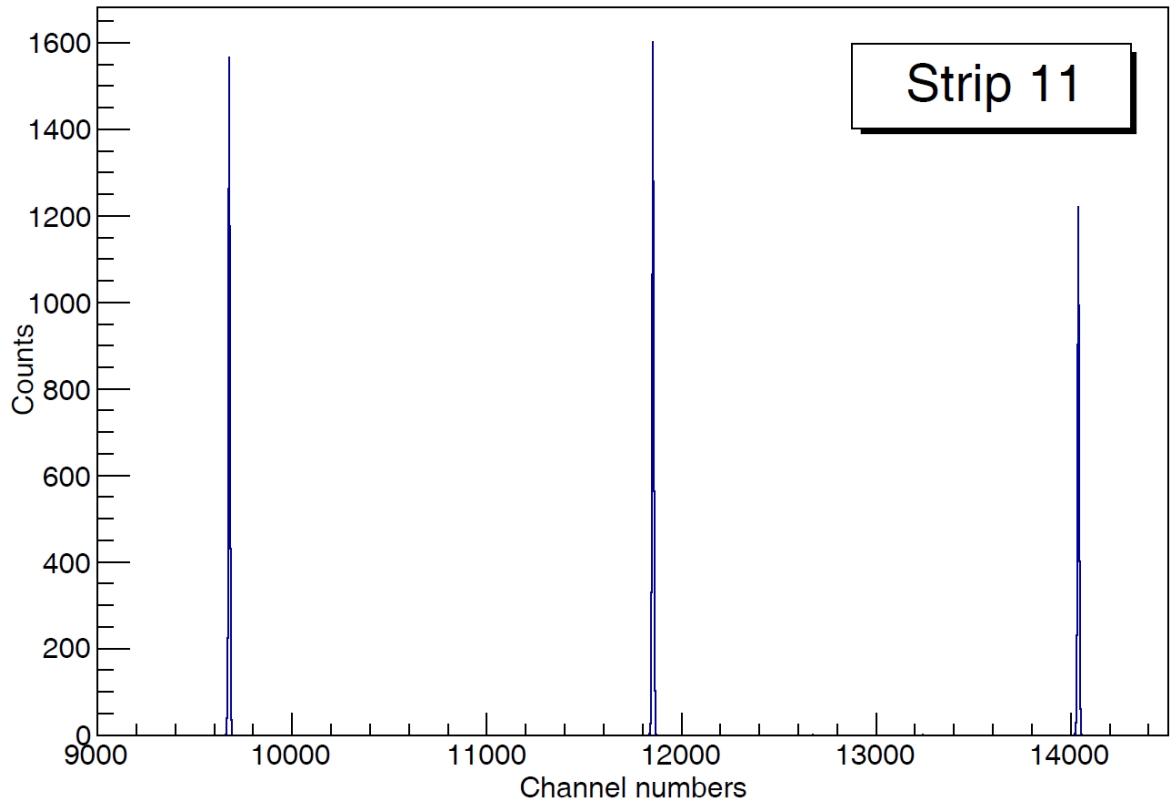

Figure 4.8 Strip 11 spectrum with 2.0 V, 2.5 V, 3.0 V peaks.

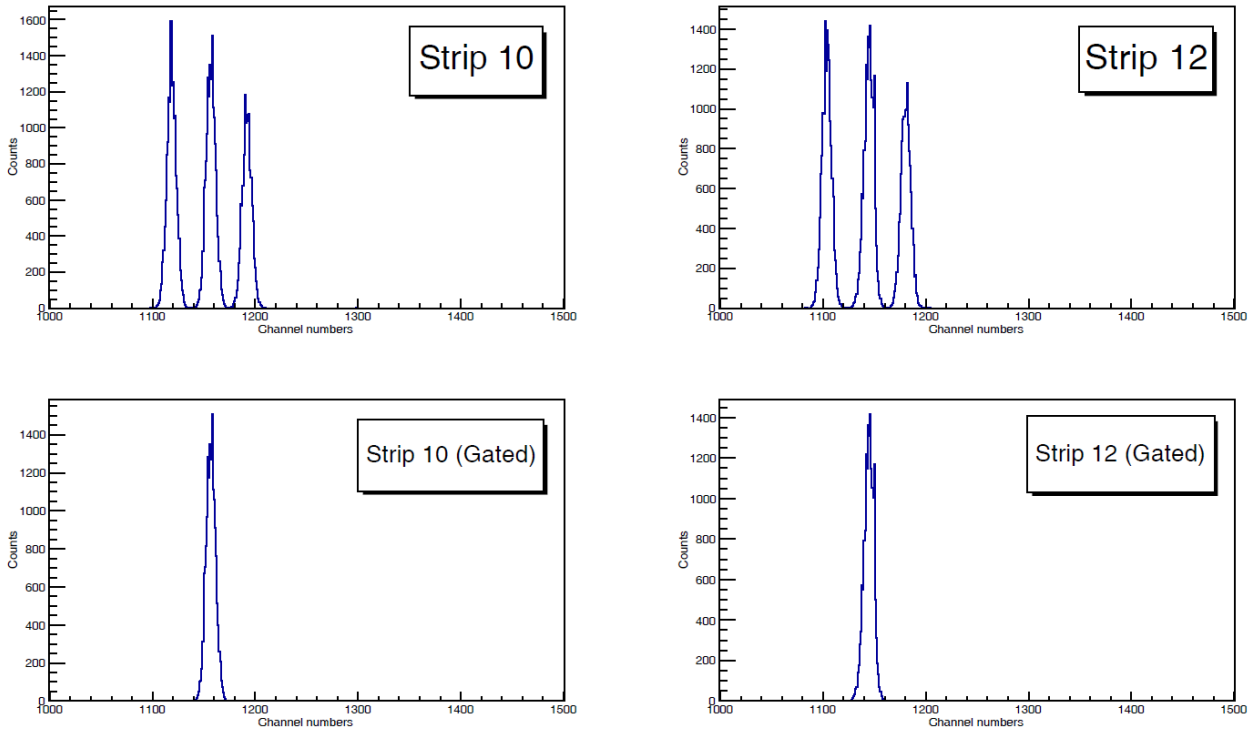

Figure 4.9 Crosstalk spectra in strip 10 (top-left figure) and strip 12 (top-right figure). Button figures shows crosstalk spectra after gating on 2.5V peak in strip 11. Strip 10 gated spectrum is button-left figure and strip 12 gated spectrum is button-right figure.

After calculating crosstalk measured energy and calculated crosstalk energy subtraction was done. If the subtraction will be below the threshold for certain channel than the signal is crosstalk.

The crosstalk corrections were implemented into the main script which will be used as the data analyzing main code. The code will be run with the ROOT software and produce all important spectra for this experiment.

The crosstalk correction checking was done, to be sure that it works correct. Without the crosstalk correction during the single event crosstalk noise will create additional signals and if all signals numbers will be drawn in the histogram it will have the shape as in the Fig. 4.10 red line. With implementing the crosstalk corrections into the code the number of the signals

will be reduced, but also will be reduced the null as well due to the signal splitting correction. With the corrections histogram has Fig. 4.10 blue line shape.

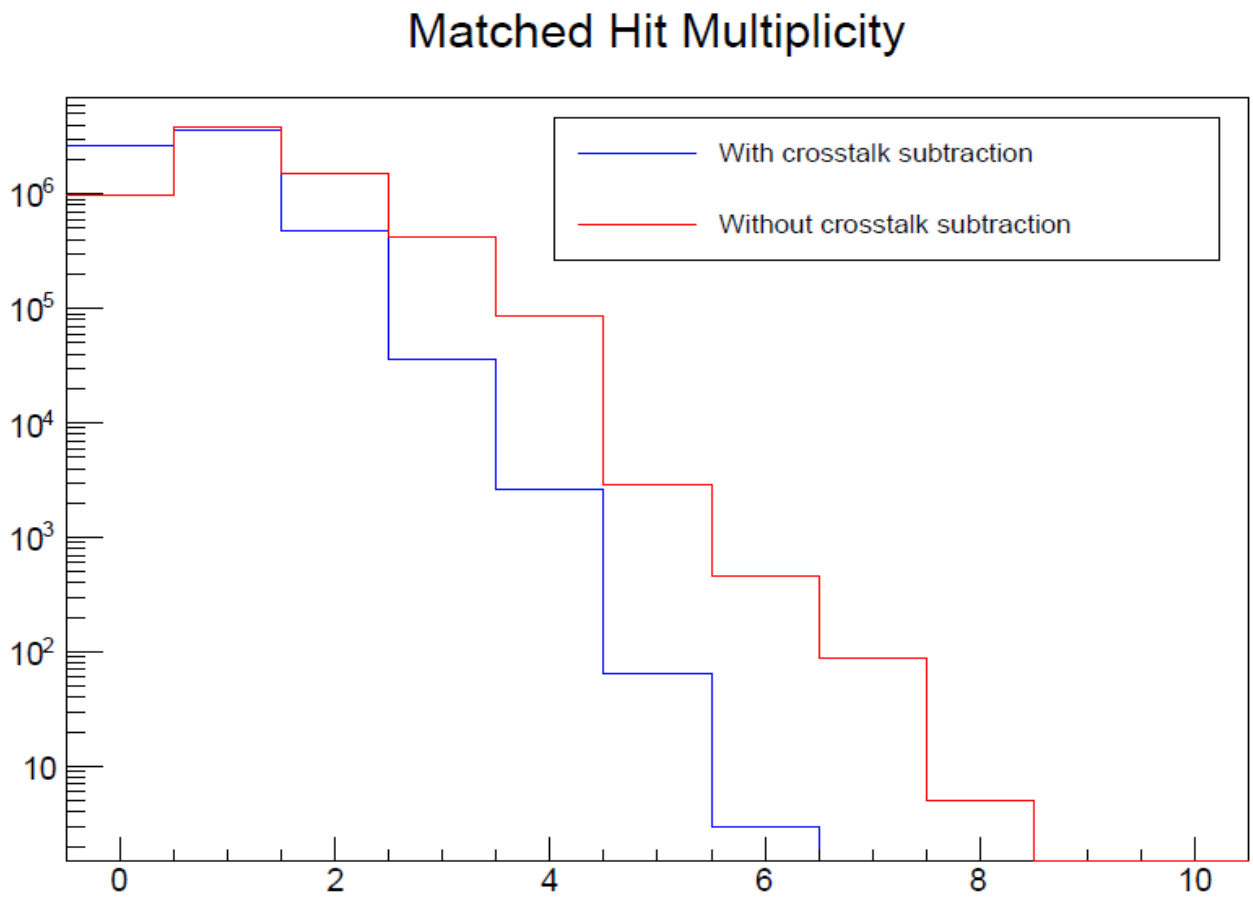

Figure 4.10 The hitpatern that the main script repoduce for the number of the signal from all detectors. Red is without the crosstal correction blue is with crosstalk correction.

In some cases it can be that two signals where trigger simultaneously in nearby strips. Due to that, both signals will create crosstalk on each other. The crosstalk will increase real values of signals. Doing crosstalk subtraction exact energy value will be measured for particle that created the signal.

4.3.3 Timing Calibration

It is important to have timing information to get better idea about data. Timing allows to do time of flight calculations and determine the particle. Due to timing calibration was done for both Caen TDC v775 modules and ASIC chipboard.

Caen TDC v775 was used to get timing information from neutron detectors. With the timing information neutrons and -rays can be separated from each other much better. The fixed voltage and delay time was changed with 40 ns increment in 1.16μs timing range. The time dependence of channel number shown in the Figure 4.11. The time starts from zero from this module and in the fitted parameters the calibration line offset is very close to zero.

Only three 300 ns, 350 ns and 400 ns delay times where used for ASIC timing calibration. Figure 4.12 shows calibration line fitting for ASIC single channel. This module timing start is not zero. It has initial point and goes down when you add delay time. That is why our slope is negative.

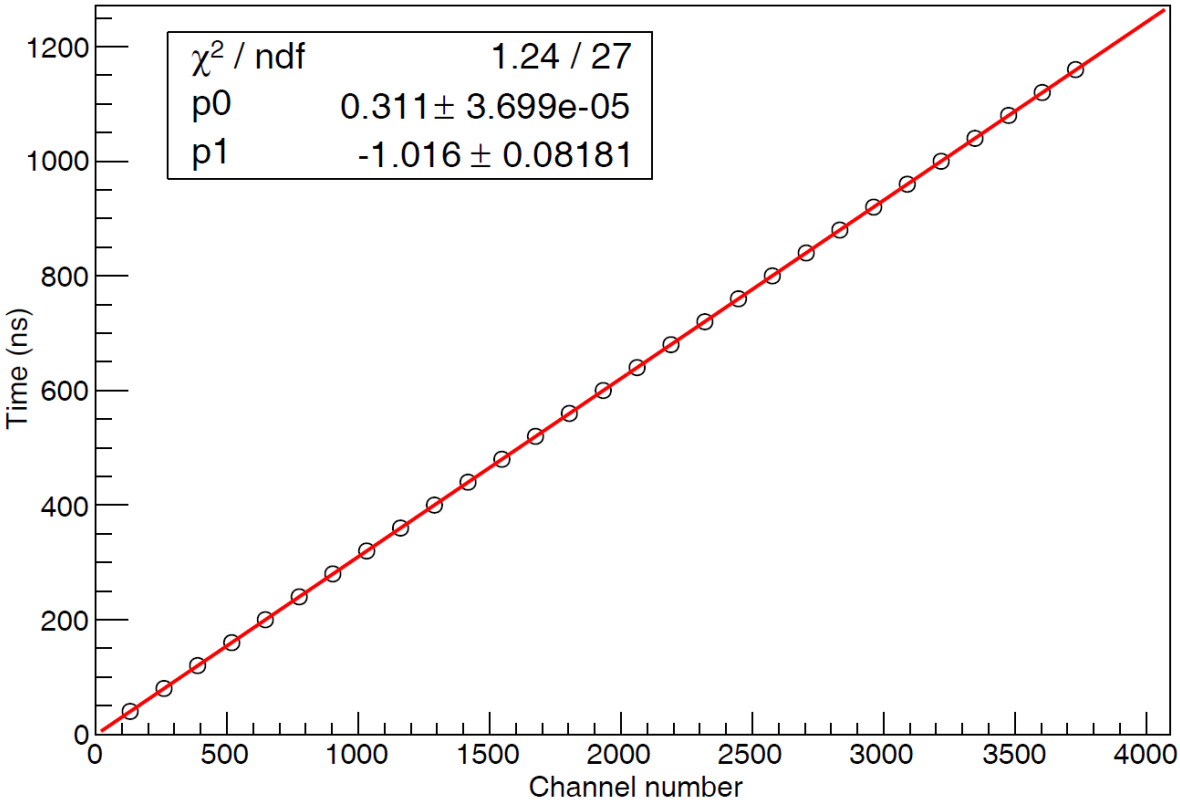

Figure 4.11 Caen TDC timing calibration for single channel. p0 is slope, p1 is offset of calibration line.

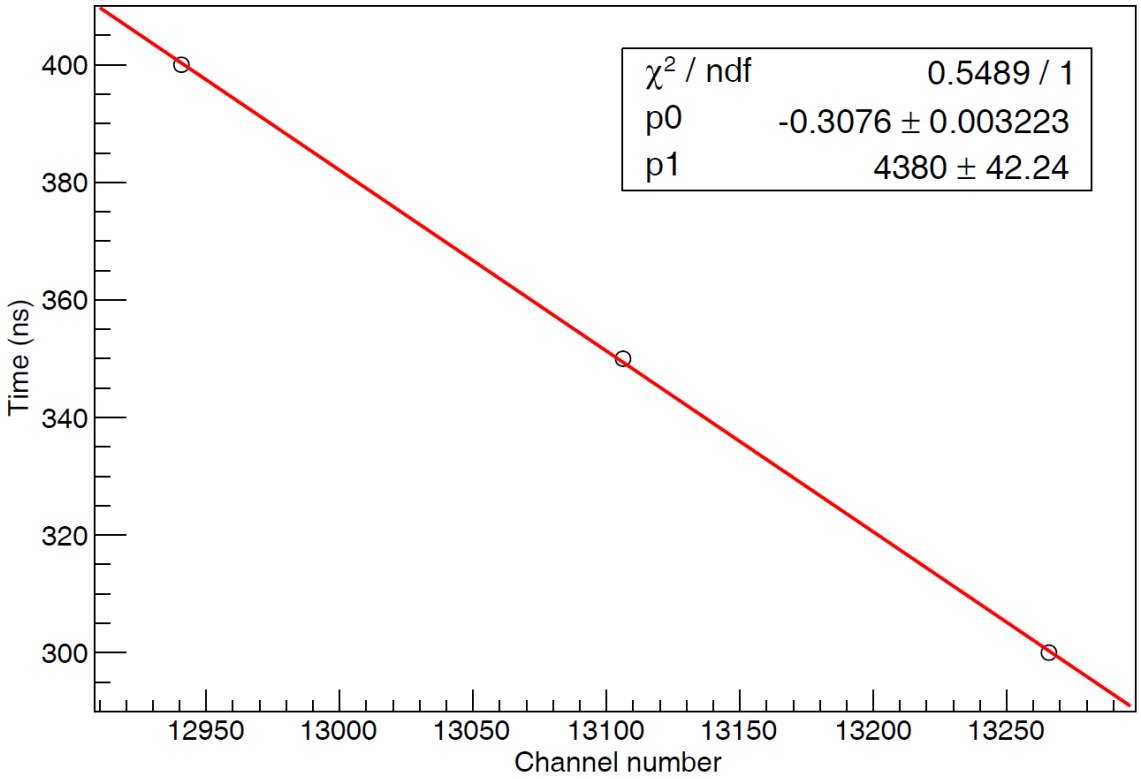

Figure 4.12 ASIC timing calibration for single channel. p0 is slope, p1 is offset of calibration line.

Calibration lines very well match with calibration data. Using those calibrations it will be possible to discriminate prompt and secondary particles, either discriminates by mass. That will be useful in data analysis when reconstruction of different ions will be done.

4.4 Simulations

The simulations play key part during the experimental data analysis. Simulations will improve angular momentum prediction and allow to predict background.

Geant4 package was used to simulate $^{16}O \rightarrow {}^{8}Be+{}^{8}Be$ decay. The main components in the Geant4 are “DetectorConstruction”, “PhysicsList” and “PrimaryGeneratorAction”.

In the “DetectorConstruction” detectors position and materials should be describe. Exact same construction was used that was during experiment. “PhysicsList” describe physical processes that should be used. In this case the “Shillding.hh” [45] already exiting physics list. The physics list includes best-guess selection of electromagnetic and hadronic physics processes.

As for “PrimaryGeneratorAction”, it is necessary to define particles which should be emitted. The reaction of interest is $^{16}O \rightarrow {}^{8}Be+{}^{8}Be$, so it is possible to generate random direction for the ^{16}O and then calculate ^{8}Be direction and emit two ^{8}Be. As ^{8}Be are radioactive, Geant4 will take care of the decay into two α-particles. After all, will be picked up only the scattering angles of ^{16}O for which all four α-particles were detected in the detectors.

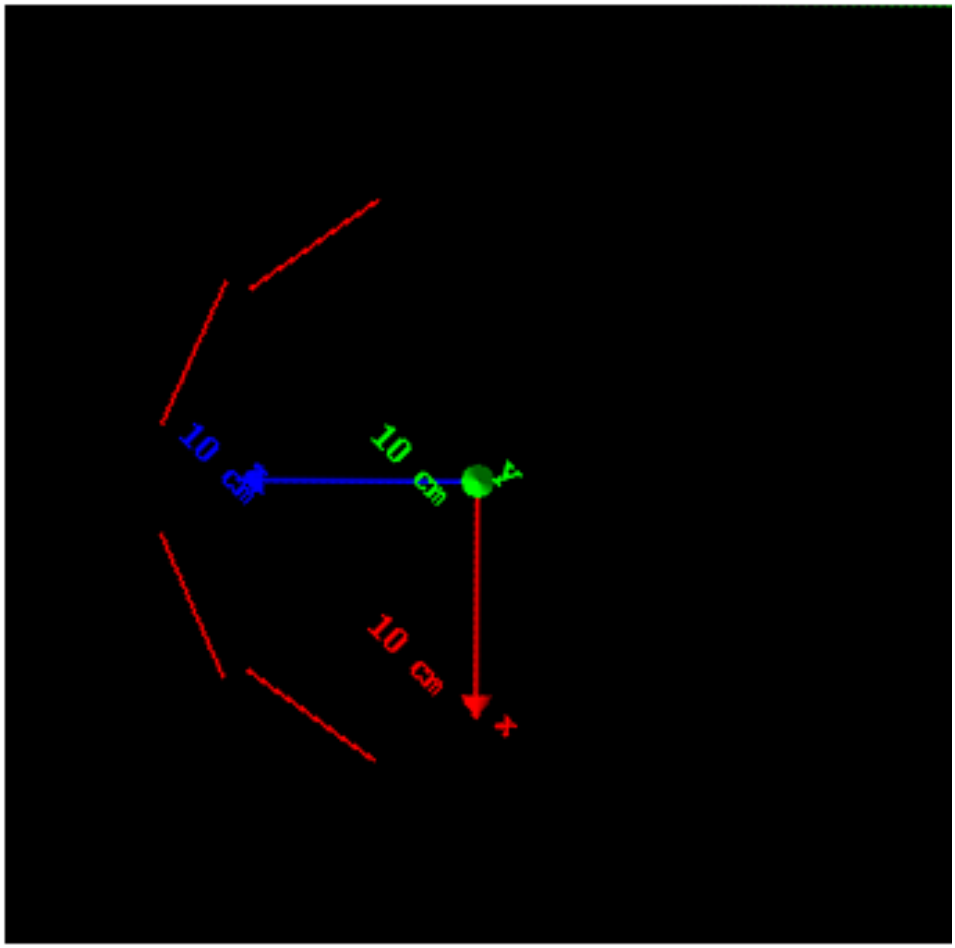

Figure 4.13 Geant4 drawing of the experimental setup. Red lines are detectors. Target is In the center of the picture were three-dimensional axes are drawn.

All for DSSDs are shown in the Fig. 3.13. The actual detector positions were used during simulations target is in the center of the figure were the axis are drawn. As it is drawn from the top the detectors are presented as a lines. In the geant4 detector structure I did not make strips. I made as a small pixels with 2 mm by 2 mm size which is a width of the strip. So if in the code if particle will reach to the pixel the code will keep the energy lose, detector ID, pixel vertical and horizontal numbers and make as an event.

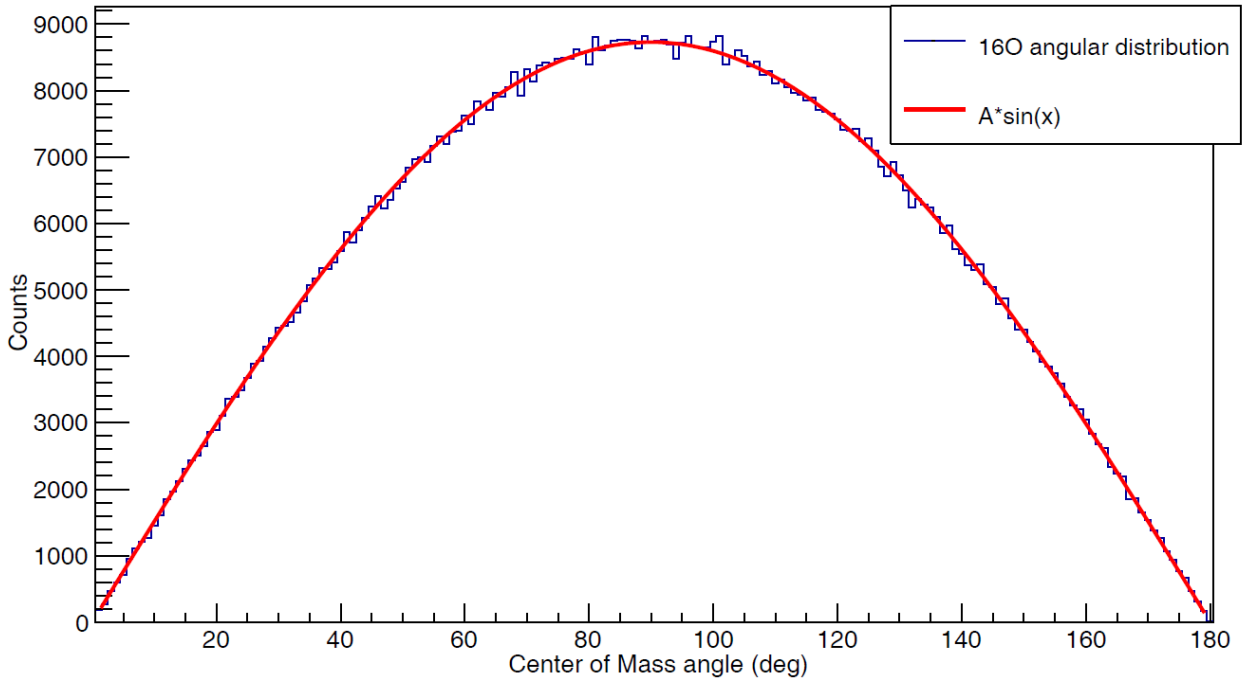

Figure 4.14 Isotopically angular distribution of ^{16}O comparison with A*sin(x) function. Where A constant and equal value of distribution when x=90^0.

^{16}O and neutron will have opposite directions in the center of mass frame as it is two-body reaction. The angle between the ^{16}O and beam directions is center of mass θ angle. After randomizing ^{16}O direction the angle also will be random.

The energy approximation was done and non-relativistic case was used due to nuclei low energies. Energy and momentum of ^{16}O was calculated with the energy and momentum conservation laws after randomizing the angle. The angular distribution should be sine function, due to solid angle dependence from center of mass frame θ angle (Eq. 4.4).

$$d\Omega = \sin(\theta) d\theta d\phi \tag{4.4}$$

Comparison of isotopically simulated one million ^{16}O angles and solid angle function shown in Fig. 4.14. Constant "A" is a value when the angle was equal 90° so the sine function will be equal one.

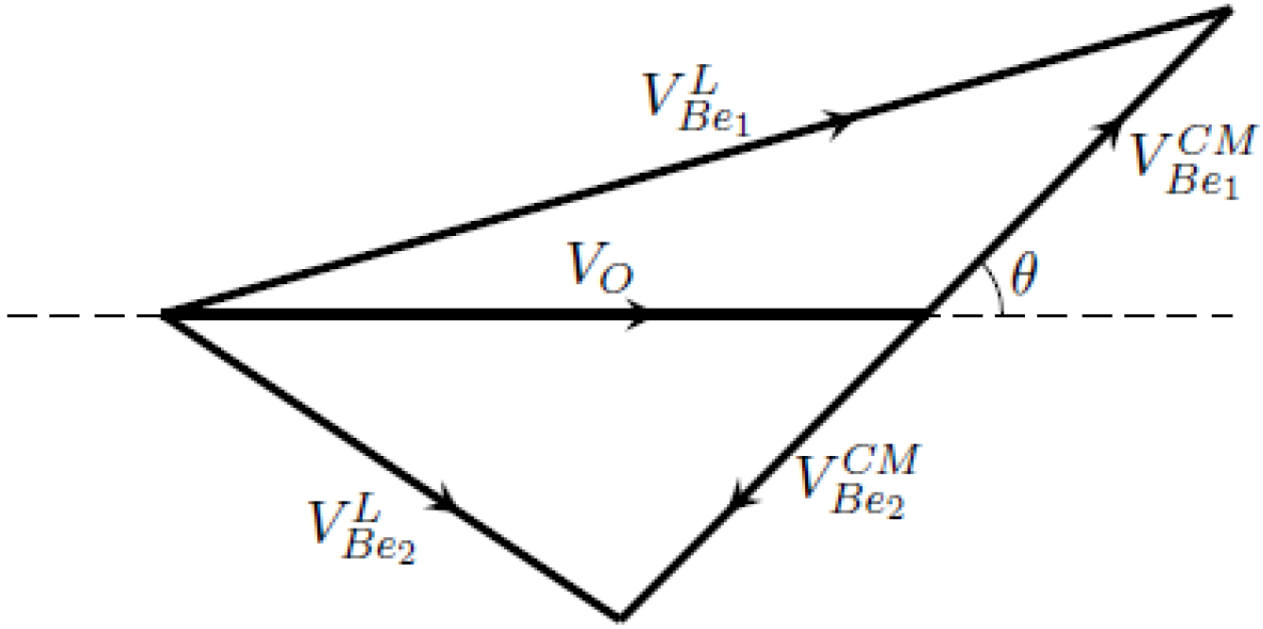

Figure 4.15 Velocities diagram of ^{16}O and two ^{8}Be in the laboratory and center of mass frames.

In the ^{16}O related frame ^{16}O will be in rest and two ^{8}Be will break-up with same energy in opposite directions. In the laboratory frame ^{16}O, on the other hand, has kinetic energy. So again ^{16}O momentum and ^{8}Be center of mass momentum can form any angle, because ^{16}O can break-up isotropically.

Generating random angle in this case as well, ^{8}Be momentum direction was calculated in the center of mass. Fig. 4.15 shows the diagram of ^{16}O and two ^{8}Be velocity diagram in the centre of mass and laboratory frames. The vectorial sum of ^{16}O and ^{8}Be center of mass velocities will be equal to ^{8}Be velocity in the laboratory frame:

$$V_{Be_1}^L = V_O + V_{Be_1}^{CM} V_{Be_2}^L = V_O + V_{Be_2}^{CM} \quad (4.5)$$

Initial energy of ^{8}Be in the center of mass frame can be calculated from excitation energy and Q-value of reaction which is Q = -14.62 MeV. As ^{16}O will be in rest in its frame each ^{8}Be will get equal energy shown below:

$$E_{^8Be} = (E_x + Q)/2 \quad (4.6)$$

With the equation (4.6) kinetic energy can be calculated for each ^{8}Be after ^{16}O break-up. In the laboratory frame each ^{8}Be velocity can be calculated with equation below:

$$(V_{Be_1}^L)^2 = (V_O)^2 + (V_{Be_1}^{CM})^2 + 2V_O(V_{Be_1}^{CM})\cos(\theta) \quad (4.7)$$

$$(V_{Be_2}^L)^2 = (V_O)^2 + (V_{Be_2}^{CM})^2 + 2V_O(V_{Be_2}^{CM})\cos(\theta) \quad (4.7)$$

After calculating each ^{8}Be energy and momentum direction in the laboratory frame with the Eq. 4.7 and Eq. 4.8, both 8Be were simulated. Then ^{8}Be will break-up into two α-particles.

The comparison between the ^{16}O angle dependence from ^{16}O kinetic energy for both experimental and simulation is shown in the Fig. 4.16. The simulated line matches with the experimental curve very well. So it can be surely said that the code is working corrected and it can be used to do simulations for any excited level which will break-up with the $^{16}O \rightarrow {}^8Be + {}^8Be$ decay channel. Results of the simulations were published in the Armenian Journal of Physics in the Ref. [36].

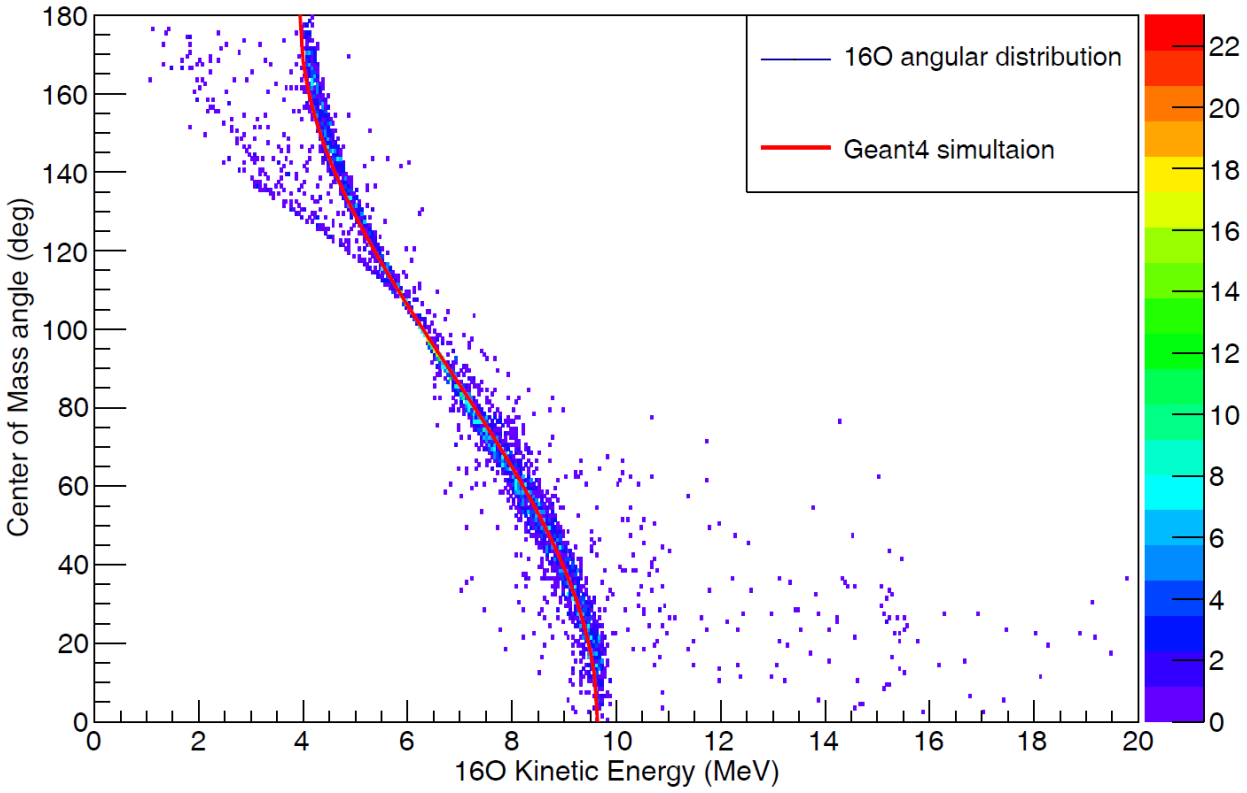

Figure 4.16 Comparison of simulated and experimental ^{16}O kinetic energy and center of mass angle dependences.

Other test of the code can be done other way as well. If the excited levels energies from Ref. [29] will be picked and applied to the code all results should be same. The levels in the Ref. [29] don't have 0^+ spin, but it is proven that they have α-cluster states.

Appling energy in the code without the gate, as it was mention initially, angular distribution will be as shown in the Fig. 4.17. Now the gates should be done. The gate is that all four α-particles are detected in the detectors.

There are four excited levels for sure that are measured in the Ref. [29]. I did apply only that levels and got the results that are in the Fig. 4.17. It can be seen that for all excited level energies angular distributions are very similar. In all angular distributions one million initial ^{16}O were generated. The small difference between angular distributions are just statistical issue.

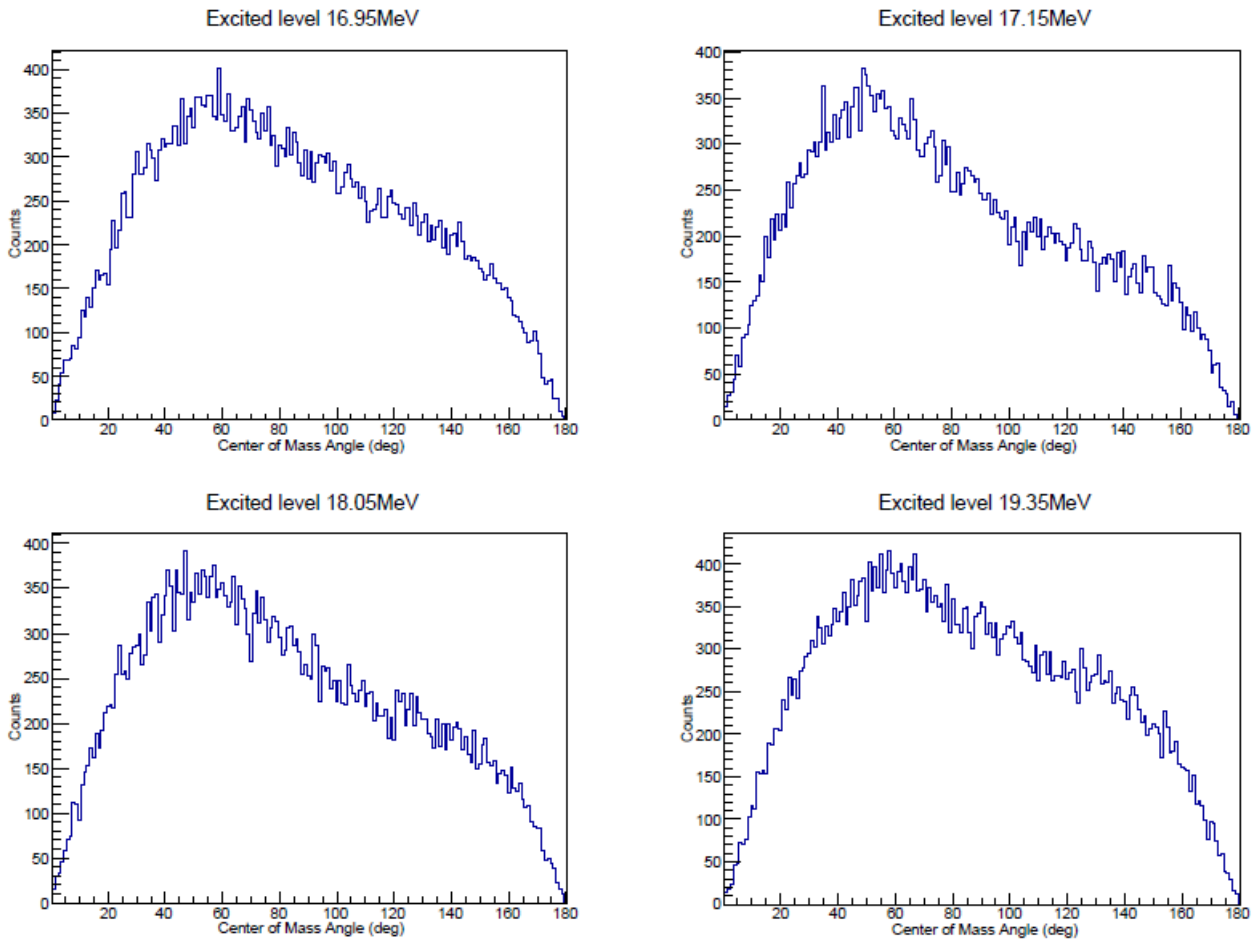

Figure 4.17 Isotropic angular distributions for the states that were measured in the Ref. [29].

This is another prove that the code is working and just levels energies should be measured properly and applied to the code and calculate isotropic angular distribution. That can be used to find 0^+ spin levels or do subtractions and get better shape of experimental results. Than the experimental angular distributions will be compared with the TALYS code angular distributions and assigned spin to each state.

TALYS is a code that can calculate absolute cross section. Due to the measured angular distributions will be divided on this calculated angular distributions to normalize them to make sure that the comparison is correct.

Chapter 5

Conclusion

Both experiments that were done are useful in the nuclear structure studies. It is not possible to explain the structure of the nuclei with the shell model if the nuclei is heavier than A~50. So other methods were implemented to solve that issue. One of them is Super Symmetry (SUSY) to explain the structure of excited sates of nuclei A~190 and the other one is to explain the excited levels in the α-conjugates nuclei above α break-up level. Before measurements were done and suggested linear α-chain structure in some ^{16}O excited levels with the momentum of inertia measurements.

5.1 $^{195,196}Pt(p,xn)^{195}Au$ Experiment

Multiple things were tested and measured during this experimental data analysis. The main component were understanding the software which was used, defining the functions to find the efficiency curves for detectors and the ADC test to choose faster ADC. These are the comments that are important to get good experimental results. Now shortly I will mention what was done for each part briefly.

The expensive NIM standard ORTEC ASPec-927 ADC was replaced with the new faster and cheaper Mesytec MADC-32. The NIM standard ORTEC ASPec-927 has only 2 input channels, but Mesytec MADC-32 has 32 input channels. That 32 channels helped to read out the data from all detectors from same ADC and later after converting into ROOT files do gates and study coincidences. It was shown that the Mesytec MADC-32 has same resolution and linearity as the NIM standard ORTEC ASPec-927 and can be later used for any γ-ray spectroscopy experiments.

Another key part was defining the function to describe the efficiencies of the detectors. As Internal Conversion Coefficient (ICC) was measured during the experiments having the good defined efficiency curve is crucial to measure the Yield of electrons and γ-rays. The best achieved results were presented in the experimental discussion chapter section for both Silicon-Lithium (Si(Li)) and HPGe detectors.

All data was analysed with the RadWare software package which is good in the γ-ray and electron spectroscopes data analysing. The RadWare was tested to find best parameters which was used during experimental data analysing.

After all experimental data was analysed. The ^{196}Au stile remain open as for the 12 MeV proton beam energy on ^{196} target (p,2n) reaction dominates and other channels are open. However, the knowledge on the ^{195}Au level structure was approved. Until 1.5 MeV excitation energy 8 new energy levels and 10 new transitions were observed. The spin and polarity of the states still remains open as angular distributions for that states was not measures, but there is some predictions with the ICCs what spin and polarity excited levels can have.

Also some issues caused the level 439.91 keV which is known, but has uncertainty either the $3/2^+$ or $5/2^+$ spins which is imputing additional uncertainty in the predictions.

Studying the structure of the odd-odd nuclei stile remains open and interesting question. The SUSY is good method to do prediction for odd-odd nuclei only using quantum numbers and other members of the quartet levels list.

5.2 ^{13}C(α,n)^{16}O Experimental Preparations

The ^{16}O is one of the most important nucleus in the nuclear astrophysics. The nucleus helps to understand the age of the structure and α-burning

reactions rates. Due to measuring excited levels of this nucleus precisely is very important.

Very complicated Data Acquisition (DAQ) system was used for this experiment. Totally there were 256 input channels for Double-sided Silicon Strip Detector (DSSD)s and 12 input channels for Deuterated Scintillator Array (DSA).

In the experimental data chapter was described the way of each electronics the purpose and how calibration was done. There was to type of calibration for DSSDs timing and energy. The energy calibration was used to convert from channel to energy and timing calibration was used to do gates and clean up the spectra.

After calibration all data should be reconstructed. As the goal was studying the 4α break-up levels than assumption that theDSSDs detected α-particles.

With ROOT software a lot of coding was done. As it is double-sided than the α-particle will create signals in the front and back part of the detector. The crosstalk corrections were done for both front and back sided. Crosstalk is the fake signal in the detector arising in the nearby strips of the real signal.

Additional Geant4 simulations were done to measure the isotropic distributions for $^{16}O \rightarrow {}^{8}Be + {}^{8}Be$ reaction. The simulation can be used for two purposes. First is that 0^+ excited level will break-up isotropic and with the simulations will be possible to predict 0^+. Second is that background is isotropic so event if excited level is not 0^+, the simulations can be used to calculate the background for that state and then do subtraction.

All this calibration, corrections and simulations will be used during the experimental data analysis. Hopefully, that will enough to find new excited levels in the ^{16}O with the α-clusters.

List of Figures

List of Tables

Bibliography

[1] David J. Gross, PNAS, 93, 25, 14256-14259 (1996)

[2] F. Iachello and A. Arima, The Interacting Boson Model, (Cambridge University Press,Cambridge, 1987)

[3] F. Iachello and P. Van Isacker, The Interacting Boson-Fermion Model, (Cambridge University Press, Cambridge, 1991)

[4] Roelof Bijker, Journal of Physics: Conference Series 237, 012005 (2010)

[5] P. Van Isacker, J. Jolie, K.Heyde and A. Frank, Phys. Rev. Lett. 54, 653 (1985)

[6] A. B. Balantekin and V. Paar, Phys. Rev. B 169, 1 (1986)

[7] J. A. Cizewski, R. F. Casten, G. J. Smith, M. L. Stelts, W. R. Kane, H. G. Börner, and W. F. Davidson, Phys. Rev. Lett. 40, 167 (1978)

[8] J. Barea, R.Bijker, A. Frank and G. Loyola Phys. Rev. C 64, 064313 (2001)

[9] J. Gröger, J. Jolie, R. Krücken, C. W. Beausang, M. Caprio, R. F. Casten, J. Cederkall, J. R. Cooper, F. Corminboeuf, L. Genilloud, G. Graw, C. Günther, M. de Huu, A. I. Levon, A. Metz, J. R. Novak, N. Warr and T. Wendel, Phys. Rev. C 62, 064304, (2000)

[10] J. Jolie, U. Mayerhofer, T. von Egidy, H. Hiller, J. Klora, H. Linder and H. Trieb, Phys. Rev. C 43, R16 (1991)

[11] A. Metz, J. Jolie, G. Graw, R. Hertenberger, J. Gröger, C. Günther, N. Warr and Y. Eisermann, Phys. Rev. Lett. 83, 1542 (1999).

[12] A. B. Balantekin, I. Bars and F. Iachello, Nucl.Phys. A370, 284 (1981)

[13] P. Van Isacker, A. Frank and H. Z. Sun, Ann. Phys. 157, 183 (1984)

[14] Susan M. Fischer, Ph.D. Thesis (1994)

[15] P. Van Isacker, J. Jolie, K. Heyde and A. Frank, Phys. Rev. Lett. 54, 653 (1985)

[16] P. O. Tjom, M. R. Maier, D. Benson Jr., F. S. Stephens and R. M. Diamond, Nucl. Phys. A231, 397-410 (1974)

[17] B. Fodelberg, A. B□acklin, V. Berg and S. G. Malmskog, Nucl. Phys. A153, 301-315 (1970).

[18] G. D. Dracoulis, G. J. Lane, H. Watanbe, R. O. Hughes, N. Palalani, F. G. Kondov, M. P. Carpenter, R. V. F. Janssens, T. Lauritsen, C. J. Lister, D. Seweryniak, S. Zhu, P. Chowdhury, W. Y. Liang, Y. Shi and F. R. Xu, Phys. Rev. C 87, 014326 (2013).

[19] S. C. Wang, X. H. Zhou, Y. D. Fang, Y. H. Zhang, N. T. Zhang, B. S. Gao, M. L. Liu, J. G. Wang, Y. X. Guo, S. C. Li, X. L. Yan, L. He, Z. G. Wang, F. Fang, X. G. Wu, C. Y. He, Y. Zheng, Z. M. Wang and G. X. Dong, F. R. Xu, Phys. Rev. C 85, 027301 (2012).

[20] A. Mauthofer, K. Stelzer, J. Gerl, Th. W. Elze, Th. Happ, G. Eckert, T. Faestermann, A. Frank, and P. Van Isacker Phys. Rev. C 34, 1958

[21] M. Freer et. al., Phys. Rev. C 83, 034314 (2011)

[22] O. Endo, I. Shimodaya, J. Hiura, Prog. Theor. Phys. 31 (1964) 1157

[23] I. Shimodaya, R. Tamagaki, H. Tanaka, Prog. Theor. Phys. 27 (1962) 793

[24] L. R. Hafstad and E. Teller, Phys. Rev. 54, 681 (1938)

[25] J. Hiura, I. Shimodaya, Prog. Theor. Phys. 30 (1963) 585

[26] R. Tamagaki, H. Tanaka, Prog. Theor. Phys. 34 (1965) 191

[27] K. Ikeda, N. Tagikawa, H. Horiuchi, Prog. Theor. Phys. 464 (Suppl.) (1968)

[28] M. Freer, Rep. Prog. Phys. 70, 21492210 (2007)

[29] P. Chevallier, F. Scheibling, G. Goldring, I. Plesser, M. W. Sachs, Phys. Rev. 160, 827 (1967)

[30] E. B. Carter, G. E. Mitchell and R. H. Davis, Phys. Rev. 133, B1421 (1964)

[31] G. E. Mitchell, E. B. Carter and R. H. Davis, Phys. Rev. 133, B1434 (1964)

[32] "Characterizing New Multi-Channel Peak Sensing ADC-Mesytec MADC-32", Armenian Journal of Physics", 9 (1). pp. 29-33. ISSN 1829-1171 A. Gyurjinyan and R. Avetisyan, (2016)

[33] "Measurements of Conversion Electrons in the s-process Branching Point nucleus 176Lu", A. Battaglia, W. Tan, R. Avetisyan, C. Casarella, A. Gyurjinyan, K. Manukyan, S.T. Marley, A. Nystrom, N. Paul, K. Siegl, K. Smith, M.K. Smith, S. Strauss, and A. Aprahamian, Manuscript number EPJA-103416.R1 (approved for publication)

[34] "Conversion Coefficients Measurements for 195Au" Armenian Journal of Physics", 9 (2). pp. 117-119. ISSN 1829-1171 A. Gyurjinyan, (2016)

[35] "16O → 8Be + 8Be Decay Simulation", Armenian Journal of Physics, 9 (1). pp. 39-43. ISSN 1829-1171 A. Gyurjinyan, (2016)

[36] geant4.web.cern.ch/geant4/

[37] www.slac.stanford.edu/comp/physics/geant4/slac physics lists/shielding/physlistdoc.html

[38] isnap.nd.edu/html/research FN.html

[39] www.pelletron.com/charging.htm

[40] isnap.nd.edu/html/research SNICS.html

[41] isnap.nd.edu/html/research HIS.html

[42] www.nndc.bnl.gov/chart/

[43] Radiation Detection and Measurement, 3rd edition, G. F. Knoll (1999)

[44] CAEN, ASPec-927.pdf, www.caen.it

[45] MESYTEC, MADC-32 www.mesytec.com/datasheets/MADC-32.pdf

[46] RadWare, Notes on the use of the program gf3, radware. phy.ornl.gov/gf3/gf3.html

[47] Flexible High Performance VME based Data Acquisition System for the ESA Physics Program, P. R. Anthony and Z. M. Szlata, SLAC-PUB-7201, (1996)

[48] Data Acquisition and Online Analysis at the NSCL, R. Fox, NSCL, (2006)

[49] www.slac.stanford.edu/comp/physics/geant4/slacphysicslists/ shielding/physlistdoc.html

[50] bricc.anu.edu.au/